Universidad Autónoma de San Luis Potosí

Centro de Investigación y Estudios de Posgrado
Facultad de Ingeniería

Modeling lead-acid battery aging and its effect on internal mechanisms.

TESIS

TO OBTAIN THE DEGREE OF:

PhD. in Electrical Engineering

PRESENTS:

M.Sc. Humberto Velasco Arellano

ADVISOR:

PhD. Nancy Visairo Cruz

CO-ADVISOR:

PhD. Ciro Alberto Núñez Gutiérrez

San Luis Potosí, S.L.P. August 2024

UASLP
Universidad Autónoma de San Luis Potosí

FACULTAD DE INGENIERÍA

16 de noviembre de 2023

M.C. HUMBERTO VELASCO ARELLANO
P R E S E N T E.

En atención a su solicitud de Temario, presentada por los Dres **Dr. Nancy Visairo Cruz y Ciro Alberto Núñez Gutiérrez,** Asesora y Coasesor de la Tesis que desarrollará Usted con el objeto de obtener el Grado de **Doctor en Ingeniería Eléctrica**, me es grato comunicarle que en la sesión del H. Consejo Técnico Consultivo celebrada el día 16 de noviembre del presente año, fue aprobado el Temario propuesto:

TEMARIO:

"Modelado del envejecimiento de baterías de plomo-ácido mediante un circuito eléctrico equivalente a partir de su reacción redox"

1. Introducción.
2. Comportamiento de baterías: mecanismos internos y modelado.
3. Modelo de circuito eléctrico equivalente basado en la respuesta en el tiempo.
4. Modelado de circuito eléctrico equivalente basado en modelo mecanístico.
5. Modelo de envejecimiento de la batería con variaciones paramétricas.
6. Conclusiones.
   Referencias

"MODOS ET CUNCTARUM RERUM MENSURAS AUDEBO"

A T E N T A M E N T E

DR. EMILIO JORGE GONZÁLEZ GALVÁN
DIRECTOR

Copia. Archivo.
*etn.

www.uaslp.mx

Av. Manuel Nava 8
Zona Universitaria • CP. 78290
San Luis Potosí, S.L.P.
tel. (444) 826 2330 al 39
fax (444) 826 2336

To my mother, who inspires me to strive for greatness every day and lifts me whenever I fall.
In loving memory of my father.

Acknowledgements

I sincerely thank my esteemed advisors, Nancy Visairo Cruz and Ciro Alberto Núñez Gutiérrez, whose invaluable guidance, unwavering support, and insightful advice have been instrumental in completing this dissertation. I want to express my sincere gratitude to María Isabel Lázaro Báez and Néstor Ricardo Castillo Magallanes for their invaluable contributions to this research. Their expertise in electrochemistry and their collaborative efforts were essential to the successful completion of this project. I am also indebted to Universidad Autonoma de San Luis Potosí for providing a conducive academic environment and essential resources that facilitated the realization of this scholarly endeavor. The intellectual rigor and scholarly discourse encouraged by Posgrado en Ingeniería Eléctrica have significantly contributed to my growth as a researcher and scholar.

Furthermore, I wish to express my heartfelt appreciation to my family and friends for their unconditional love, encouragement, and understanding throughout this academic pursuit. Their unwavering belief in my abilities has been a constant source of motivation.

Lastly, I extend my gratitude to all individuals who supported and contributed to this thesis in various capacities. Your assistance and insights have been invaluable.

This work was financially supported by the National Council of Science and Technology (CONAHCYT) through project A1-S-29705 and scholarship 1010810. I am grateful to Schweitzer Engineering Laboratories for providing essential digital infrastructure. Furthermore, the author acknowledges the support of the UASLP Hydroelectrometallurgy and electric vehicle laboratories for granting access to their facilities.

Summary

This doctoral thesis aims to contribute to the development of battery management systems (BMS), particularly in estimating the battery state, by addressing electrochemical aging mechanisms throughout its useful life under both normal and misuse conditions. The relevance of BMSs is particularly notable in applications such as electric vehicles and battery energy storage systems, where knowing the available energy is crucial.

One of the primary tasks of BMSs is to guarantee the availability and correct operation of the batteries, being an important function the estimation of the state of the batteries, which reveals information about the operation, since it only has measurements of voltage, current, and temperature.

Currently there are many works around the state of charge (SOC) to know the amount of energy inside the battery, and the state of health (SOH) to estimate the wear suffered, among others; however, the estimation of aging is multifactorial which complicates its accurate detection using only the SOH.

It is well known that there are aging mechanisms that appear naturally throughout the useful life of the batteries; however, there are conditions of misuse that can accelerate these mechanisms such as corrosion, sulfation, loss of active material, and stratification. Therefore, obtaining additional information on these phenomena improves the diagnosis of battery aging and wear. Regarding to this, to obtain an equivalent electric circuit model that allows the identification of the normal aging and premature aging mechanisms is the knowledge gap that this research will be addressed. For this work, lead-acid batteries were used, due to their stability, popularity of use, and easy maintenance characteristics.

The equivalent electric circuit (EEC) model has been chosen from the perspective of the emergent engineering technologies, and to establish direct relationships between the electrochemical reactions and the EEC parameters. A thorough review of the state of the art reveals that while numerous approaches have been proposed to address battery aging, a standardized representation of aging maintains academic and technological interest.

Once the EEC was studied, the complexity of interpreting the physical meaning of the aging mechanisms into the EEC parameters was evident. To solve this, a

mechanistic model was developed to determine the electrochemical reactions that arise into electrode-electrolyte interfaces and an electrochemical impedance spectroscopy (EIS) analysis was carried out to specify the EEC structure and stablish the correlations between the EEC parameters and the mechanistic model. These correlations allow to establish a physical reinterpretation of the variations of the EEC parameters with respect to the aging mechanisms.

With this, guidelines are provided for extracting additional information of the aging mechanisms through expanding the scope of the EEC models. The result of this research analysis is a Thévenin circuit with 3-RC parallel arrangements. To determine the EEC parameters a recursive least square estimator is used, and to estimate the battery states of charge a nonlinear observer is designed.

Then, to represent battery aging, a time-varying state space model is obtained, which made possible to represent the parameter variations due to the aging and provide additional information to differentiate normal aging from misused conditions such as overcharge and over-discharge. As the analysis results in the proposed model, the first RC array is directly related with the charge transfer and lead release from the negative electrode, which is related to the loss of active material, the second RC array represents the release of lead from the positive electrode and the generation of sulfates, which in turn is associated with the corrosion mechanism and the occurrence of hard sulfation; the third RC array represents the generation of sulfates and their diffusion in the electrolyte, so that the hard sulfation mechanism is represented with more significant presence in these elements.

Resumen

Esta tesis doctoral pretende contribuir al desarrollo de los sistemas de gestión de baterías (BMS, por sus siglas en inglés), particularmente en la estimación del estado de estas, abordando los mecanismos de envejecimiento electroquímico a lo largo de su vida útil tanto en condiciones normales como de mal uso. La relevancia de los BMS es especialmente notable en aplicaciones como los vehículos eléctricos y los sistemas de almacenamiento de energía en baterías, donde conocer la energía disponible es crucial.

Una de las tareas primordiales de los BMSs es garantizar la disponibilidad y correcto funcionamiento de las baterías, siendo una función importante la estimación del estado de las baterías, que revela información sobre el funcionamiento, ya que sólo dispone de medidas de tensión, corriente y temperatura.

Actualmente existen muchos trabajos en torno al estado de carga (SOC, por sus siglas en inglés) para conocer la cantidad de energía dentro de la batería, y el estado de salud (SOH, por sus siglas en inglés) para estimar el desgaste sufrido, entre otros; sin embargo, la estimación del envejecimiento es multifactorial lo que complica su detección precisa utilizando únicamente el SOH.

Es bien sabido que existen mecanismos de envejecimiento que aparecen de forma natural a lo largo de la vida útil de las baterías; sin embargo, existen condiciones de mal uso que pueden acelerar estos mecanismos como la corrosión, la sulfatación, la pérdida de material activo y la estratificación. Por ello, la obtención de información adicional sobre estos fenómenos mejora el diagnóstico del envejecimiento y desgaste de las baterías. En este sentido, obtener un modelo de circuito eléctrico equivalente que permita identificar los mecanismos de envejecimiento normal y envejecimiento prematuro es la brecha de conocimiento que se abordará en esta investigación. Para este trabajo se utilizaron baterías de plomo-ácido, debido a sus características de estabilidad, popularidad de uso y fácil mantenimiento.

El modelo de circuito eléctrico equivalente (EEC, por sus siglas en inglés) se ha elegido desde la perspectiva de las tecnologías de ingeniería emergentes, y para establecer relaciones directas entre las reacciones electroquímicas y los parámetros EEC. Una revisión exhaustiva del estado de la técnica revela que, aunque se han propuesto numerosos enfoques para abordar el envejecimiento de las baterías, una representación normalizada del envejecimiento mantiene el interés académico y tecnológico.

Una vez estudiada la EEC, se hizo evidente la complejidad de interpretar el significado físico de los mecanismos de envejecimiento en los parámetros EEC. Para solucionarlo, se desarrolló un modelo mecanístico para determinar las reacciones electroquímicas que surgen en las interfases electrodo-electrolito y se realizó un análisis de espectroscopia de impedancia electroquímica (EIS) para especificar la estructura de la EEC y establecer las correlaciones entre los parámetros de la EEC y el modelo mecanístico. Estas correlaciones permiten establecer una reinterpretación física de las variaciones de los parámetros EEC con respecto a los mecanismos de envejecimiento.

Con ello, se proporcionan pautas para extraer información adicional de los mecanismos de envejecimiento mediante la ampliación del alcance de los modelos EEC. El resultado del análisis de esta investigación es un circuito Thévenin con disposiciones en paralelo de 3-RC. Para determinar los parámetros EEC se utiliza un estimador recursivo de mínimos cuadrados, y para estimar los estados de carga de la batería se diseña un observador no lineal.

Despues, para representar el envejecimiento de la batería, se obtiene un modelo de espacio de estados variable en el tiempo, que permite representar las variaciones de los parámetros debidas al envejecimiento y proporcionar información adicional para diferenciar el envejecimiento normal de las condiciones de mal uso, como la sobrecarga y la sobre descarga. Como resultados del análisis en el modelo propuesto, la primera matriz RC está directamente relacionada con la transferencia de carga y la liberación de plomo del electrodo negativo, que está relacionada con la pérdida de material activo, la segunda matriz RC representa la liberación de plomo del electrodo positivo y la generación de sulfatos, que a su vez está asociada con el mecanismo de corrosión y la aparición de sulfatación dura; la tercera matriz RC representa la generación de sulfatos y su difusión en el electrolito, de forma que el mecanismo de sulfatación dura se representa con una presencia más significativa en estos elementos.

Nomenclature

Symbols

Δ_i	Determinants of superior principal submatrices
$\dot{V}(\mathbf{e}_x)$	Derivative of Lyapunov function
$\mathbf{Q}$	Symmetric matrix semidefinite
h_{ii}	elements of the correction matrix where $ii = 11, 22, 33, 44$
$V(\mathbf{e}_x)$	Lyapunov function
$[Pb^{2+}_{ads}]$	Concentration of the adsorbed lead
$[PbSO_{4ads}]$	Concentration of the adsorbed lead sulfate
$[SO^{2-}_4]$	Acid concentration for the used battery
α	charge transfer coefficient
β_i	Maximum adsorbed concentration per unit area with $i = 1, -1, 2, -2, 3, -3, 4, -4$
$\boldsymbol{\theta_{corr}}$	Vector of transfer function coefficients
χ^2	Chi-square error
$\Delta\tau_A$	Change in the τ_A parameter for aging model
$\Delta\tau_B$	Change in the τ_B parameter for aging model
$\Delta\tau_C$	Change in the τ_C parameter for aging model
ΔC_1	Change in the C_1 parameter for aging model
ΔC_2	Change in the C_2 parameter for aging model
ΔC_3	Change in the C_3 parameter for aging model
$\Delta I(t)$	Variation in the Battery current
Δi	Instantaneous change in current
ΔR_0	Change in the R_0 parameter for aging model
Δv	Instantaneous change in voltage
Δv_{SOC}	Change in v_{SOC} between t_0 and t_1

$\Delta\mathbf{A}_F$	Multiplicative changes in the state matrix for aging model
$\Delta\mathbf{B}_F$	Multiplicative changes in the input matrix for aging model
$\Delta\mathbf{D}_F$	Multiplicative changes in the feedthrough matrix for aging model
$\Delta\theta_i(t)$	Variation in the Fraction of the electrode surface occupied by the adsorbate in steady-state with $i = 1, 2, 3, 4$
$\dot{\hat{\mathbf{x}}}$	Derivative of the state vector of the observer
$\dot{\mathbf{x}}$	Derivative of state vector $\mathbf{x}$
$\dot{\mathbf{x}}_a$	Derivative of state vector $\mathbf{x}_a$
η	Correction factor
$\hat{\mathbf{x}}$	State vector of the observer
λ	Forgetting factor value
λ_{min}	Minimum forgetting factor value
$\mathbf{A}$	State matrix for 3-RC circuit
$\mathbf{A}_a$	State matrix for 2-RC circuit
$\mathbf{A}_c$	State matrix for corrosion sensitive circuit
$\mathbf{A}_{fb}$	State matrix for beginning of SOH and 0% SOC
$\mathbf{A}_{fe}$	State matrix for end of SOH and 0% SOC
$\mathbf{A}_{sb}$	State matrix for beginning of SOH and 100% SOC
$\mathbf{A}_{se}$	State matrix for end of SOH and 100% SOC
$\mathbf{B}$	Input matrix for 3-RC circuit
$\mathbf{B}_a$	Input matrix for 2-RC circuit
$\mathbf{B}_c$	Input matrix for corrosion sensitive circuit
$\mathbf{B}_{fb}$	Input matrix for beginning of SOH and 0% SOC
$\mathbf{B}_{fe}$	Input matrix for end of SOH and 0% SOC
$\mathbf{B}_{sb}$	Input matrix for beginning of SOH and 100% SOC
$\mathbf{B}_{se}$	Input matrix for end of SOH and 100% SOC
$\mathbf{C}_c$	Output matrix for corrosion sensitive circuit
$\mathbf{D}$	Feedthrough matrix for 3-RC circuit
$\mathbf{D}_a$	Feedthrough matrix for 2-RC circuit
$\mathbf{D}_c$	Feedthrough matrix for corrosion sensitive circuit
$\mathbf{D}_{fb}$	Feedthrough matrix for beginning of SOH and 0% SOC

$\mathbf{D}_{fe}$ Feedthrough matrix for end of SOH and 0% SOC

$\mathbf{D}_{sb}$ Feedthrough matrix for beginning of SOH and 100% SOC

$\mathbf{D}_{se}$ Feedthrough matrix for end of SOH and 100% SOC

$\mathbf{x}$ State vector for 3-RC circuit

$\mathbf{x}_a$ State vector for 2-RC circuit

$\nabla h(\hat{\mathbf{x}})$ Partial derivative of the function $h(\hat{\mathbf{x}})$

τ_1 Time constant associated to the adsorbed lead in negative electrode for the used battery

τ_1 Time constant associated to the adsorbed lead in positive electrode for the used battery

τ_1 Time constant associated to the adsorbed lead sulfate in positive electrode for the used battery

τ_2 Time constant associated to the adsorbed lead sulfate in negative electrode for the used battery

τ_A Time constant associated to the arrangement R_1C_1

τ_B Time constant associated to the arrangement R_2C_2

τ_C Time constant associated to the arrangement R_3C_3

τ_s Time constant associated to the production of lead sulfate in the used battery

τ_{1g} Time constant associated to the adsorbed lead for general lead-acid reaction in electrode negative

τ_{3g} Time constant associated to the adsorbed lead sulfate for general lead-acid reaction in electrode negative

$\theta_i(t)$ Fraction of the electrode surface occupied by the adsorbate with $i = 1, 2, 3, 4$

θ_{corri} Elements from the vector of transfer function coefficients with $i = 1, 2, 6, 4, 5$

θ_{iss} Fraction of the electrode surface occupied by the adsorbate in steady-state with $i = 1, 2, 3, 4$

a_{11} Term of matrix $\Delta\tau_A$ at position 1,1

$a_{corr}; b_{corr}; c_{corr}; d_{corr}$ Vector of transfer function coefficients

Ar Area

B_i Battery used in test where $i \in \mathbb{Z}$

b_i Tafel coefficient to the related reaction rate constant

C_1 Capacitance of the first RC arrangement

C_2 Capacitance of the second RC arrangement

C_3 Capacitance of the third RC arrangement

$C_{available}$ Remaining capacity

C_{corr}	Inversely proportional capacitor to the passive film
C_{dln}	Interfacial capacitance for negative electrode
C_{dlp}	Interfacial capacitance for positive electrode
C_{dl}	Interfacial capacitance
C_{nom}	Battery nominal capacity
C_{Oxd}	Concentration at the electrode surface of the spice to oxidize
C_{Red}	Concentration at the electrode surface of the spice to reduce
CPE_1	Constant phase element representing non-ideal capacitor
$E(t)$	Time-variant potential difference
$E(t)$	Variation of the Time-variant potential difference in steady-state
E	Practical voltage
e^-	Chemical symbol of electron
E^0	Cell standard potential
E_a^0	Anode standard potential
E_c^0	Cathode standard potential
$e_{base_{corr}}$	Allowed error in RLS algorithm
$E_{corr}(s)$	voltage transfer function for RLS algorithm
E_{corr}	Voltage measured for RLS algorithm
$Error()$	Relative error
F	Faraday constant
$h(\mathbf{x})$	Output function for 3-RC circuit
$h(\mathbf{x})_a$	Output function for 2-RC circuit
h	Sensitive value for the forgetting factor adjustment
H^+	Chemical symbol of hydrogen
H_2O	Chemical symbol of water
H_2SO_4	Chemical symbol of sulfuric acid
$I(t)$	Battery current
I	Current density
i	Demanded current
jZ''	Imaginary component of the impedance measured
K_i	Reaction rate constants where $i = 1, -1, 2, -2, 3, -3, 4, -4$

k_i	Pre-exponential factor to the related reaction rate constant
M_n	Area of the negative electrode
M_p	Area of the positive electrode
M_w	Molecular weight
p_{τ_i}	Frequency of the pole associate to the time constant τ_i with $i \in \mathbb{Z}$
Pb	Chemical symbol of lead
Pb^{2+}_{ads}	Adsorbed lead ions
PbO_2	Chemical symbol of lead dioxide
PbO_x	Non-stoichiometric lead oxide
$PbSO_4$	Chemical symbol of lead sulfate
$PbSO_{4ads}$	Adsorbed lead sulfate
Q	Theoretical capacity
$Q_{specific}$	Specific capacity
R	Universal gas constant
R_0	Serial resistance
R_1	Resistance of the first RC arrangement
R_2	Resistance of the second RC arrangement
R_3	Resistance of the third RC arrangement
R_s	Solution resistance
R_{corr}	Resistance of the material to be corroded
R_{eol}	Internal resistance at the end of life
R_{new}	Internal resistance at the start of lifetime
RC	Resistance and capacitor parallel arrangement
s	Complex variable
SO_4	Chemical symbol of sulfate
SOH_C	SOH estimated by battery capacity
SOH_R	SOH estimated by battery internal resistance
T	absolute temperature in Kelvin
t	Desired time
t_0	Initial time of evaluation
t_1	Final time of evaluation

T_c Sampling Time

$t_{cut-off}$ Time it takes to reach its cut-off voltage

u System input

v_1 Voltage in parallel arrangement R_1C_1

v_2 Voltage in parallel arrangement R_2C_2

v_3 Voltage in parallel arrangement R_3C_3

v_{batt_p} Terminal voltage simulated for v_{OC} considered lineal

$v_{batt_{measured}}$ Battery voltage measured along a complete charge/discharge cycle

$v_{batt_{model}}$ Battery voltage obtain from simulation model along a complete charge/discharge cycle

$v_{batt_{pl}}$ Terminal voltage simulated for v_{OC} considered piecewise linear

$v_{batt_{pol}}$ Terminal voltage simulated for v_{OC} considered polynomial

v_{batt} Terminal voltage

v_{corr} Voltage in parallel arrangement $R_{corr}C_{corr}$

$v_{cPb^{2+}_{ads}}$ Rate of consumption of the adsorbed lead

$v_{cPbSO_{4ads}}$ Rate of consumption of the adsorbed lead sulfate

$v_{fPb^{2+}_{ads}}$ Rate of formation of the adsorbed lead

$v_{fPbSO_{4ads}}$ Rate of formation of the adsorbed lead sulfate

v_{OC} Open Circuit Voltage

v_{SOC} State of Charge Voltage

x Number of electrons transferred in the reaction

Y_0 Characteristic parameter of CPE_1 given in Farads

Z' Real component of the impedance measured

z Discrete variable

$Z_n(s)$ Negative electrode impedance

$Z_p(s)$ Positive electrode impedance

$Z_{fn}(s)$ Negative electrode faradic process of the impedance

$Z_{fp}(s)$ Positive electrode faradic process of the impedance

$Z_{Tg}(s)$ Transfer function from the impedance of lead-acid battery generalized

$Z_T(s)$ Total transfer function of the impedance for the used battery

$\hat{\mathbf{y}}$ Output of the state-state observer

$\dot{\mathbf{e}}_x$	Derivative of the error between model and observer
$\mathbf{e}_x$	Error between model and observer
$\mathbf{H}$	Correction matrix of the observer
$\mathbf{y}$	Output of the state-state system

Abbreviations

BESS	Battery Energy Storage System
BMS	Battery Management System
CC	Coulomb Counting
DC	Direct Current
EEC	Equivalent Electric Circuit
EIS	Electrochemical Impedance Spectroscopy
NC	Normal Condition
OC	Overcharge
OD	Over-Discharge
P2D	Pseudo-two-Dimensional
PS-260	Power Sonic model 260
RLS	Recursive Least Square
SOC	State of Charge
SOH	State of Health
SW	Switch
UPS	Uninterruptible Power Supply
VRLA	Valve-Regulated Lead-Acid

Contents

List of Figures

List of Tables

Chapter 1

Introduction

In the present era, where technology is predominantly powered by electrical energy, energy storage has emerged as a significant concern for businesses and clients. Numerous demanding applications like Electric Vehicles [5], energy distributed resources [6, 7], and Uninterruptible Power Supply (UPS) for critical processes [8], necessitate energy storage backup as a central component of their operations. In this way, recent studies have emphasized the significance of energy storage from the economic [9], technological [10], and operative [11] standpoint.

Batteries are widely considered a reliable energy storage method due to their versatility in terms of different technologies, energy densities, weights, volumes, and other electrical characteristics [4, 12]. Among the most notable types are Valve-Regulated Lead-Acid (VRLA) batteries [13, 14], which have gained popularity due to their competitive characteristics in production, maintenance, and recycling [15]. Additionally, VRLA batteries are known for their relative stability when exposed to external variables and are highly suitable for commercial usage [16].

The batteries serve as a crucial component of the system's flexibility. However, any battery failure may compromise or halt the system's operation. As such, a range of challenges have emerged that require attention, such as the identification of better construction materials [17], improvements in battery power delivery [18], the implementation of more efficient battery state management [19], and the development of effective fault detection mechanisms [12]; focusing this work on improving the efficiency of battery state management, specifically in the detection of aging.

One of the practical approaches to address the challenges related to batteries is using mathematical modeling techniques. These models should be able to depict the battery's behavior throughout its entire lifespan accurately [20, 21, 22, 23]. The equivalent electrical circuit model is a popular and preferred model used in battery modeling due to its simplicity and ability to represent the cells' critical internal states [4]. As a result, this type of modeling is widely employed by most battery management systems [12].

Therefore, battery energy storage, available power, and aging status can be assessed with its specified energy delivery capacity [24]. Aging, a general term, encompasses the natural deterioration of active materials through various chemical processes, including

hard sulfation, corrosion, stratification, and mass loss [25]. Consequently, identifying abnormal aging is crucial for indicating premature onset of one or more of these aging mechanisms. However, detecting these mechanisms is challenging due to intricate models and their simultaneous occurrence within short timeframes, hindering their identification [1].

The battery's aging process impacts its model, making it essential to estimate its state of health (SOH). This state reflects the battery's loss of capacity or energy retention [26]. Moreover, it is crucial to comprehensively study the aging mechanisms responsible for the changes detected by the SOH [18]. In this way, it could address one of the challenges of detecting fault conditions. It is worth noting that one of the factors contributing to aging is the degradation process, which will ultimately appear at the end of the battery's useful life. However, the early appearance of this process is a clear sign of a fault condition [27].

Hence, accurately measuring the SOH of a battery is essential but challenging. SOH cannot be measured directly online, therefore necessitates the use of alternative parameters to calculate it. These parameters must be related to the SOH to serve as a surrogate for the real SOH [28]. In-depth reviews analyzing the study of SOH and compiling standard estimation methods are available in [29, 30]. A widely accepted approach is periodically evaluating batteries at various aging points to compare their responses and establish an association with the SOH [31, 32].

Studies have been carried out on lead-acid batteries using electrochemical impedance spectroscopy (EIS) to determine the equivalent circuit parameters of the battery relative to its SOH and to evaluate aging through premature battery capacity loss. Several works, including [33, 34], have utilized EIS to estimate the EEC parameters, which are monotonically related to capacity loss. Similarly, [31] have reported a correlation between the SOH and impedance measure in double-layer charge transfer. At the same time, it is unnecessary to evaluate all impedance spectra frequencies to determine the SOH. Instead of this, the entire impedance spectra can be used to explain the aging mechanisms.

Other methods, like [35], have been used to represent the battery model, including the time response to current, stochastic models, and open-circuit voltage (v_{OC}) characterization. [23] have proposed the latter as an alternative tool to estimate the SOH in a shorter time, requiring offline conditions. In addition, specific works have developed algorithms based on Kalman filters to evaluate the state of charge (SOC) and SOH by examining changes in the model parameters [36].

The studies above focus on the detection of aging through the evaluation of energy and capacitance loss. These studies aim to develop a percentage indicator of SOH that encompasses all aging mechanisms. This approach enables a comprehensive assessment of the system's health and can provide valuable insights for further analysis and decision-making.

The works cited in [28, 37] propose a semi-empirical equivalent electric circuit (EEC) model that utilizes the Nernst equation to parameterize the model. This approach provides supplementary information that can help infer the occurrence of aging reflected

in parametric changes.

Several studies have leveraged artificial neural networks to forecast battery aging. For example, [38] employed these networks to predict the performance decline of Li-ion batteries using data from four commercial suppliers. [39] focused on electric vehicle batteries, utilizing artificial neural networks to assess and forecast battery degradation under real-world driving conditions. Research on lead-acid batteries has also incorporated artificial neural networks. A hybrid convolutional neural network model developed in [40] accurately predicted battery aging with a margin of error of only 5%. Additionally, [20] estimated the aging status of flooded lead-acid batteries using a feed-forward neural network approach. By determining the current battery health, these studies contribute to anticipating future aging patterns and mitigating their impact.

Fuzzy logic has also been employed to study battery aging. For instance, [21] utilized a fuzzy logic approach to identify battery degradation within a battery energy storage system (BESS) tasked with frequency and voltage control. Reference [41] introduced a fuzzy logic-based control strategy to dynamically adjust a battery's safe operating limits in response to its power and aging status. Regarding lead-acid batteries, various heuristic methods, including evolutionary, genetic, and particle swarm algorithms, have been applied to optimize SOH models for aging assessment and detection, as reported in [42]. These studies indicate that fuzzy logic excels at capturing aging-induced model variations, thereby facilitating timely system adaptations to prevent battery-related hazards.

Kalman filters have been employed in previous research to address battery aging. For instance, [22] utilized this technique to estimate essential battery parameters, including SOC and SOH, throughout the battery's lifespan. Building upon this, [43] refined the SOC estimation process by combining Kalman filters with least squares to accommodate various aging scenarios. While these studies present robust methods to counteract aging-induced variations, they primarily focus on adapting to these changes rather than directly predicting the aging process itself.

An alternative method involves analyzing EIS data from batteries. Studies like [44] and [45] have demonstrated that by examining EIS changes in batteries with varying degrees of degradation, it is possible to correlate these changes with battery aging and subsequently predict the remaining useful life based on historical data.

Certain semiempirical models are developed by integrating established models with parameters determined through specific experimentation and calculations, as exemplified in [37]. These models often derive their parameters from electrochemical models, with parameter deviations indicative of abnormal aging.

While previous studies have provided valuable insights into battery behavior, existing methodologies present several challenges. Data-driven models, as exemplified in [46], often require extensive training data for each specific application, resulting in models that lack transparency and physical interpretability. Heuristic models, commonly employed for optimization as in [47], can be influenced by model uncertainties and limited adaptability. Time-domain models, as described in [46], can

be computationally demanding and provide limited insight into the fundamental aging mechanisms. Mathematical models, while useful in specific contexts, are susceptible to measurement errors and may not generalize well across different conditions. Electrochemical models, as explored in [47], offer a detailed understanding of internal aging processes but require complex formulations and precise state-of-charge estimates.

The EEC models provide simplified representations of battery behavior, offering low computational costs suitable for real-time applications as outlined in [12]. However, the accuracy of EEC models is heavily influenced by measurement and estimation precision, as highlighted in [46]. In contrast, semi-empirical models leverage the simplicity of EEC while incorporating physical meaning into their parameters through electrochemical measurements. This approach, as demonstrated in [28], allows for a deeper understanding of internal battery processes. In this way, this thesis study the battery aging by using a semi-empirical mathematical model correlating a mechanistic model and its constituent reactions with an EEC model parameterized through EIS. The objective is to assess the effectiveness of this model in representing specific changes that occur due to each aging mechanism.

1.1 Objective

This work aims to develop a battery model that adequately represents the ageing conditions for battery banks.

1.1.1 Specific objectives

- To analyse the basic electrochemical principles (anode-cathode-electrolyte reactions) of a battery under normal conditions throughout the useful life in order to model it by an equivalent electrical circuit.
- To propose the structure of an equivalent electric circuit model by correlating the reactions of the mechanistic model through the analysis of electrochemical impedance spectroscopy and control theory.
- To design battery state estimation schemes of state of charge and state of health, as well as parametric estimation method.
- To validate experimentally the proof of concept under normal and abnormal conditions on a valve regulated lead-acid PS-260 battery bank.

1.2 Motivation

This thesis work arises from the interest of addressing the research gap of having an EEC model that be able to identify the normal aging from premature aging mechanisms,

with the perspective of being useful for the emerging technology of engineering, such as electric vehicles and battery energy storage systems.

1.3 Problem statement

Traditional battery aging diagnosis primarily relies on SOH estimation. While effective for overall battery degradation assessment, this approach falls short in isolating specific aging mechanisms. To address this limitation, this thesis investigates the feasibility of employing an EEC model to represent and characterize the electrochemical reactions within a battery. By providing supplementary information beyond SOH, the EEC model is expected to facilitate a more in-depth analysis of battery aging and lay the groundwork for identifying individual aging mechanisms.

1.4 Hypothesis

By incorporating a parametrization based on electrochemical principles into an equivalent electrical circuit model, this research postulate that a more comprehensive understanding of battery aging can be achieved, enabling the identification and characterization of individual aging mechanisms beyond traditional state-of-health metrics.

1.5 Methodology

To address the thesis work presented, the first thing that was done was to study the operation of the battery; for this, the electrical characteristics of the battery and its interaction in electrical circuits with other components were reviewed in the same way the electrochemical characteristics of the batteries were studied, their internal reactions, and how these determine the electrical behavior, highlighting how batteries are systems that are affected by aging, progressively modifying their performance; this is described by aging mechanisms that depend on the battery technology used; however, in any case, the aging mechanisms represent the deterioration of the elements involved and how this changes the electrical response of the battery, to describe these behaviors, mathematical models are used, so a review was made of the existing EEC models and the different proposals present in state of the art, where many works seek to address the issue of aging, but it is still a topic for improvement, due to not having a single representation of aging and being of great interest for battery management systems (BMS), in this way we could understand scope, limitations and challenges around the current state of science and technology regarding batteries and monitoring its status for engineering applications.

With all the information obtained, different models were analyzed, selecting an EEC model with a 3-RC arrangement and the behavior of the EEC model in the face of changes in the state of charge and aging was studied, observing how these states modify the parameters of the model under conditions of use recommended by the manufacturer, allowing us to infer the existence of a relationship between parametric changes and unwanted behaviors due to misuse concluding that it is necessary to know the physical meaning of the model parameters to understand what the variations above reveal.

Afterward, a mechanistic model was developed to know the electrochemical interpretation of the battery impedance; EIS analysis was carried out to measure the actual impedance of the batteries and compare the results with the developed mechanistic model. With the model and measurements, control theory was used to correlate the electrochemical reactions with the EEC model using the time constants of the reactions to give physical meaning to the parameters of the EEC model.

Once the interpretation of the EEC model was known, battery state estimation schemes were designed, for which an observer was used for systems with non-linear output mapping to estimate the SOC and know the voltage responses of the RC arrays throughout the useful life of the battery, allowing an in-depth analysis of the effects of aging.

For that purpose, a VRLA 2 V 6 Ah battery has been used in a battery setup for electrical measurements, analyzing the behavior of these variations using batteries aged by the recommendations of the IEC 60095-1 standard, enabling them to reach the end of life in ideal conditions. With this information, it is validated that the behavior throughout the battery's life is monotonically decreasing, so the proposed model is valid throughout the useful life, and the aging behaves as modeled. Once it is validated that the proposed model represents the battery, measurements are made to batteries exposed to over-charging and over-discharging conditions, with which we seek to compare the evolution of the SOH in these conditions and the proposed model, revealing additional information for the correct estimation of the state of the battery. The value of this research lies in the formal proposal of a methodology that demonstrates the feasibility of measuring battery aging using voltage and current measurements.

1.6 Contributions

The contribution lies into two notable results. The first one consists on a reinterpretation of the physical meaning of the EEC model through a correlation with a mechanistic model. This correlation has the following characteristics:

- This circuit is composed of a dependent source ($v_{OC}(v_{SOC})$) which represents the amount of stored energy
- A series resistance R_s which represents the solution resistance and is related to the electrolyte loss and stratification;

- The first arrangement R_1C_1 represents the charge transfer and lead release from the negative electrode, which is related to the loss of active material
- The second arrangement R_2C_2 represents the release of lead from the positive electrode and the generation of sulfates, which in turn is associated with the corrosion mechanism and the occurrence of hard sulfation
- The third arrangement R_3C_3 represents the generation of sulfates and their diffusion in the electrolyte, so that the hard sulfation mechanism is represented with more significant presence in these elements.

The second one consists on proposing a state-space represtation of the EEC model that describes the aging of the battery through the parametric variation of the system, where the changes are treated as multiplicative variations associated with electrochemical reactions which in turn are related to some of the common aging mechanisms.

1.7 Thesis structure

This work is composed of 6 chapters. Chapter 2 describes the general behavior of the battery as well as valuable definitions to understand the development of the work. Chapter 3 explains the modeling of the battery from a conventional EEC model, its scope, and limitations, and explores the parametric changes of the battery from an experimental perspective. Chapter 4 explains in detail a mechanistic model of the battery and the correlation between the EEC model and how it is related to the internal reactions through the analysis of EIS and control theory, allowing a redefinition of the elements that conform to the model. Chapter 5 proposes a model with parametric variations through the use of a non-linear observer, which allows us to observe changes in state variables that complement the aging information obtained from the battery; this allows us to improve the diagnostic techniques and establish a first step in a diagnostic system for internal failures. Finally, Chapter 6 shows the conclusions of the thesis work developed and the future perspectives to be developed with the information obtained here.

Chapter 2

Battery behavior: internal mechanisms and modeling

This chapter presents the basic concepts necessary to generally understand the work carried out.

Batteries are energy storage systems in the form of chemical energy. This system was born in 1800 with experiments by Alessandro Volta, who proposed the first battery following the principles of galvanism. However, it was not until 1868 that George Leclanché invented the first primary battery with liquid electrolyte. These inventions and the resulting research in galvanism established the electrochemical foundations for modern batteries [48].
It is essential to define some concepts that are often confused:

- A cell is the smallest electrochemical unit, which delivers energy according to the materials by which it is constructed.
- A primary cell is a single-use cell.
- A secondary cell is a cell whose chemistry allows it to recharge.
- A battery is made up of a set of cells. Figure 2.1 shows the difference in the symbology of a battery and a cell [4]. However, for electrical circuits the symbols are used interchangeably.

2.1 How cells work

A redox reaction is the fundamental process powering a battery. It involves the transfer of electrons between chemical species (active materials). One species loses electrons

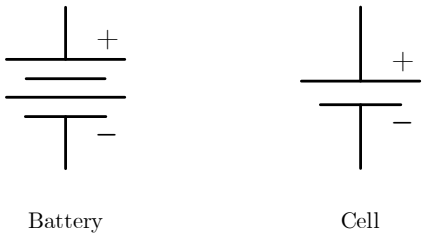

Figure 2.1: Symbology of a battery and a cell.

(oxidation) while another gains them (reduction). This exchange of electrons creates an electrical current, which is delivered by the battery [4].

A cell mainly comprises four elements: A positive electrode, a negative electrode, an electrolyte, and a separator. There may be other elements in the construction of the cell, but the four mentioned above are the main components that react to produce energy. Figure 2.2 shows the general diagram of the battery [4].

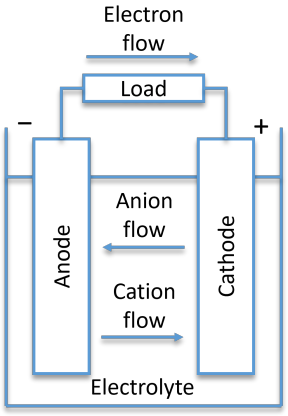

Figure 2.2: Schematic diagram of the composition of a battery.

The negative electrode is usually composed of a pure metal, a metal alloy, or even hydrogen. During the discharge, this material gives up electrons in a process by which the electrode oxidizes. During charging, the electrode accepts electrons through a reduction process [4].

The positive electrode is typically a metal oxide, a sulfide, or oxygen. During the discharge, this material gains electrons, undergoing a reduction process. During charging, it liberates electrons, oxidizing them again [4].

The electrolyte is a medium that allows the transfer of ions and stabilizes the redox reaction. During charging, the electrolyte allows the flow of ions or species formed from

one of the electrodes to the other. This medium allows the ions to travel in the opposite direction during the discharge [4].

The separator is a porous material that isolates the electrodes from each other, allowing the flow of ions for the redox reaction and preventing electrical flow, which prevents short circuits and self-discharge [4].

2.1.1 Discharge process

Of the elements that make up the battery, the electrodes are characterized by their potential electrochemical energy since the negative electrode favors the release of electrons through the external electrical circuit. In contrast, the positive electrode accepts the electrons coming from the external circuit. For this reaction to occur, there must be a circuit that conducts electrons between the electrodes and a medium that allows the flow of ions, the latter facilitated by the electrolyte. Finally, the separator's job is to prevent the electrodes from coming into direct contact, generating a short circuit. Electrically, the discharge process occurs when the battery delivers energy to a load [4].

2.1.2 Charge process

The charging process is not always possible in a battery since the primary cells' electrochemical process is irreversible. Once the materials react, they are permanently converted into another product, which can only be used once. On the other hand, the secondary cells can be charged; for this, it is necessary to connect to an external power source greater than the potential of the battery. In this way, the movement of the ions to their electrode of origin and the recomposition of electrons using the voltage of the external source return to the initial state. Secondary cells can be charged and discharged many times; however, the process can be repeated a finite number of times due to deterioration [4].

2.1.3 Electrochemical process

These processes applied to lead-acid batteries are described in (2.1), where the terms on the left represent the electrodes: Pb negative electrode, PbO_2 positive electrode. On the other hand, the element on the right represents lead sulfate as a product resulting from the reaction, and the symbol $\leftrightarrows$ indicates that the reaction could occurred from left to right or from right to left [49].

$$Pb + PbO_2 \leftrightarrows PbSO_4 \tag{2.1}$$

However, equation (2.1) is incomplete, it only indicates the materials of interest, to complete the reaction a mass balance must be made, guaranteeing that the material

before and after the reaction is conserved, as well as a charge balance, guaranteeing that the energy before and after the reaction is conserved[49].

The oxidation reaction in the negative electrode is first analyzed, taking only the lead (Pb) that forms the electrode and the lead sulfate ($PbSO_4$) that is the material resulting from the reaction [49], as show in equation (2.2).

$$Pb \leftrightarrows PbSO_4 \tag{2.2}$$

Considering that the electrolyte is an acidic medium, where lead with a neutral state reacts with the acid electrolyte (SO_4), it can be observed the lead on both sides of the reaction, but the sulfates on the left side are missing; in order to balance the reaction, they are added respecting the conservation of matter, resulting in a reaction electrically unbalanced by a charge of +2, so it adds 2 electrons ($2e^-$), as shown in (2.3) [49].

$$Pb + SO_4 \leftrightarrows PbSO_4 + 2e^- \tag{2.3}$$

Then, the analysis on the positive electrode is addressed, where the reduction occurs, by using only lead dioxide as the initial electrode and lead sulfate as a result of the reaction (2.4) [49].

$$PbO_2 \leftrightarrows PbSO_4 \tag{2.4}$$

Again, balancing the material in both parts of the reaction, adding the missing sulfate, from the electrolyte (SO_4), in the left part of the reaction; however, adding the sulfate causes a surplus of oxygen on the left. Compensating with two water molecules ($2H_2O$) are added to the right and four hydrogen ($4H^+$) on the left, thus guaranteeing balance. However, when carrying out the charge balance, the electrode has a gain of +2 coming from the hydrogens, which is compensated by adding 2 electrons ($2e^-$), which were added in the oxidation process, remaining as indicated in equation (2.5) [49].

$$PbO_2 + SO_4 + 4H^+ + 2e^- \leftrightarrows PbSO_4 + 2H_2O \tag{2.5}$$

Finally, both the reduction and oxidation processes are added, leaving the form (2.6), where the left side of the formula represents the compounds of the battery, and the right side the molecules resulting from the chemical reaction [49].

$$Pb + PbO_2 + 2H_2SO_4 \leftrightarrows 2PbSO_4 + 2H_2O \tag{2.6}$$

where $2H_2SO_4$ is the sulfuric acid of the electrolyte. The charging and discharging process eventually damages the battery since every time we recharge the battery, the internal structure deforms due to the heat, creating imperfections in the metal that interfere with the mobility of the ions [50].

The redox formula presented above is exclusive for lead-acid batteries; However, the redox process follows the steps described here for different materials, with the previous process serving as an example [51].

2.1.4 Materials

The selection of electrodes for a battery requires combining two materials, one highly oxidizing (on the left of the periodic table) and another highly reducible (on the right of the periodic table). However, two arbitrary elements cannot be selected since an electrolyte must be capable of stabilizing the reaction without deterioration, so the selection of materials becomes complicated. For this purpose, studies of different combinations have obtained electrodes commonly used in redox reactions[4], in Table 2.1 common batteries technologies are shown.

Inert gases are not useful for the redox reaction since, having full electron shells, they

Table 2.1: Common batteries technologies [4].

Technology	Negative electrode	Positive electrode	Electrolyte	Nominal voltage
Lead-acid	Pb	PbO_2	H_2SO_4	2,1V
Dry-cell	Zn	MnO_2	$ZnCl_2$	1,6V
Alkaline	Zn	MnO_2	KOH	1,5V
Nickel Cadmium	Cd	$NiOOH$	KOH	1,35V
Nickel hydrogen	H_2	$NiOOH$	KOH	1,5V
Nickel zinc	Zn	$NiOOH$	KOH	1,75V
Silver zinc	Zn	Ag_2O	KOH	1,6V
Zinc air	Zn	O_2	KOH	1,65V

tend not to react chemically.

It is essential to highlight that the batteries explored at the frontier of knowledge related to electric vehicles are Lithium-Ion batteries [52, 53, 54, 55, 56], due to the characteristics present in their behavior. Even so, there is a large number of works that place lead-acid batteries on the market due to their stability and high level of recycling [57, 58, 59, 60, 61].

For this reason, lithium-ion and lead-acid batteries stand out for their characteristics, having better performance [62], in addition to being a trend in innovation [63], which is why it was decided to use batteries for this work of lead-acid since its benefit-cost ratio narrowly exceeds that of lithium-ion [62].

2.2 Electrical characteristics

Remember that although the battery is an electrochemical system, its main application is energy storage and delivery for electrical systems. Therefore, it also has electrical characteristics of interest, such as voltage, capacity, and energy [12].

2.2.1 Theoretical voltage

One of the fundamental characteristics of a battery is the voltage since the strength with which it can supply energy depends on it. The voltage that a battery can deliver is directly related to the materials that react inside it; this is called theoretical voltage or standard potential, which is limited according to the oxidation potential of the electrodes and is mathematically [64], defined as (2.7).

$$E^0 = E_c^0 - E_a^0 \tag{2.7}$$

where E^0 is the cell standard potential, E_c^0 is the cathode standard potential, and E_a^0 is the anode standard potential. These data are obtained from tables and do not consider the reaction medium, so this voltage corresponds to the voltage obtained from a single cell regardless of the amount of active material and remains constant throughout the reaction [64], giving the potentials shown in (2.8), corresponding to the anode and cathode, respectively. These voltages are generated by the level of oxidation or reduction of the material, allowing electrons to be absorbed or released.

$$\begin{aligned} E_a^0 &= -0.356 \text{ V} \\ E_c^0 &= 1.685 \text{ V} \end{aligned} \tag{2.8}$$

With these data, the standard potential is calculated according to the equation (2.7) [65].

$$E^0 = E_c^0 - E_a^0 = 1.685 - (-0.356) = 2.041 \text{ V} \tag{2.9}$$

When considering the reaction medium, the voltage is modified; the practical voltage is used for this purpose and is explained in the following subsection.

2.2.2 Practical voltage

The practical voltage in a battery corresponds to the potential difference produced by the different electrode materials and how it is affected by factors such as temperature and concentration of the medium [51]. This value is governed by the Nernst equation shown in (2.10).

$$E = E^0 - \frac{RT}{nF} \ln\left(\frac{c_{\text{Oxd}}}{c_{\text{Red}}}\right) \tag{2.10}$$

where E is the practical voltage, R is the universal gas constant, T is the temperature in kelvins, F is the Faraday constant, n is the number of electrons transferred in the cell reaction, c_{Oxd} is the concentration at the electrode surface of the species that release the electrons to external circuit of the battery, c_{Red} is the surface concentration of the ions that flow throw the electrolyte [51].

As the concentration of surfaces on the electrodes depends on the electrolyte concentration available to react, each time energy is consumed from the battery, this electrolyte is finished. Hence, the battery loses voltage until it reaches a point where there is not enough material left to react, known as the end of the state of charge, this phenomenon represents the change in open circuit voltage [51].

For a lead-acid battery, the value of n is known since 2 electrons are transferred in its redox reaction; in the same way, the concentration of the surface of the electrode to be oxidized is used as a unit, obtaining its normalized ratio and the denominator is obtained from knowing the concentration of the electrolyte for the electrode to be reduced, using a density of 1. 28 g cm^{-3}, as this is the typical density in a lead-acid battery, thus obtaining a concentration of 6.9 molar [51], and finally, the ambient temperature is considered as 25° C.

$$E = 2.041 - 0.02958 \cdot \ln(\frac{1}{6.9^2 \cdot 6.9^2}) = 2.269 \text{ V} \tag{2.11}$$

2.2.3 Theoretical capacity

The theoretical capacity (Q) of a battery represents the amount of current that it can deliver over a defined time; this is determined by the amount of active material contained in the electrodes of the battery and is defined in terms of Coulombs (C) or Ampere-hours (Ah) [50].

These values can be consulted using tables indicating the capacity per gram of material of the complete cell or of each electrode separately; in the case of having the data of each electrode separately, both values are added as the inverse of the sum of the inverses [50].

This value represents the amount of active material in grams necessary to obtain the desired capacity. However, the weight obtained differs from the actual weight of a battery, as this calculation only considers the electrodes and disregards the rest of the materials involved [50].

In the case of lead-acid batteries, it is possible to obtain their capacity from widely reported data [50], obtaining 3.87 g Ah^{-1} for the negative electrode and 4.45 g Ah^{-1} for the positive electrode, giving the capacity shown in (2.12).

$$Q = \frac{1}{3.87 + 4.45} = 120 \text{ mAh g}^{-1} \tag{2.12}$$

However, the value obtained only considers the oxidation and reduction capacities of the electrodes, disregarding the rest of the battery components. In order to consider these values, the specific capacity is used and explained in the following subsection.

2.2.4 Specific capacity

The specific capacity is a practical way to measure the amount of energy stored in an actual battery, considering the physical characteristics of the materials used, such

as their molecular weight (Mw) and area (Ar), as well as their response to a known current density (I) such as the time it takes to reach its cut-off voltage ($t_{cut-off}$) [12]; all the above defined by equation (2.13).

$$Q_{specific} = \frac{I \cdot Ar \cdot t_{cut-off}}{3600 \cdot Mw} \tag{2.13}$$

This data is provided by the manufacturer in its datasheet or printed on the battery body, being this is the data used in front when referring to the battery capacity. However, this value depends on the applied or demanded current, so adjusting this data or considering an error present for applications is essential [12].

The primary information provided by the specific capacity is the time that a battery can deliver current, according to the level of consumption; this datum is expressed in times the capacity and is represented as C. Thus, if the capacity of a known battery is 300 mAh at 1C, it is equivalent to say that this battery can deliver 300 mA continuously for 1 hour, going from 100% charge to 0% [12].

Nevertheless, the batteries may require that current, a higher or lower, so the charging time that can deliver us change its expression, for the same battery mentioned above can be discharged to 4C, which would correspond to demand 1200 mA and give support for 15 minutes, otherwise is to discharge the battery to 0.2C, which is equivalent to a demand of 60 mA and support of 50 hours [12].

The information above describes the electrical characteristics of the battery, considering only the interaction of the active materials in the electrodes and the electrolyte. However, the energy storage capacity is not considered; for this purpose, the values of specific energy, energy density, and specific power are used [12].

2.2.5 Specific energy, energy density, and specific power

The specific energy represents the capacity of the battery to store energy per unit of available weight, whose units are Wh kg^{-1}, so it is possible to know the total weight of a battery bank for mechanical design purposes or to know the amount of energy available given the weight of the battery bank in question. It is necessary to consider the batteries' nominal voltage, specific capacity in ampere hour, and the weight obtained experimentally to obtain this metric. Equation (2.14) shows how the specific energy is estimated [12].

$$Specific\ Energy = \frac{Nominal\ Voltaje \cdot Specific\ Capacity}{Battery\ Weight} \tag{2.14}$$

On the other hand, the energy density corresponds to the amount of energy that can be stored in a battery per unit volume, whose units are Wh l^{-1}; both metrics seek to represent the available storage but are associated with different physical properties. Together, both metrics allow us to analyze the batteries from a mechanical point of view, with which it is possible to dimension the properties of the battery. The energy density can be calculated by equation (2.15), similar to equation (2.14). However,

instead of dividing by the weight of the battery in kg, it is divided by the volume of the battery in liters [12].

$$Energy\ Density = \frac{Nominal\ Voltaje \cdot Specific\ Capacity}{Battery\ Volume} \tag{2.15}$$

Complementary to the previous metrics, the specific power is the energy that the battery can deliver under a point load and is defined according to equation (2.16), where the nominal voltage, the maximum current that the battery can support uninterruptedly, and the weight of the battery are taken, all data provided by the manufacturer [12]. The units used for specific power are W kg^{-1}

$$Specific\ Power = \frac{Nominal\ Voltaje \cdot Maximum\ Current}{Battery\ Weight} \tag{2.16}$$

These three metrics allow us to know the energy storage and how it can be delivered; analogously, to understand their relationship, it is possible to visualize it through the illustrative example of the water bottle, where the amount of water that can be stored in the bottle corresponds to the specific energy or energy density. In contrast, the specific power is the amount of water that can immediately come out of the bottle [12].

According to its designed application, this datum is unique to each battery so it may vary from model to model within the same battery technology [12].

With the electrical characteristics seen so far, it is possible to know the ranges of a battery, thus allowing a selection to be made according to a given application, contemplating mechanical and electrical constraints. However, it is essential to know how all these characteristics interact as a whole and how they relate to an external current demand over time. For the latter, a mathematical model can be used, allowing the battery's performance to be monitored without the need to apply it directly to a battery in each case. There is a large number of possible models from different areas of science that seek to study batteries. However, two types of modeling have the most significant number of studies: electrochemical models and equivalent electrical circuit models [12].

2.3 Mathematical model

Many factors and uncertainties influence the complexity of the reactions occurring inside the battery, so establishing a mathematical model to describe their behavior is of relevance to both academia and industry; this requires a mathematical tool that depends on the data provided by the manufacturer and the available measurements [12].

2.3.1 Electrochemical model

The first and most apparent model to use is the electrochemical model, which allows us to model the battery response based on the reactions of the active material itself [66].

There are many possible models to address, but in general terms, it is necessary to describe the faradic reactions, those where charge transfer is involved, and non-faradic reactions, which modify the system response but do not depend on the charge transfer like geometry [67]. All these models can be summarized in the following steps:

- Describe the reactions and their kinetic constants for each electrode.
- Perform a mass balance to measure the rate of generation and consumption.
- Perform a charge balance where the reactions are related as a single electrical system.
- Estimate the transfer function with which faradaic reactions will be described.
- Add non-faradaic reactions to the model.

With these steps, we seek to develop a system based on the laws of conservation of matter and energy; in this way, it is possible to know the interaction of the internal reactions and how the internal energy is distributed [67].

Additionally, it is necessary to consider the amount of energy stored inside the battery at each moment, so the estimation of the state of charge and the open circuit voltage are carried out externally to complement the model obtained. Within the steps described, considerations of diffusion, concentration, and temperature are assumed [67].

This modeling strategy applies to any battery based on a redox reaction and will be discussed in detail in Chapter 4.

2.3.1.1 Lithium-ion batteries

Lithium or sodium batteries behave differently from batteries whose working principle is the redox reaction. However, their behavior is close, and to approach this type of battery from the electrochemical point of view is typically using the Pseudo-two-Dimensional (P2D) model, which contemplates two faces, solid during an open circuit and electrolyte during a closed circuit and three regions, positive electrode, negative electrode, and separator [12]; This model can be summarized in the following steps:

- Electrolyte phase, diffusion equations.
- Solid phase, diffusion equations.
- Electrolyte phase, Ohm's law equations.
- Solid phase, Ohm's law equations.

- Conservation of charge equation.
- Bulter-Volmer kinetic equation for surface active particles.

The first two steps describing diffusion are governed by Fick's second law, describing the ability of the materials to seek a homogeneous distribution depending on the concentration of particles, the active reaction area, the reaction coefficients of the materials, and the directions of particle movement [12].

The steps corresponding to the application of Ohm's law describe each phase's electrical behavior, the electrical potential, the reaction permittivity, the current applied to each phase, the concentration, and its interaction with temperature [12].

The conservation of charge allows us to obtain the total current flowing in the system relating to both reaction phases. Finally, the Bulter-Volmer kinetic equation relates the molar fluxes of each phase depending on their diffusion with the corresponding potentials, allowing us to know the battery's response to a known current input in a general way. In addition to the above, it is necessary to know the amount of energy stored depending on the state of charge, so this parameter is estimated using the concentration changes measured in the electrolyte [12].

The electrochemical model previously described superficially requires estimating many parameters that are impossible to measure, in addition to requiring information that the manufacturers do not necessarily share, so a laboratory experiment is required to obtain this information and indirectly estimate the remaining data [12].

Following this strategy, it is possible to obtain a mathematical representation of the battery's impedance dependent only on its potential; the rest of the phenomena must be considered additional to the model or the level of error it contains.

2.3.2 Equivalent electric circuit model

In order to simplify the understanding of the electrochemical model, one of the most widely used strategies is the application of equivalent electrical circuits, where it is well known that the electrochemical reactions are represented by electrical elements whose dynamic response is similar; in this way, an electrical model whose response is similar to the battery, however, as it is a representation with equivalent dynamics, the elements that make it up may not have a direct meaning to the electrochemical reactions [68].

The equivalent electrical circuit is built based on the time response of the battery, and a circuit with a similar response is built; for this purpose, the elements listed in Table 2.2 are used [68].

Due to its empirical nature, there are a variety of different equivalent electrical circuits used. However, their construction or proposal does not only arise from chance; they are proposed through different studies, aiming to adjust the dynamic response with a circuit that is as simple as possible [68].

Among the elements available are the constant phase elements and the Warburg impedance, described in their frequency response as fractional systems. The estimation

of this type of element is usually tricky [68], which is why it is used any of the following definitions:

- Grünwald-Letnikov.
- Riemann-Liouville.
- Caputo.

All approaches to representation at the time of its response. This modeling strategy will be described in depth in the following chapters.

One of the characteristics of this model strategy is that the mathematical description represents the impedance of the battery, contemplating variations and phenomena that not only depend on its potential but, as in the electrochemical model, it is necessary to calculate the open circuit voltage independently that completes the representation [68].

Table 2.2: Elements are commonly used to construct an EEC representing a battery.

Element Name	Symbol	Description
Power source	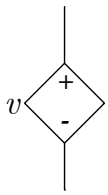	This element represents the energy stored in the battery and the open circuit voltage available to deliver said energy.
Resistor	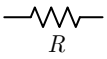	This element represents a voltage drop where the stored energy is dissipated when interacting with a demanded current.
Capacitor		This element represents a voltage storage response, which is related to the rates of the reactions.
Coil		This element represents a current storage response; this phenomenon is related to changes in the current demand.
Constant phase element		This element has a behavior similar to that of a capacitor, typically treated as a real capacitor, which has a slight variation dependent on the applied frequency.
Warburg impedance		This element represents a semi-infinite diffusion phenomenon, which represents a hole on the surface of the electrodes.

According to the aforementioned general descriptions of the contemplated model strategies, the characteristics of each model are deduced and summarized in Table 2.3.

Table 2.3: Main characteristics of the leading modeling strategies used to represent batteries.

• Equivalent electric circuit model.	• Electrochemical model.
• Electrical parameters. • Application of circuit theory. • Non-explicit general function of Z of the potential. • Not every phenomenon is represented by electrical elements. • More applicable approach.	• Physico-chemical parameters. • Reaction kinetics. • General explicit Z function of the potential. • It is necessary to complete the model with non-faradic reactions.

Considering the characteristics described above and seeking to ensure that the work developed will be useful for the emerging engineering applications, it was decided to address the problem with an equivalent electric circuit model that will be described in the following chapters.

Chapter 3

Equivalent electric circuit model based on time response

In this chapter an EEC model is studied to analyze the feasibility to represent aging phenomena through the parametric variation by using a recursive least squares algorithm, establishing its limitations. Then, a particular study case to represent the corrosion mechanism is evaluated.

3.1 EEC model description

An EEC model approximation of the battery is widely used for engineering applications. It defines battery response with known electrical elements that closely coincide with the observed behavior [68].

The model follows the typical configuration of a Thevenin EEC, from left to right, the model of Figure 3.1 has an open circuit voltage (v_{OC}) dependent on the SOC, since it means the voltage for the stored energy available at a given moment, so this parameter should be online estimated [12].

Since the response of the battery when delivering or receiving energy is not instantaneous, elements that describe the transient response are added, which in all battery technologies follows a sigmoid response, so they can be approximated as an arrangement of resistive and capacitive elements. A resistance R_0 along with two RC parallel arrangements, representing the power that the battery is capable of delivering [32, 68], the terminal voltage (v_{batt}) which shall be considered as the output, and the demanded current (i) which shall be considered as the input.

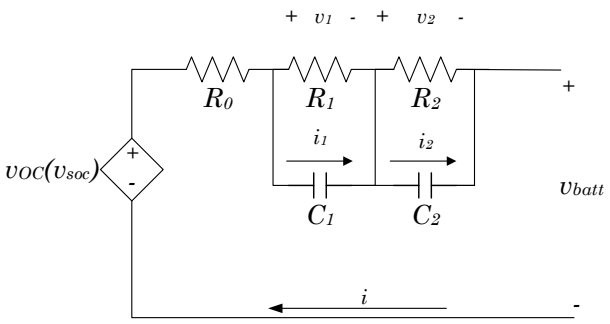

Figure 3.1: Equivalent Electric Circuit (EEC) for the battery modeling.

In a simplified way, the model has three essential elements:

- Measurable variables: The terminals measurable voltage (v_{batt}) considered in this work as the output, the battery current (i) considered in this work as the input [4], and the temperature that for this work is considered constant.
- Dynamic response parameters: Represented by the resistors and capacitors in the used model. R_0 represents the instantaneous relationship between voltage and current, and the other elements, the transient response splitting the dynamic in time constants following the sigmoid response [32].
- Battery states: Representing the energy storage and its change due to use conditions [69].

The mathematical representation of the EEC used is a well-established state-space model derived from Lagrangian energy equations, as detailed in [70] and presented in equation (3.1).

$$\begin{bmatrix} \dot{v_1} \\ \dot{v_2} \end{bmatrix} = \begin{bmatrix} -\frac{1}{R_1 \cdot C_1} & 0 \\ 0 & -\frac{1}{R_2 \cdot C_2} \end{bmatrix} \cdot \begin{bmatrix} v_1 \\ v_2 \end{bmatrix} + \begin{bmatrix} \frac{1}{C_1} \\ \frac{1}{C_2} \end{bmatrix} \cdot i \tag{3.1}$$
$$v_{batt} = \begin{bmatrix} -1 & -1 \end{bmatrix} \cdot \begin{bmatrix} v_1 \\ v_2 \end{bmatrix} + \begin{bmatrix} -R_0 \end{bmatrix} \cdot i + v_{OC}(v_{SOC})$$

where v_1 corresponds to the voltage in the parallel arrangement R_1C_1 and v_2 corresponds to the voltage in the parallel arrangement R_2C_2.

3.2 Model parameter identification

For the selected EEC model, and considering that the battery used as experimental case is a VRLA PS-260 battery of 2 V and 6 Ah, it is necessary to parameterize the

passive elements R_0, R_1, R_2, C_1, and C_2. The method used is the one proposed by Plett [4] that obtains the parameters based on the response to a discharge pulse. This test is illustrated in Figure 3.2, where the values of Δi and Δv correspond to the instantaneous changes, obtaining the value of R_0 using Ohm's law from these.

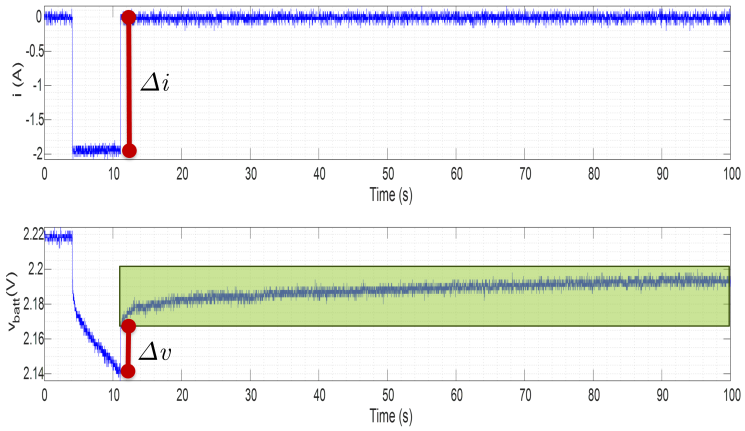

Figure 3.2: Discharge pulse response to parameterize the model passive elements.

From the information in the green box and using a fitting exponential function from MATLAB, as the one shown in equation (3.2), the rest of the passive elements are characterized.

$$f(x) = ae^{bx} + ce^{dx} \tag{3.2}$$

For this, we consider the output equation from the system (3.1) as shown in (3.3).

$$v_{batt} = v_{OC}(v_{SOC}) - v_1 - v_2 - R_0 i \tag{3.3}$$

where v_{batt} and i are known since they are being measured, the previously calculated value of R_0 is used, and the measurements are taken at a known SOC point, so v_{OC} is also known, typically using the 100% of SOC and the discharge pulse applied is small enough to despise the change in the SOC, considering that v_1 and v_2 correspond to the voltage in each parallel arrangement RC, could be rewrite as exponential functions, leaving only the elements at the right of the equal in equation (3.4) to correlate to equation (3.2). Under this consideration, it can be seen that both equations have similar structures, allowing the coefficients of the exponents of the fitted function (3.2) to be equal to the coefficients of the exponents in equation (3.4), where since i is known, only remains as unknown resistance values. In the same way, the exponents are equalized, considering that the independent variables are x for equation (3.2) and t for equation (3.4), thus obtaining the values of the capacitors. For this, the value of $i{=}\Delta i$ [4].

$$v_{batt} - v_{OC} - iR_0 = -R_1 ie^{-t/(R_1C_1)} - R_2 ie^{-t/(R_2C_2)} \tag{3.4}$$

For a Power Sonic PS260 VRLA battery from 2 V to 6 Ah, the parameters obtained are shown in Table 3.1.

Table 3.1: Experimental parameters for obtained from Power Sonic PS260 VRLA battery.

Parameter	Value
R_0	0.0088 Ω
R_1	0.0211 Ω
R_2	0.0463 Ω
C_1	114.7717 F
C_2	18527 F

3.3 Open circuit voltage

It is essential to clarify that the v_{OC} value cannot be measured online. However, representing the amount of stored energy related to the state of charge voltage (v_{SOC}), expressed as the amount of charge in an interval between 0 V and 1 V [4]. The latter has the advantage that it can be estimated. One of the simplest methods used is Coulomb Counting, described by the equation (3.5).

$$v_{SOC}(t) = v_{SOC}(0) - \frac{\int_0^t \eta \cdot i \cdot dt}{C_{available}} \tag{3.5}$$

where $v_{SOC}(t)$ is the SOC voltage at the desired time t, $v_{SOC}(0)$ is the SOC voltage at the initial time, η is an additional correction factor which is considered 1 for simplicity since their values are close to this number, and to complete the model, it is necessary to continually adjust the value of $C_{available}$, which corresponds to the remaining capacity within the battery and changes with the passing of the use cycles. In equation (3.5), $C_{available}$ corresponds to the practical capacity provided by the manufacturer, and it will decay as the battery ages. Then, the method described in equation (3.6) is used to upgrade the value of $C_{available}$, which is obtained from Coulomb Counting [4].

$$C_{available} = \frac{1}{\Delta v_{SOC}} \int_{t_0}^{t_1} i(t)dt \tag{3.6}$$

where t_0 is the initial time for evaluation, t_1 is the final time for evaluation, Δv_{SOC} is the change in the v_{SOC} between t_0 and t_1. It is necessary that Δv_{SOC} be different from 0.

That is why the v_{SOC} is used to estimate the v_{OC}, which has a correlation. Depending on the model's application and the required precision level, this assessment

can be described differently. The first approach is to consider the relationship between both variables as proportional. For this, the data provided by the datasheet is taken as the voltage under charge, considered the v_{OC} at 100% SOC (2.18 V for this battery case), and the final voltage, considered the v_{OC} at 0% SOC (1.7 V for this battery case) [71]. Figure 3.3 shows this proportional relationship graphically.

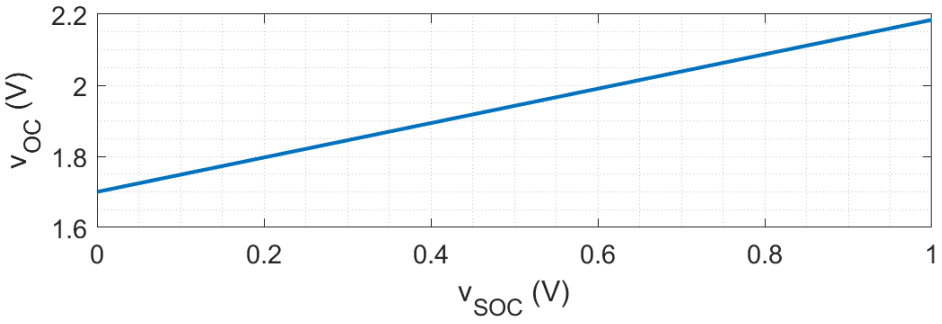

Figure 3.3: Open-circuit voltage versus state-of-charge voltage considering a lineal relationship.

This approximation is valid in contexts where the application can work with the error produced by this simplification. However, the behavior of the v_{OC} is non-linear, and if we seek to represent this relationship more precisely, it is necessary to explore other ways to approximate it.

One of the ways to approximate this correlation is through a discharge by controlled pulses [2, 12]. The method consists of taking a previously charged battery up to 100% in new optimal conditions following the manufacturer's instructions and subsequently discharging the battery at a known rate, typically close to 0.2 C, in time intervals that coincide with a 5% SOC, allowing the battery to rest long enough until v_{batt} stabilizes, typically close to 30 minutes. The steady-state value is taken as the corresponding v_{OC} value because, in rest time the battery is at open circuit, and when the voltage is stabilized the difference between v_{OC} and v_{batt} are minimal, approximating the behavior of the battery [72, 73]. This process is repeated until the battery is completely discharged.

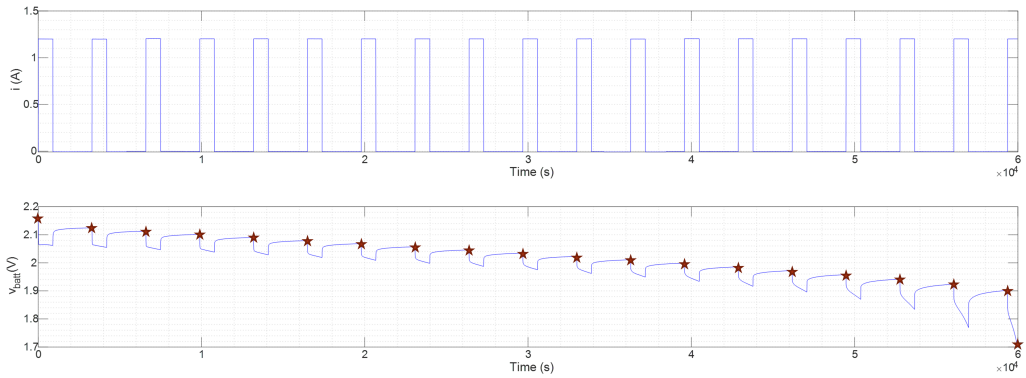

Figure 3.4: Total discharge test by controlled pulses to estimate the relationship between v_{OC} and v_{SOC}.

Figure 3.4 shows the pulse discharge method previously described. As the discharge pulses are carried out at 0.2 C and the time that each pulse lasts is known, the percentage of charge remaining after each pulse can be estimated. The points marked with a star indicate the v_{batt} value that better approximate the v_{OC}, value on that moment, located in the voltage stabilization point [73]. The data obtained allows to approximate the relationship between the v_{SOC} and the v_{OC}, the corresponding values are in Table 3.2. displayed graphically in Figure 3.5 in triangles; However, it is necessary to know the value of this relationship for each one of the SOC points, for this adjustment there is not a specific function, hence, it was proposed to use a polynomial function. Therefore, to fit these points to a polynomial function, MATLAB software was used. For the selection of the fitting function, using the smallest order function that would fit all the measured points was taken as a criterion. Therefore, in Figure 3.5 the red line shows the fitted fifth-order function and the blue triangles are the measurements put together in Table 3.2.

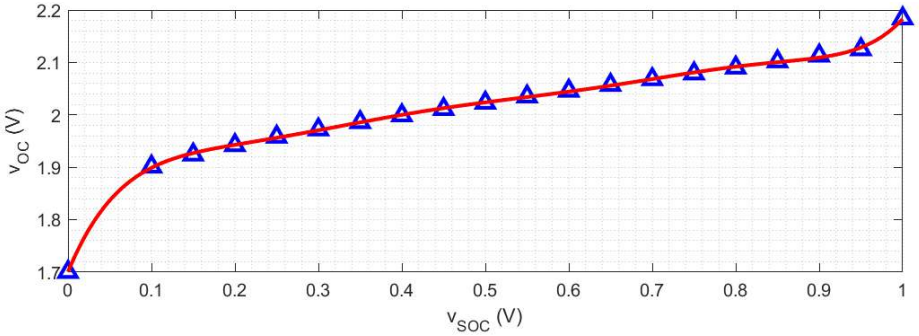

Figure 3.5: Open-circuit voltage versus state-of-charge voltage curve

Table 3.2: v_{OC} and v_{SOC} values experimentally obtained from the total discharge test by controlled pulses.

v_{OC}	v_{SOC}	v_{OC}	v_{SOC}	v_{OC}	v_{SOC}
2.184	1.00	2.057	0.65	1.972	0.30
2.125	0.95	2.046	0.60	1.958	0.25
2.113	0.90	2.035	0.55	1.942	0.20
2.102	0.85	2.023	0.50	1.924	0.15
2.090	0.80	2.011	0.45	1.901	0.10
2.079	0.75	1.999	0.40	1.700	0.00
2.068	0.70	1.986	0.35		

This relationship is expressed mathematically in the equation. (3.7).

$$v_{OC}=2.357\cdot(v_{SOC})^5-5.963\cdot(v_{SOC})^4+5.624\cdot(v_{SOC})^3-2.442\cdot(v_{SOC})^2+0.6952\cdot(v_{SOC})+1.912 \tag{3.7}$$

The adjustment of the points is not restricted to using a polynomial function, so different types of functions or combinations of these can be used interchangeably.

3.4 Equivalent electric circuit model

Using the information obtained from the passive elements and incorporating the estimate of v_{SOC} given in (3.5), the state-space model (3.8) is constructed; for this, Kirchhoff's laws are applied to the EEC model in Figure 3.1 [4].

$$\begin{aligned} \dot{\mathbf{x}}_a &= \mathbf{A}_a\mathbf{x}_a + \mathbf{B}_a i \\ v_{batt} &= h(\mathbf{x})_a + \mathbf{D}_a i \end{aligned} \tag{3.8}$$

where $\mathbf{x}_a \in \mathbb{R}^3$, $i \in \mathbb{R}$, and $v_{batt} \in \mathbb{R}$; defining the matrixes $\mathbf{x}_a$, $\mathbf{A}_a$, $\mathbf{B}_a$, and $\mathbf{D}_a$ as (3.9) [4].

$$\begin{aligned} \mathbf{x}_a = \begin{bmatrix} v_1 \\ v_2 \\ v_{SOC} \end{bmatrix}; \mathbf{A}_a = \begin{bmatrix} -\frac{1}{\tau_1} & 0 & 0 \\ 0 & -\frac{1}{\tau_2} & 0 \\ 0 & 0 & 0 \end{bmatrix}; \\ \mathbf{B}_a = \begin{bmatrix} \frac{1}{C_1} \\ \frac{1}{C_2} \\ -\frac{1}{C_{available}} \end{bmatrix}; \mathbf{D}_a = \begin{bmatrix} -R_0 \end{bmatrix}; \end{aligned} \tag{3.9}$$

Likewise $h(\mathbf{x})_a$ is the function (3.10) and the parameters τ_1 and τ_2 represent the multiplication of R_1C_1 and R_2C_2, respectively.

$$h(\mathbf{x})_a = -v_1 - v_2 + v_{OC} \tag{3.10}$$

The function $h(\mathbf{x})_a$ can complicate the model because it contains the function v_{OC}, which can be linearized, generating a linear state space, or can be defined by the polynomial equation (3.7), which adds nonlinearity.

As is evident from everything described in the model, the definition of the v_{OC} modifies its complexity; with all cases being correct, the selection of any of them depends entirely on the restrictions of the application and the precision sought. To delve deeper into these differences are presented 3 different cases:

- The model considers the v_{OC} to be lineal.
- The model considers the v_{OC} as a piecewise linear function.
- The model considers the v_{OC} as a polynomial function.

For this purpose, a charge and discharge cycle at 0.2 C was used in a battery without wear. Once analyzed, the results are compared with the charge and discharge cycle measurements at 0.2 C in a battery with 200 wear cycles.

3.4.1 Model considers the v_{OC} lineal

In this case, the v_{OC}, when is lineal, is defined by a reactant line whose equation is described in (3.11), using the data previous mention to plot the figure 3.3. This way, building a complete model using the previous data is possible.

$$v_{OC} = 0.484 v_{SOC} + 1.7 \tag{3.11}$$

Figure 3.6 shows the validation of the model in this case; the blue line (v_{batt} Measured) shows the voltage measurements after being subjected to the charge and discharge cycle. The red line (v_{batt_p} Simulated) shows the model's behavior using v_{OC} as a lineal relationship. It can be observed that the charging stops at 10500 s, followed by a rest time of 50 s, then the discharge process starts.

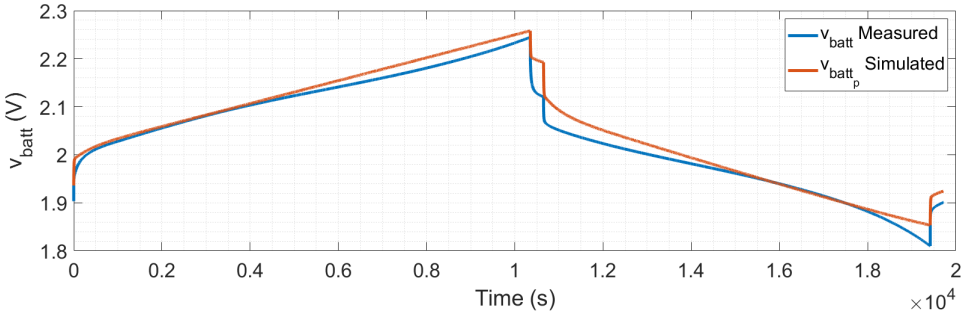

Figure 3.6: Battery voltage measured and simulated for v_{OC} as proportional function.

It can be seen how the model's response to the current input follows similar behavior than the measurements. However, there is a difference between them due to the following reasons:

- The model considers constant resistances and capacitances [68] and a linear v_{OC} function.
- There are phenomena that are not represented in a 2-RC parallel arrangement.

This difference can be observed in detail in Figure 3.7, where the relative error between this model and the measurements is always smaller than 3.5%, observing that the error is near to zero and the most significant values are in the the transitions, considering that the cell-to-cell variation allowed in VRLA batteries is around 5% [74], this model represents a good approximation.

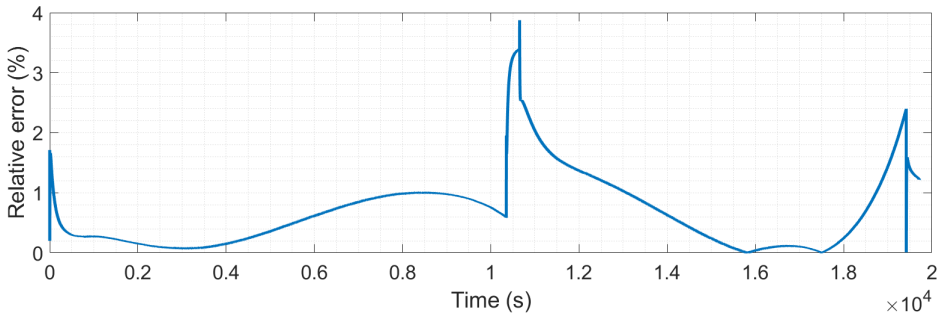

Figure 3.7: Relative error between battery voltage measurements and model simulation considering v_{OC} as proportional function.

In this case, it can be seen how the simulated voltage has a transient period produced by the dynamic response parameters. After that, the response has a linear behavior, so its growth is a straight line, both in charging and discharging; this allows to easily predict the time it will take to reach some SOC point of interest.

3.4.2 Model considers the v_{OC} piecewise linear

The previous case simplifies the behavior of the v_{OC}. However, it is necessary to know its behavior in detail for some applications. One of the ways to address this problem is through a piecewise function, which allows us to know the changes in v_{OC} but maintains a linear system. There is not a specific number of sections used for this methodology, hence it was decided to use 100 sections to reproduced the v_{OC} behavior, closer to Figure 3.5. Therefore, the v_{OC} is defined by equation (3.12), where each section corresponds to the equation of a straight line.

$$v_{OC} = \begin{cases} 2.184v_{SOC} + 0 & if \quad 0 < SOC < 1 \\ 0.3935v_{SOC} + 1.7905 & if \quad 1 < SOC < 2 \\ 0.3832v_{SOC} + 1.8007 & if \quad 2 < SOC < 3 \\ \vdots & \vdots \quad \vdots \\ 0.2868v_{SOC} + 1.936 & if \quad 99 < SOC < 100 \end{cases} \tag{3.12}$$

Figure 3.8 shows the validation of the model for the new v_{OC} condition, where the blue line (v_{batt} Measured) corresponds to the voltage measurements. In contrast, the red line ($v_{batt_{pl}}$ Simulated) shows the behavior of the updated model. It can be observed that the charging stops at 10500 s, followed by a rest time of 50 s, then the discharge process starts.

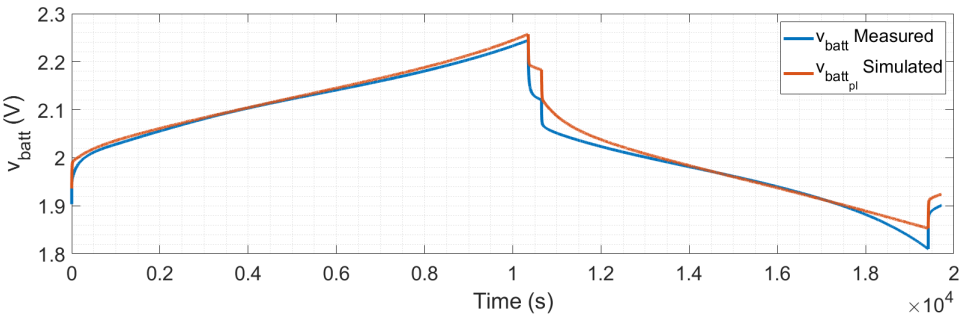

Figure 3.8: Battery voltage measured and simulated for v_{OC} as a piecewise linear function.

As it can be seen, the model's behavior is closer to that obtained with a lineal v_{OC}, but there are still differences due to the consideration of constant parameters, linear v_{OC} and phenomena that cannot be represented by the EEC model, this differences are evident in Figure 3.9, which shows the relative error approaches zero. However, during transients, the error continues to increase but in this case is smaller than 3%.

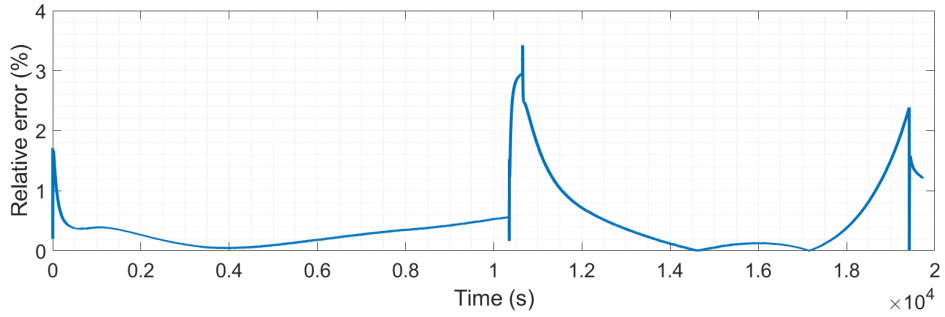

Figure 3.9: Relative error between battery voltage measurements and model simulation considering v_{OC} as piecewise lineal function.

As in the previous case, a transient behavior can be observed when the battery voltage changes; however, the rest of the behavior is no longer proportional and better approximates the variations present in the measurements. In this way, the model's response is improved, and the linearity characteristic of the system is maintained; this is an advantage for many applications since the mathematical analysis does not present complications. The tracking obtained is considered good enough. However, the computation of this model increases since the v_{OC} function must be stored and selected according to the SOC being worked.

3.4.3 Model considers the v_{OC} polynomial

The previous cases seek to linearize the model by simplifying its calculation, however there is information that is lost in the process, so the v_{OC} was approximated using a fifth order polynomial (3.7) mentioned previously. This model is nonlinear, with the peculiarity that the nonlinearity appears in the model output.

Figure 3.10 shows the validation of the model for the nonlinear v_{OC} condition, where the blue line (v_{batt} Measured) corresponds to the voltage measurements. In contrast, the red line ($v_{batt_{pol}}$ Simulated) shows the behavior of the nonlinear model. It can be observed that the charging stops at 10500 s, followed by a rest time of 50 s, then the discharge process starts.

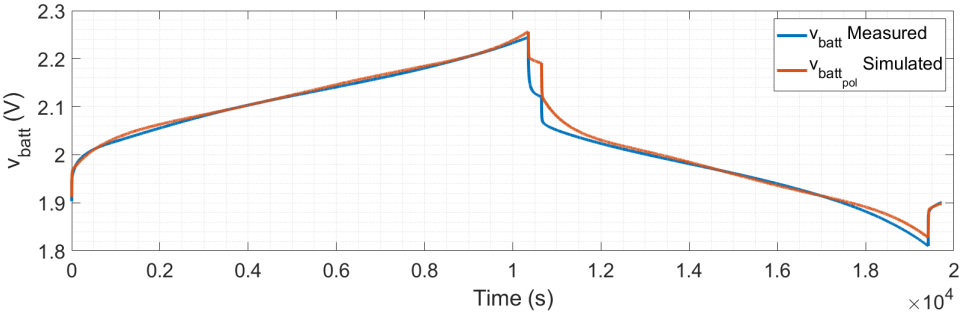

Figure 3.10: Battery voltage measured and simulated for v_{OC} as fifth order polynomial function.

The behavior of the model for this case follows the variations of the measurements better than the previous two cases, however, during transients the performance of the piecewise linear model is better, the error in this point corresponds to the variation of the parameters and phenomena that cannot be represented by the EEC model. This can be seen in detail in Figure 3.11, which shows the relative error present in this model, it stands out how the error during the transient reaches 3.8%. However, during the rest of the test the error does not exceed 1%, presenting best tracking on average.

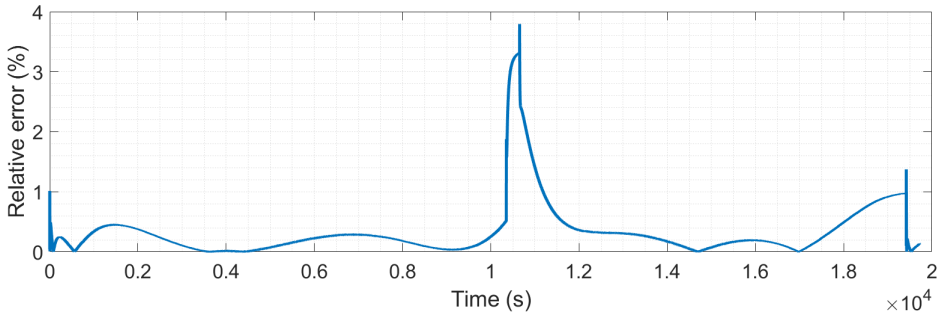

Figure 3.11: Relative error between battery voltage measurements and model simulation considering v_{OC} as fifth order polynomial function.

Unlike the previous cases, none of the responses maintain a proportional growth or decrease, however, it better follows the changes present in the battery. On the other hand, the error when a transient occurs is greater, however, in all cases the error obtained is less than the cell-to-cell variation present in VRLA batteries, typically 5% [74]. This case allows us to monitor the changes in the battery very well, however the mathematical complexity is greater than in the rest of the cases and the computational cost is greater than that of the linear case, but equal to that of the linear case in sections, due to because the complexity of the operations in this case is compensated by the memory necessary to store the 100 linear sections.

For all the previous simulations, the Coulomb Conting method (3.5) was used to estimate the state of charge of model (3.8), shown in Figure 3.12.

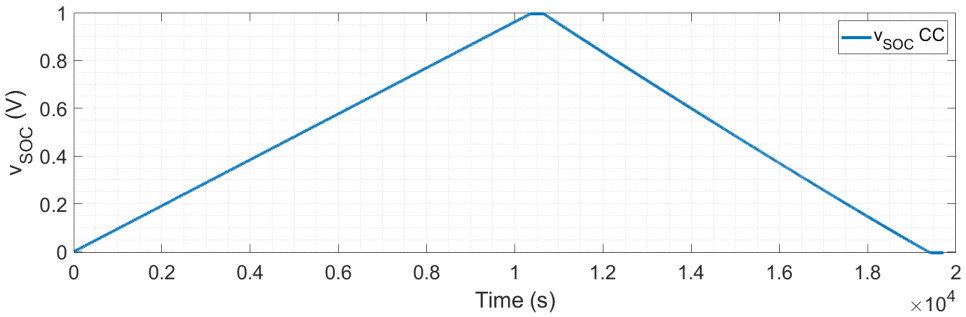

Figure 3.12: SOC estimated by coulomb counting method in a full charge/discharge cycle.

From the results shown in each case it is possible to concentrate their characteristics, benefits and scopes as shown in Table 3.3, evidencing that each case of the EEC model can cover different application requirements. The errors shown in the Table 3.3 correspond to the specific case of the VRLA battery used.

Table 3.3: v_{OC} model cases comparative behavior and applications.

Method	Characteristics	Disadvantages	Error
v_{OC} proportional	• Linear behavior throughout the charge and discharge process. • v_{OC} is described with a multiplication and an addition. • Make easy to predict the remaining time for full charge or full discharge. • Low computational cost. • Low memory required.	• The transitory variation are not represented. • The tracking shows greater variation.	3.3%
v_{OC} piecewise linear	• Concerted its linear characteristics. • Represents transitory changes. • v_{OC} is described with a multiplication and an addition. • Less variation during charge process.	• Memory required for each peace. • Medium computational cost • Tracking during download has errors.	3.0%
v_{OC} polynomial	• Better tracking during the entire loading and unloading cycle • Less error during transients • Accurate battery representation.	• High computational cost • Increased error during instantaneous changes. • v_{OC} is described as nonlinear system	3.8%

Each case has slightly different characteristics; this does not mean that any model is better or worse, but rather that it depends on the application and its restrictions on which case is best suited. For the purposes of the thesis work presented, the v_{OC} is used as a fifth order polynomial function, since it is intended to represent the behavior of the battery as accurately as possible during charge and discharge, prioritizing the smallest errors in steady state.

However, these models tend to diverge as the battery ages because they are time-invariant models, as is observed in Figure 3.13, where simulations of a charge/discharge cycle with a battery with 200 aging cycles. It can be observed that the error increases significantly.

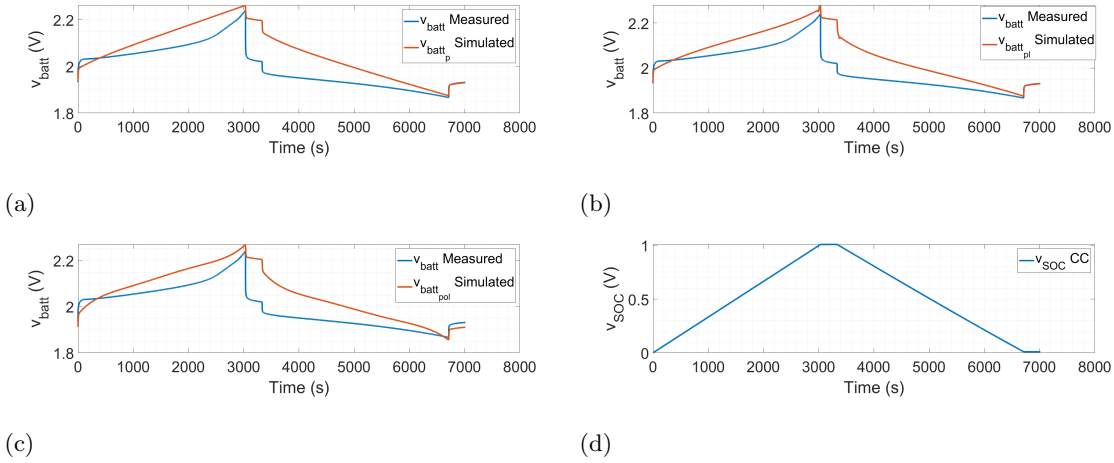

Figure 3.13: Simulation with different v_{OC} consideration in a battery with 200 aging cycles. (a) v_{OC} as proportional. (b) v_{OC} as piecewise linear function. (c) v_{OC} as polynomial function. (d) v_{SOC} estimated by Coulomb Counting method.

Therefore, considering that the battery model changes monotonically in its parameters due to SOC and SOH [28], equation (3.13) represents the models where their matrices reflect the parametric variations due to both SOC and SOH. Thus, the models by columns express variations due to the SOC from 100% to 0%, and by rows due to the SOH from the beginning of the life to the end of the life.

$$\begin{array}{ccc} \dot{\mathbf{x}} = \mathbf{A}_{sb}\mathbf{x} + \mathbf{B}_{sb}u & \cdots & \dot{\mathbf{x}} = \mathbf{A}_{se}\mathbf{x} + \mathbf{B}_{se}u \\ y = h(\mathbf{x}) + \mathbf{D}_{sb}u & & y = h(\mathbf{x}) + \mathbf{D}_{se}u \\ \vdots & \ddots & \vdots \\ \dot{\mathbf{x}} = \mathbf{A}_{fb}\mathbf{x} + \mathbf{B}_{fb}u & \cdots & \dot{\mathbf{x}} = \mathbf{A}_{fe}\mathbf{x} + \mathbf{B}_{fe}u \\ y = h(\mathbf{x}) + \mathbf{D}_{fb}u & & y = h(\mathbf{x}) + \mathbf{D}_{fe}u \end{array} \tag{3.13}$$

where the subscripts s correspond to the beginning of the SOH, f correspond to the end of the SOH, b represents 100% of the SOC, and e represents 0% of the SOC.

3.5 Electrochemical reactions in a VRLA battery

The state of health SOH usually characterizes the aging of batteries, giving information on the available energy retention and comparing it with the datasheet specifications.

Usually, the SOH is estimated by using the battery capacity in ampere-hours according to equation (3.14):

$$SOH_C(\%) = \frac{C_{available}}{C_{nom}} \times 100\% \tag{3.14}$$

where C_{nom} is the nominal capacity given at the datasheet, $C_{available}$ is the available capacity, estimated by the formula (3.15):

$$C_{available} = -\int_{t_0}^{t} \frac{i(t)}{SOC(t) - SOC(t_0)} dt \tag{3.15}$$

where $i(t)$ is the battery current, t_0 is the initial time, t is the time as variable, $SOC(t)$ is the SOC in time t, and $SOC(t_0)$ is the SOC in time t_0. Additionally is possible to estimate the SOH based on the internal resistance defined as (3.16):

$$SOH_R(\%) = \frac{R_{eol} - R_{now}}{R_{eol} - R_{new}} \times 100\% \tag{3.16}$$

where R_{eol} is the internal resistance at the end of life, R_{new} is the internal resistance at the start of the lifetime, these two values are given by the manufacturer, R_{now} is the current value of internal resistance, this last value could be estimated and approach accurately the SOH.

The SOH gives general information about battery degradation and retention capacity losses. This phenomenon is due to aging mechanisms. These mechanisms could be divided for lead-acid batteries in corrosion, hard sulfation, and active material loss.

3.5.1 Battery corrosion

Battery corrosion is a natural process in a lead-acid battery due to the redox reaction in charge of energy storage and delivery. As the battery ages, some particles fail to reconstitute properly, specifically on the positive electrode reaction in equation (3.17), the recomposition of lead dioxide (PbO_2) is incomplete, producing non-stoichiometric lead oxide (PbO_x), where x is a value greater than one but less than two [75, 76].

$$PbO_2 + 4H^+ + SO_4 \Leftrightarrow PbSO_4 + 2H_2O - 2e^- \tag{3.17}$$

PbO_x creates a non-reactive material, creating a passive layer that modifies the battery dynamics. This phenomenon is accentuated when the battery is exposed to high temperatures or is over-charged [1].

3.5.2 Battery hard sulfation

Lead sulfates ($PbSO_4$) are the natural product of the battery when discharged; in the same way, these sulfates dissolve when charging the battery. However, some sulfates fail to dissolve throughout their useful life, producing hard sulfation. This phenomenon is accentuated when the battery is exposed to deep discharge or over-discharge, modifying the v_{OC} in rest conditions; this produces a loss of active material and interferes with the diffusion process [1, 77].

3.5.3 Battery loss of active material

As a result of the constant charging and discharging of the battery and under the aforementioned aging mechanisms, the amount of available active material changes throughout its useful life. These changes modify the surface reactions of the electrodes and the instantaneous electrode-electrolyte [37].

3.5.4 Battery time reaction

The aging mechanisms described above occur at the same time, and although there are conditions that accelerate some of them, it is difficult to distinguish between them; however, works such as [1] indicate a difference between reactions, highlighting this work as the dynamics of the following processes:

- Electrical and magnetic effects (around μs and ms).
- Effects on the electrical double layer (around ms and s).
- Mass transport effects (around s and h).

The full spectrum of time reactions is shown in Figure 3.14.

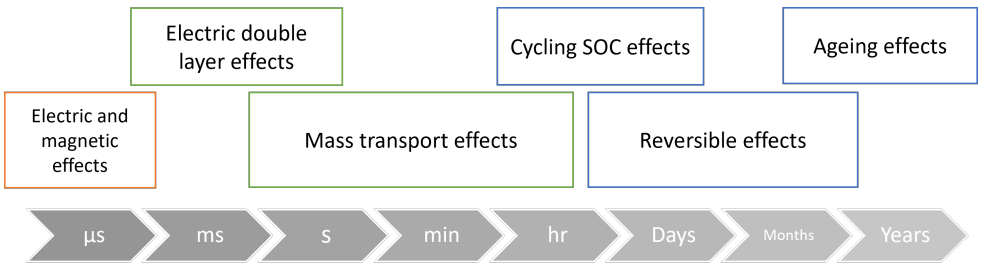

Figure 3.14: Dynamic processes in batteries and their average reaction time [1].

According to this information and limiting the scope to the description of the previous aging mechanisms, it is possible to associate but not restrict to an unknown time constant with a relationship concerning the other mechanisms.

The rate at which active material is lost from the battery is the fastest mechanism, mainly impacting the electrode's electrical behavior and surface interactions. Corrosion follows, affecting the electrode composition and its interface with the electrolyte at a slower pace. Lastly, hard sulfation occurs at the slowest rate, mainly influencing diffusion and mass transport within the battery.

3.6 Parameter variation identification

Due to the parametric variations present in the model, it is formulated the idea of being able to identify abnormal behaviors in the battery through the parametric changes.

To approach the problem from this point of view we replicated the work [2], in which the EEC model is parameterized by means of Recursive Least Squares (RLS) with forgetting factor, deciding to follow this path since in the reported work a similar model is used, with conditions close to the batteries used for this thesis and the application obtained good results for lithium batteries.

To verify these results, the model developed above was fitted to the circuit shown in Figure 3.1, with the following assumptions:

A1 The temperature is constant at room temperature.

A2 The $v_{OC}(v_{SOC})$ is known, previously calculated by a Coulomb Counting method (3.5).

As reported in [2], the algorithm is developed to estimate the parameters according to the flowchart shown in Figure 3.15.

As validation of the correct operation of the recursive least squares algorithm, measurements of a charge/discharge cycle of a new battery were used, obtaining the results shown in Figure 3.16, where the blue line shows the measured voltage (v_{batt}) and the red line shows the tracking of the algorithm, showing how at the beginning the values try to adjust, presenting jumps, but after a few iterations it converges and makes a reliable fitting.

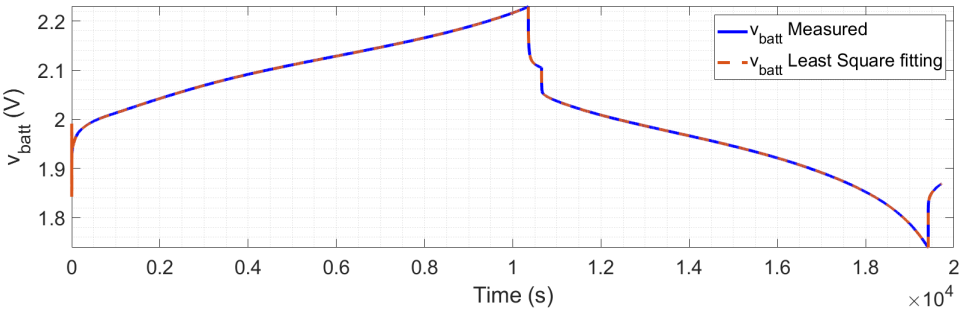

Figure 3.16: Battery voltage measurements and fitting by RLS algorithm.

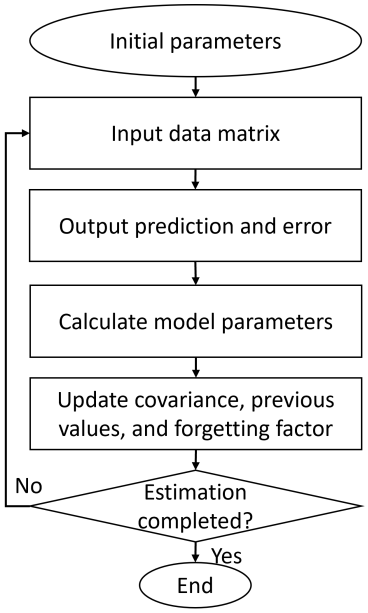

Figure 3.15: Flowchart of the RLS algorithm with adaptive forgetting factor [2].

Having shown that the parameterised model follows the battery behaviour, each parameter is analysed in detail. Figure 3.17 shows the changes of the resistors and capacitors, observing how these parameters have smooth changes, in some cases imperseptible, along the charge and discharge, the only notorious change is due to the transition from charge to discharge.

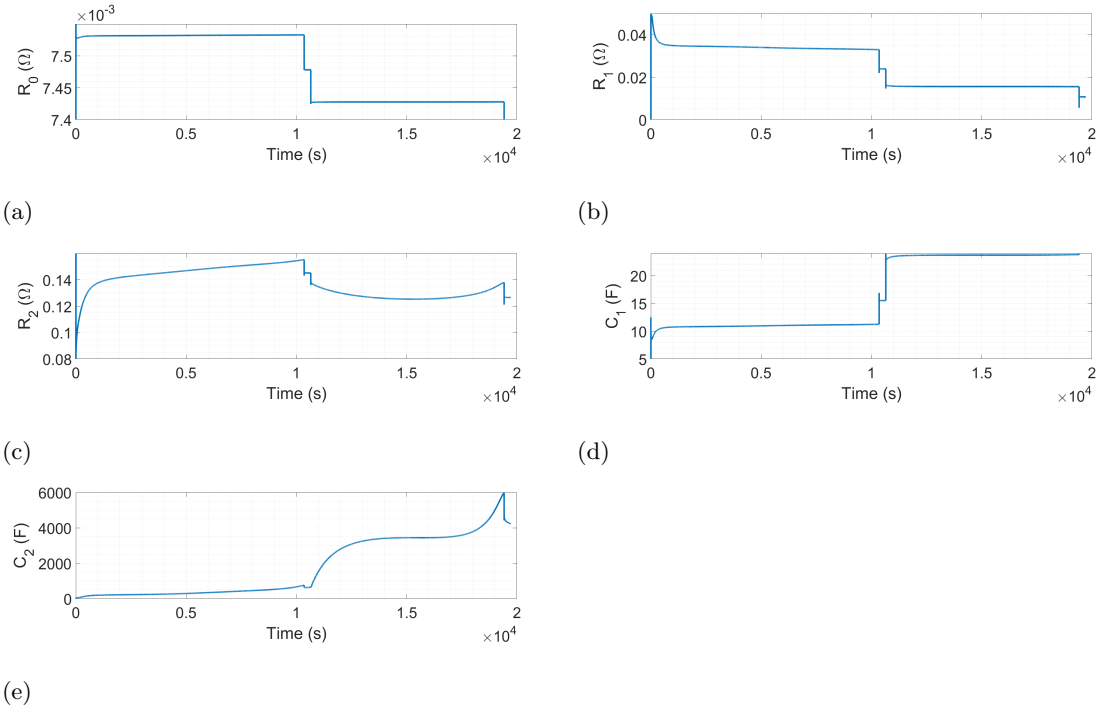

Figure 3.17: Parameter fitting evolution through charge/discharge cycle for new battery. (a) R_0, (b) R_1, (c) R_2, (d) C_1, and (e) C_2.

In order to know the behavior of the battery throughout its useful life, VRLA Power Sonic PS-260 batteries were tested, which were aged for 200 cycles.

3.6.1 Aging battery test for data recording

This test was formulated to record voltage and current measurements through the useful life of eight series-connected batteries, considering 200 full charge/discharge cycles. Figure 3.18 shows the schematic of the setup, the RTAC SEL-2240 was used to program the switching logic of the switches SW 1 and SW 2 to charge and discharge the battery, and to record the eight voltages and the chain current in floating data format collected every 50 ms in a structure that will be recorded in a csv file, creating a file each full charge/discharge cycle, automatically. The charger is a direct current source, which delivers constant current at a maximum voltage equal to the float voltage of the battery (2.25 V). The load consists in a resistance (R_{LOAD}) of 13.3 Ω.

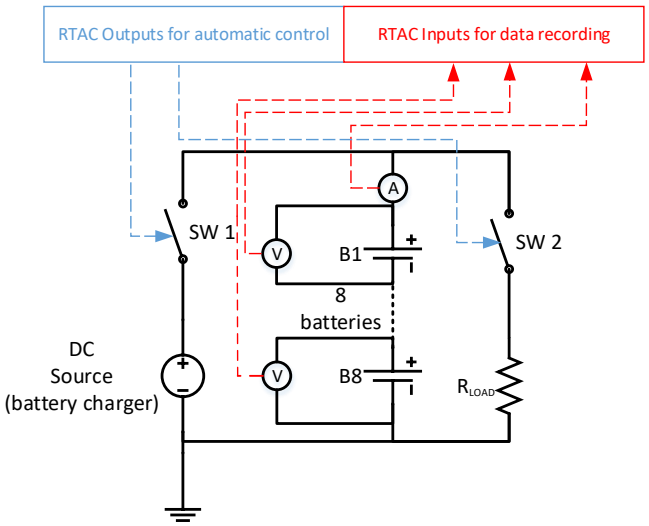

Figure 3.18: Battery aging test circuit.

The batteries were subjected to a charge and discharge profile that responds to the IEC 60095-1 standard, shown in Figure 3.19. While the voltage limits are established according to the discharge characteristics given by the manufacturer, with the maximum operating voltage being 2.24 V and the minimum voltage being 1.7 V [71].

To evaluate the aging evolution, the batteries were removed at different aging points, so 2 with 50 cycles, 2 with 100 cycles, 2 with 150 cycles and 2 with 200 full charge/discharge cycles were taken.

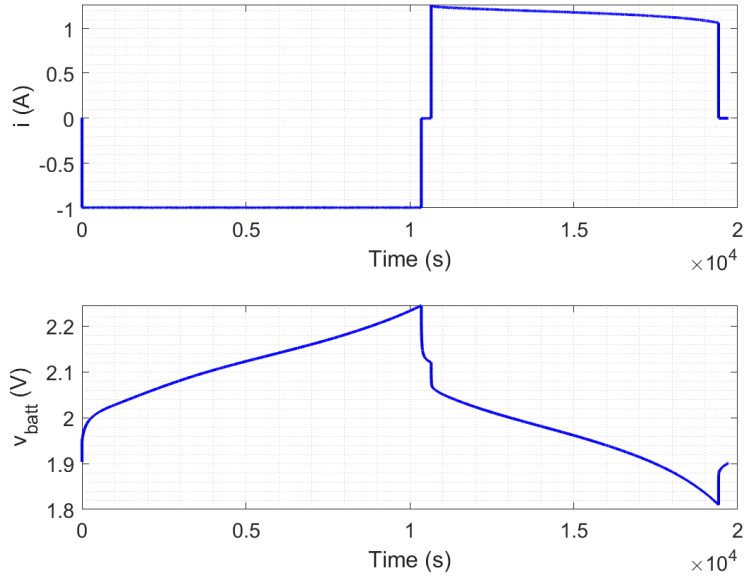

Figure 3.19: Voltage and current profile for charge/discharge aging cycle for lead acid batteries according to IEC60095-1.

The data obtained were separated for each charge and discharge cycle, using this information to apply the previously described RLS algorithm, which was simulated using MATLAB.

3.6.2 Battery parameter estimation

The above-mentioned aging test was applied to eight batteries (B1 to B8) and for each of them the parameters were estimated at the end of each cycle. From the data obtained, the loss of health status was estimated, which is defined as $1 - SOH$, obtaining the graph in Figure 3.20, Observing how the loss of health increases until it reaches close to 0.25 when approaching 200 cycles, this measurement is consistent with the battery data sheet since for charge/discharge cycles of 100% of the SOC, a drop to 70% of the SOH, or what is the same, approximately 30% of health is lost [71].

It is evident that not all batteries have the same behavior; this is because there are slight differences due to manufacturing in the batteries; these changes are known as cell-to-cell variation, which is 5% for lead-acid batteries [74], in addition, during the charging/discharging processes, the brush phenomenon is present, which tends to weaken the battery charge [68]. It is also notable that, every 50 cycles, the values have a more significant variation because, at those times, batteries were removed from the experiment to have batteries at different aging points for later tests. However, this does not mean that the data is invalid since letting the batteries rest longer allows the measurements to vary.

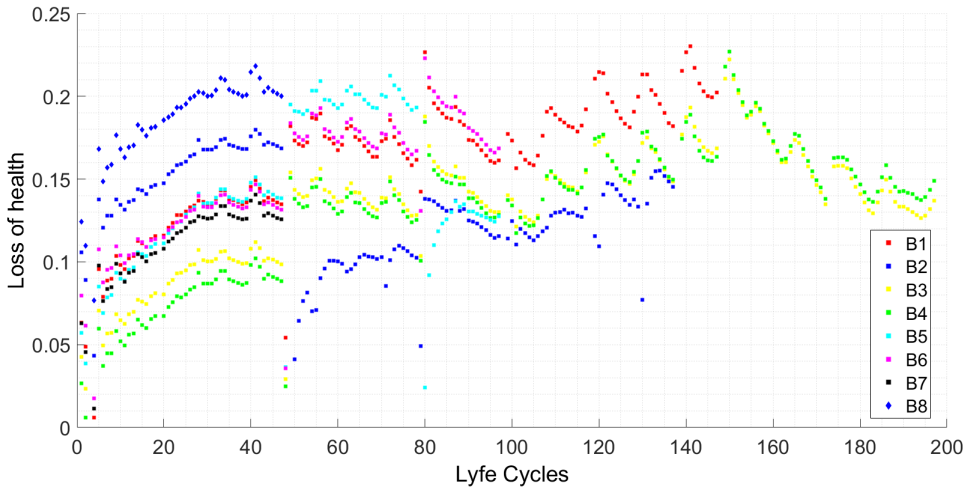

Figure 3.20: Dispersion for the loss of health status in VRLA batteries throughout 200 charge/discharge cycles

With these results, we can assume that the RLS gives results following the expected behavior of a battery for the test submitted. In order to improve the understanding of these data, all points were adjusted to an average function (PROM data) to obtain a standard deviation graph using a probability distribution function (Distribution PROM), shown in Figure 3.21. In this way, it can be seen that the data obtained are close, allowing us to infer that the results obtained are consistent.

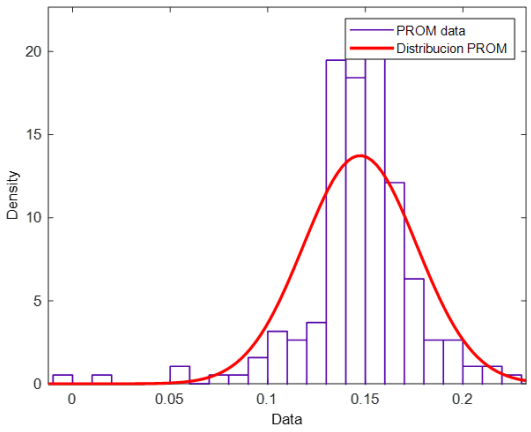

Figure 3.21: Standard deviation graph for probability distribution function of health loss

Similarly, Figure 3.22 shows the changes of the capacitors for the same eight batteries along the cycles, showing a trend corresponding to aging, also Figure 3.23

shows the changes of the resistors, all these cases show the dispersion of data produced, finding in all of them a marked trend, so it is possible to conclude that the parameter changes of the batteries along the useful life can be bounded by the graphs shown in each cycle, so that a parameter that exceeds these limits may be indicative of abnormal behavior.

Figure 3.22 and Figure 3.23 show the raw data of the capacitors and resistors throughout their useful life, showing their variations, and can be observed that the parameter value is different among the eight batteries in similar conditions. However, it is possible to note that the mostly data follow a trend, suggesting that a battery of the same technology in a known number of cycles will have parametric values withing the trend, and if it has a distant value, it can be associated with abnormal aging or misuse.

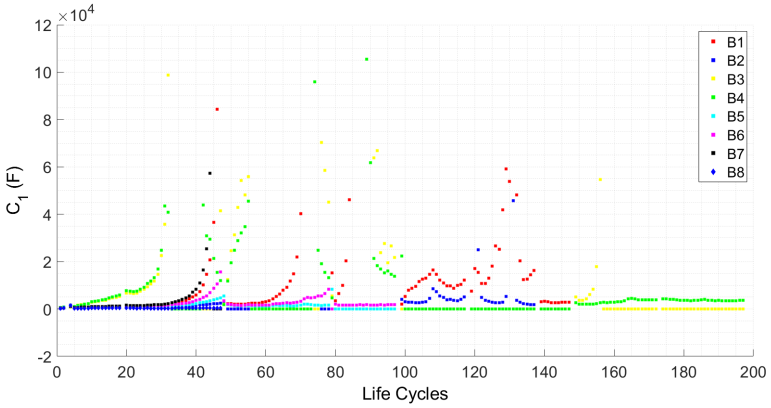

(a)

(b)

Figure 3.22: Capacitors dispersion for VRLA batteries through 200 life cycles. (a) C_1 and (b) C_2.

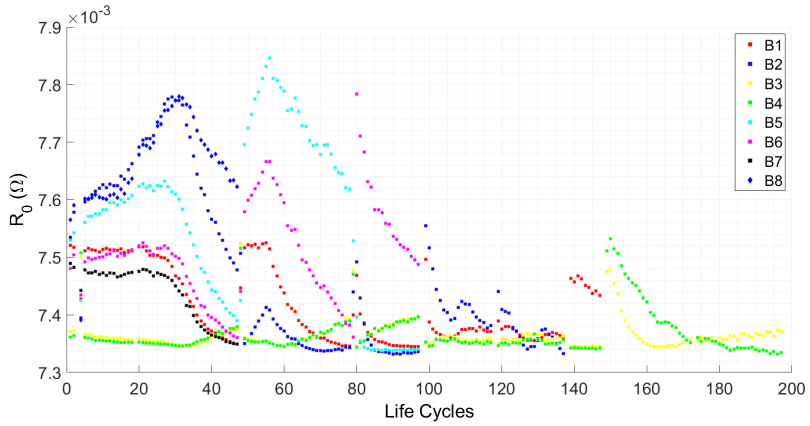

(a)

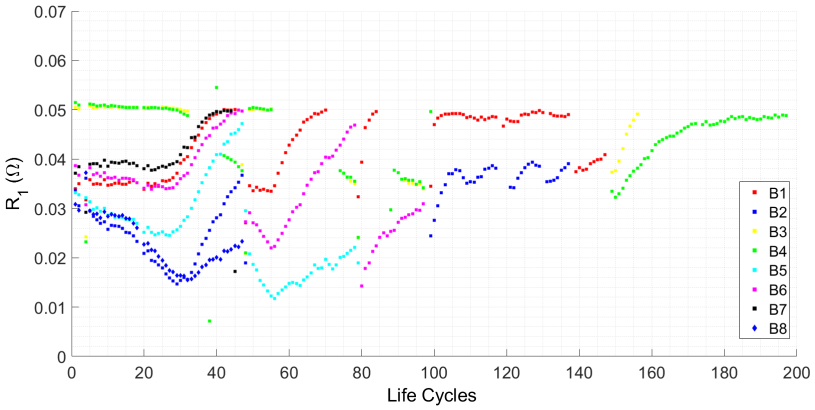

(b)

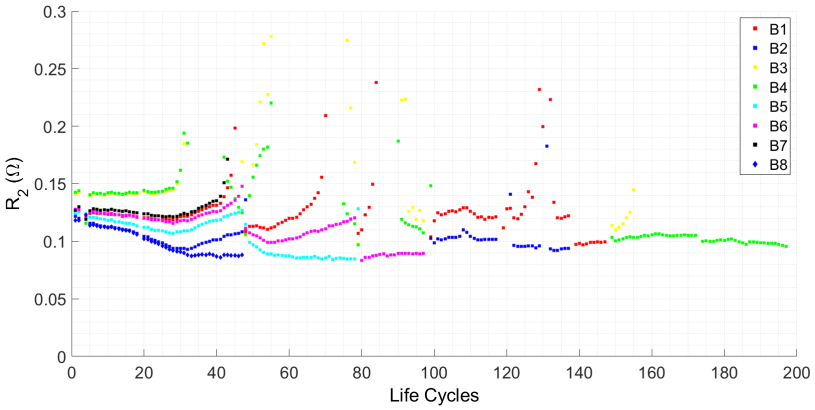

(c)

Figure 3.23: Resistors dispersion for VRLA batteries through 200 life cycles. (a) R_0, (b) R_1, and (c) R_2.

With the results described above, it is assumed that the variations can be estimated for specific purpose, mainly to detect aging mechanisms thorough parametric variations. To test this idea, it is proposed to develop a corrosion-sensitive model, which serves as a case study to validate the parameter variation and associate it with an internal mechanism.

3.7 Modeling Corrosion Layer Formation and Growth in Battery with EEC

To model corrosion it is important to deepen the understanding of this mechanism, understanding that corrosion is a primary factor contributing to battery aging and failure, arising from the inherent chemical processes within the cell, as is documented in [78, 79].

This aging mechanism is a byproduct of chemical reactions within the battery, and is a primary cause of battery degradation. Oxygen exposure and temperature fluctuations at the positive electrode facilitate the formation of a protective PbO_x layer (where $1 \leq x \leq 1.5$), reducing the active surface area and promoting the detachment of lead particles. This corrosion process, visualized in Figure 3.24, ultimately contributes to battery failure, as detailed in [3, 65, 80, 81].

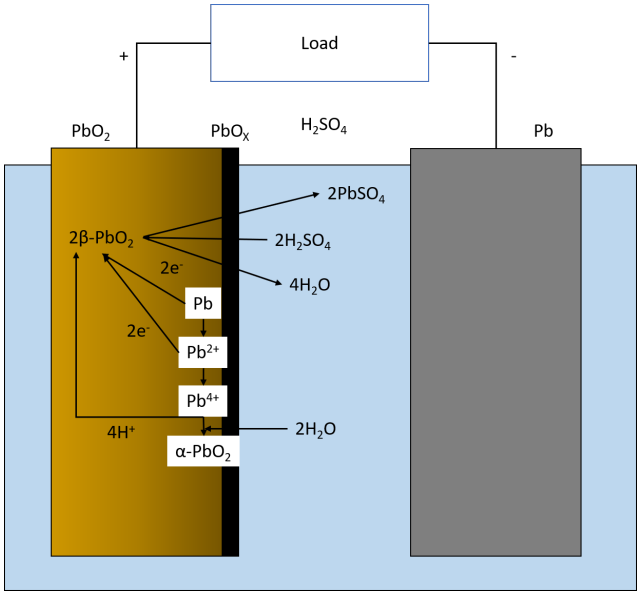

Figure 3.24: Passive film formation due to anodic corrosion [3]

The presence of hydrogen particles within the electrode structure creates voids that facilitate ion movement and, consequently, electron flow. This process accelerates

electrode corrosion due to the availability of free oxygen atoms. These oxygen atoms contribute to the formation of additional voids, further enhancing electron mobility and ultimately leading to accelerated battery degradation, as documented in [3, 79].

Accelerated corrosion can be attributed to various factors, including separator damage as detailed in [82], electrode surface contamination, and porous electrode structures as described in [83].

The rate at which chemical reactions occur within the battery varies over time, as illustrated in Figure 3.14. Importantly, the formation of a corrosion layer influences the behavior of the electrical double layer, as detailed in [1].

3.7.1 Corrosion EEC

In this work is decided to explore the model proposed in [84], That proposes an addition of passive elements in the response of charge transfer in the double layer, considering an electrode-electrolyte interface, adding R_{corr} to the model, as the resistance of the material to be corroded, parallel to it C_{corr} is added, which is inversely proportional to the thickness of the passive film, representing the increase in the speed of ion transmission in the electrolyte due to the particles attached to the electrode, resulting in PbO_x particles.

The proposed EEC model is based on the circuit depicted in Figure 3.1. To incorporate corrosion effects, a corrosion-related resistance and capacitance (R_{corr} and C_{corr}) elements are added in parallel with the first RC component (R_1 and C_1) of the circuit. This arrangement is justified by the relatively short time constant associated with corrosion processes, which primarily occur within the double layer as illustrated in Figure 3.14. The resulting EEC model, incorporating corrosion effects, is presented in Figure 3.25.

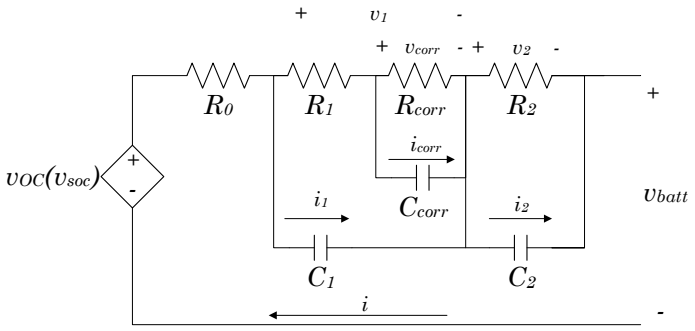

Figure 3.25: Proposed EEC model for electrode-electrolyte interface and corrosion.

A mathematical model was derived for the proposed circuit by applying Lagrangian energy principles. The resulting model equations are based on Kirchhoff's circuit laws.

A voltage relationship, as defined in Equation (3.18), was derived for the model. In this equation, battery voltage (v_{batt}) is the output variable and current (i) is the input.

$$v_{batt} = v_{OC} - iR_0 - v_1 - v_2 \tag{3.18}$$

Additionally, Equation (3.19) presents the relationship between current and voltage across the capacitors. These variables constitute the state variables for the model's state-space representation.

$$\begin{aligned} i_{C_1} &= C_1 \frac{dv_1}{dt} \\ i_{C_{corr}} &= C_{corr} \frac{dV_{corr}}{dt} \\ i_{C_2} &= C_2 \frac{dv_2}{dt} \end{aligned} \tag{3.19}$$

The state-space model, presented in Equation (3.20), was developed using the voltage and current relationships established in Equations (3.18) and (3.19). This model comprehensively represents the circuit behavior, including the impact of corrosion on the battery.

$$\begin{aligned} \begin{bmatrix} \dot{v}_1 \\ \dot{v}_{corr} \\ \dot{v}_2 \end{bmatrix} &= \mathbf{A}_c \begin{bmatrix} v_1 \\ v_{corr} \\ v_2 \end{bmatrix} + \mathbf{B}_c i \\ v_{batt} &= \mathbf{C}_c \begin{bmatrix} v_1 \\ v_{corr} \\ v_2 \end{bmatrix} + \mathbf{D}_c i + v_{OC}(v_{SOC}) \end{aligned} \tag{3.20}$$

Where $\mathbf{A}_c$, $\mathbf{B}_c$, $\mathbf{C}_c$, and $\mathbf{D}_c$ are defined as:

$$\begin{aligned} \mathbf{A}_c &= \begin{bmatrix} -\frac{1}{R_1 C_1} & \frac{1}{R_1 C_1} & 0 \\ \frac{1}{R_1 C_{corr}} & -\frac{R_1 + R_{corr}}{R_1 R_{corr} C_{corr}} & 0 \\ 0 & 0 & -\frac{1}{R_2 C_2} \end{bmatrix}; \\ \mathbf{B}_c &= \begin{bmatrix} \frac{1}{C_1} \\ 0 \\ \frac{1}{C_2} \end{bmatrix}; \mathbf{C}_c = \begin{bmatrix} -1 & 0 & -1 \end{bmatrix}; \mathbf{D}_c = \begin{bmatrix} -R_0 \end{bmatrix}; \end{aligned} \tag{3.21}$$

The system's stability was verified through eigenvalue analysis using the internal stability theorem. All eigenvalues were found to be non-positive, confirming Lyapunov stability. Additionally, the system was determined to be both observable and controllable.

The proposed model exhibits characteristics consistent with those reported in [84]. The inclusion of corrosion effects in the model aligns with findings from studies, such as [85].

3.8 Experimental Setup

To validate the model's ability to accurately simulate terminal voltage dynamics, a comparison was conducted between simulated and experimental data obtained from a charge/discharge profile, as shown in Figure 3.26.

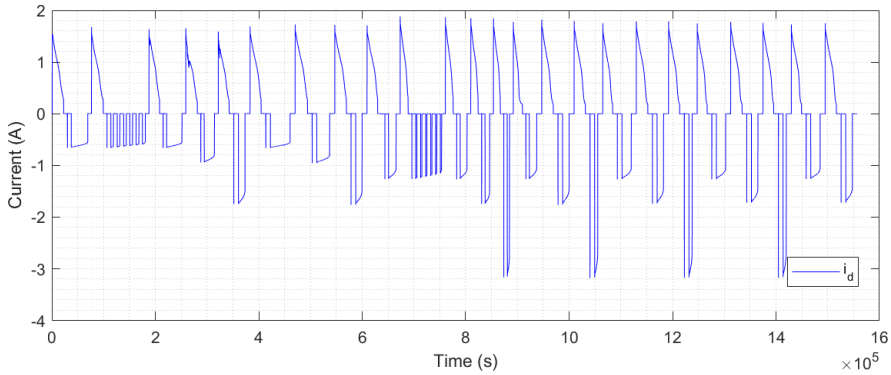

Figure 3.26: Battery charge/discharge current profile.

A three-level discharge profile combined with constant charging was employed for the testing. Data acquisition and processing were handled by an RTAC SEL-2240 industrial computer, configured as illustrated in Figure 3.27. The experiments were conducted within the L-53 electric vehicle laboratory at the Universidad Autónoma de San Luis Potosí.

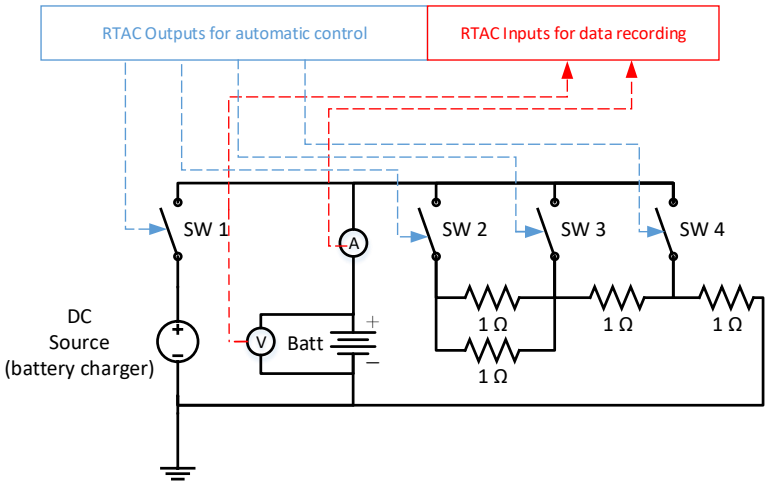

Figure 3.27: Battery testing circuit schematic.

3.8.1 RLS computational model

The transfer function, required for the RLS model, was derived from the state-space model via Equation (3.22). In this equation, $\mathbf{I}$ represents the identity matrix.

$$G(s) = \mathbf{C}_c(s\mathbf{I} - \mathbf{A}_c)^{-1}\mathbf{B}_c + \mathbf{D}_c \tag{3.22}$$

The RLS algorithm, incorporating the forgetting factor as described in [2], was employed to estimate the parameters of the Thévenin equivalent model.

The parameters obtained from the RLS algorithm, specifically R_0, R_2, and C_2, were assumed to be constant for the corrosion-sensitive model, taking a mean value within the average function previously described in the data dispersion, this with the purpose of observing in the rest of the parameters the variations corresponding to corrosion under normal aging conditions. The transfer function of this model takes the voltage across R_1, C_1, R_{corr}, and C_{corr}, represented by $E_{corr}(s)$ in Equation (3.23), as its input.

$$\begin{gathered} E_{corr}(s) = v_{batt} - v_{OC} + v_2 + v_{R_0} \\ E_{corr} = -I(s) - \frac{C_{corr}R_1R_{corr}s + R_1 + R_{corr}}{C_1C_{corr}R_1R_{corr}s^2 + C_1R_1s + C_1R_{corr}s + C_{corr}R_{corr}s + 1} \end{gathered} \tag{3.23}$$

The continuous-time transfer function was converted to its discrete-time equivalent using the bilinear transformation defined in Equation (3.24). In this equation, T_c represents the chosen sampling time.

$$s = \frac{2}{T_c}\frac{1 - z^{-1}}{1 + z^{-1}} \tag{3.24}$$

The resulting discrete-time transfer function is given by Equation (3.25).

$$G(z) = \frac{E_{corr}(k)}{I(k)} = \frac{\theta_{corr3} + \theta_{corr4}z^{-1} + \theta_{corr5}z^{-2}}{1 - \theta_{corr1}z^{-1} - \theta_{corr2}z^{-2}} \tag{3.25}$$

For easier notation, it was substitute variables $a_{corr}, b_{corr}, c_{corr}, d_{corr}$ into the transfer function, as shown in Equation (3.26).

$$\begin{cases} a_{corr} = C_1 \\ b_{corr} = R_1R_{corr}C_{corr} \\ c_{corr} = R_1 + R_{corr} \\ d_{corr} = R_1C_1 + C_1R_{corr} + C_{corr}R_{corr} \end{cases} \tag{3.26}$$

Assuming the new variable substitutions, the RLS algorithm outlined in [2] is reapplied. However, two key adjustments are made:

- The input-output data pairs used in the RLS algorithm are now defined by Equation (3.23), which incorporates the voltage term specific to the corrosion-sensitive model.

- The coefficients of the new parameter vector, denoted by $\boldsymbol{\theta}_{corr}$, are expressed using auxiliary variables as shown in Equation (3.27).

This simplifies the estimation process.

$$\begin{cases} a_{corr} = \dfrac{1}{4}\dfrac{T_c(\theta_{corr1} - \theta_{corr2} - 1)}{2\theta_{corr3} - \theta_{corr4}} \\ b_{corr} = -\dfrac{T_c(2\theta_{corr3} - \theta_{corr4})}{\theta_{corr1} - \theta_{corr2} - 1} \\ c_{corr} = -\dfrac{2\theta_{corr4})}{\theta_{corr1} - \theta_{corr2} - 1} \\ d_{corr} = -\dfrac{T_c(\theta_{corr2} - 1)}{\theta_{corr1} - \theta_{corr2} - 1} \end{cases} \tag{3.27}$$

Equation (3.28) provides the unknown parameter values based on the newly defined system.

$$\begin{cases} C_1 = a_{corr} \\ R_1 = -\dfrac{b_{corr}}{a_{corr}c_{corr} - d_{corr}} \\ R_{corr} = \dfrac{a_{corr}c_{corr}^2 - c_{corr}d_{corr} + b_{corr}}{a_{corr}c_{corr} - d_{corr}} \\ C_{corr} = \dfrac{(a_{corr}c_{corr} - d_{corr})^2}{a_{corr}c_{corr}^2 - c_{corr}d_{corr} + b_{corr}} \end{cases} \tag{3.28}$$

The collected measurement data is processed using the adaptive forgetting factor RLS algorithm, as outlined in the flowchart of Figure 3.28. This process enables the estimation of model parameters.

Table 3.4 presents the initial RLS algorithm parameters. The values of λ and λ_{min} are the values of the forgetting factor and the minimum forgetting factor, respectively; both values must range between 0.95 - 1, where λ_{min} is the smallest value that this factor can have to allow adjustment, so an intermediate value to those mentioned above was taken. The λ value was initialized at this same value to prevent the RLS from starting with a high variation. h is the sensitivity value, which can take a value between 0 and 1; the closer to 1, the forgetting factor changes slowly; on the other hand, the closer to 0, the forgetting factor changes quickly, so a value of 0.99 was selected. To allow the RLS to adjust smoothly. $e_{base_{corr}}$ is the allowed error, which is selected low enough to adjust the RLS to the evaluated measurements; $E_{corr}(-1)$ and $E_{corr}(-2)$ are the previous voltage measurements, which is recommended to initialize at 0. Finally, $\boldsymbol{\theta}_{corr}(0)$ is initialized at zero so as not to alter the adjustment trend, which is recommended to vary if, after initializing it at zero, the RLS does not converge.

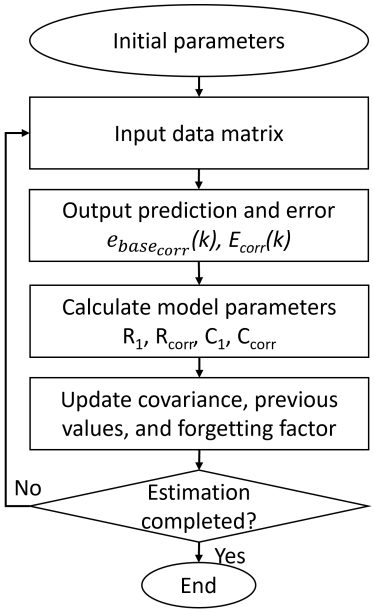

Figure 3.28: Flowchart of adaptive forgetting factor RLS for corrosion detection.

Table 3.4: RLS initial conditions for corrosion model estimation on PS-260 Battery.

Parameter	Value
λ	0.98
λ_{min}	0.98
h	0.99
$e_{base_{corr}}$	0.005
$E_{corr}(-1)$	0
$E_{corr}(-2)$	0
$\boldsymbol{\theta}_{corr}(0)$	$[0, 0, 0, 0, 0]$

3.8.2 Model Performance Validation

To estimate the unknown corrosion-related parameters, R_{corr} and C_{corr}, within the proposed model, the RLS algorithm outlined in Figure 3.28 was employed. An optimally functioning battery was initially used to establish baseline parameter values, assuming R_{corr} to be zero and C_{corr} to be infinitely large. Given the unavailability of true resistor and capacitor values for validation, the estimated parameters were incorporated into

the EEC model. The model's voltage output was then compared to measured voltage data to assess its accuracy.

The evolution of the resistor R_{corr}, as determined by the RLS algorithm, is depicted in Figure 3.29 using a red line.

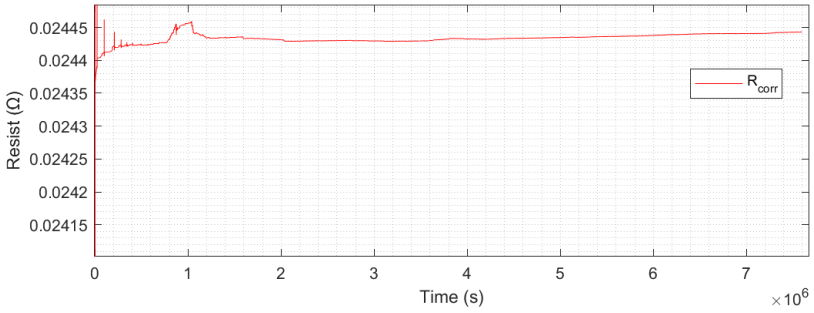

Figure 3.29: Evolution of corrosion resistance during RLS estimation.

The RLS-estimated values for the corrosion-related capacitor, C_{corr}, are plotted in black in Figure 3.30.

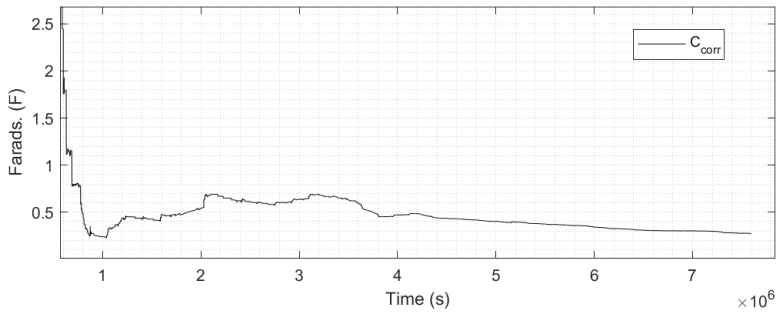

Figure 3.30: Evolution of corrosion capacitance during RLS estimation.

The observed trends in C_{corr} and R_{corr} align with established knowledge. As the passivation layer thickens, capacitance (C_{corr}) typically decreases, while resistance to ion flow (R_{corr}) increases, as reported in the literature.

Table 3.5 presents the constant parameter values obtained for the EEC model.

Table 3.5: Passive component values for corrosion-sensitive EEC model using RLS algorithm.

Parameter	Value
R_0	$7.4334 \times 10^{-03}\Omega$
R_1	$3.3287 \times 10^{-02}\Omega$
R_2	$1.6995 \times 10^{-02}\Omega$
R_{corr}	$5.3508 \times 10^{-02}\Omega$
C_1	$6.2032 \times 10^{02}F$
C_2	$3.1021 \times 10^{03}F$
C_{corr}	$7.1249F$

Figure 3.31 presents a comparison of model-predicted and measured voltages. The green curve represents the model output under optimal conditions, while the red curve shows the model's response when incorporating the estimated corrosion parameters, equation (3.20). The blue curve represents the experimental data. While all three curves exhibit similar trends, the model with the added corrosion elements demonstrates a closer approximation to the measured voltage amplitude.

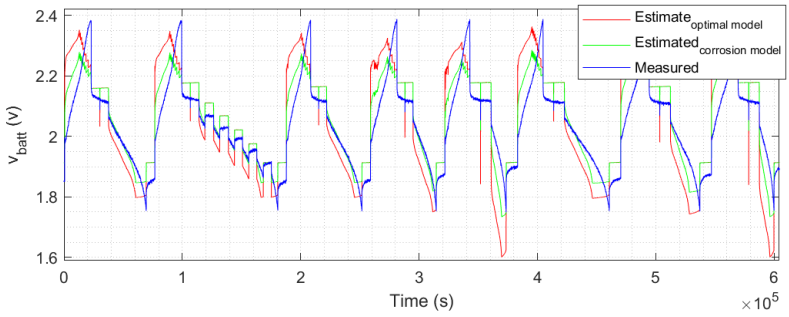

Figure 3.31: Evaluation of corrosion-sensitive model and optimal condition EEC models, compared with measurements.

Figure 3.32 illustrates the voltage error between the measured and modeled data, with the corrosion-sensitive model error plotted in red. For comparison, the error between the optimal condition model and measurements is shown in green. The optimal model exhibits a maximum error of ±12% during switching periods and ±4% otherwise, equating to an approximated deviation of 80 mV. This error level is comparable to other published battery voltage models (e.g., [2, 86]). While the optimal model initially

appears more accurate, the corrosion-sensitive model more realistically captures the gradual degraded capacity observed in the negative voltage region.

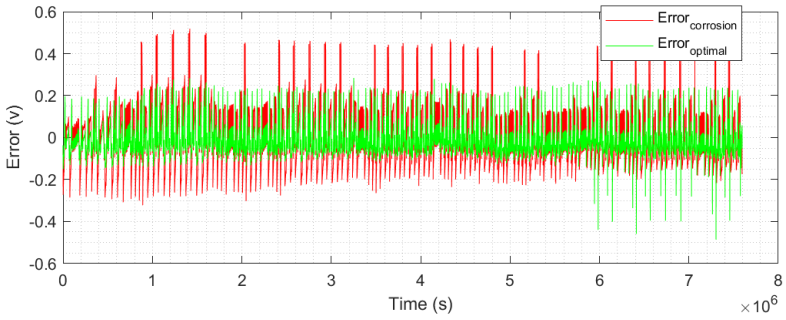

Figure 3.32: Error between v_{batt} voltage measurements, RLS estimation for the corrosion model and optimal condition model.

From the results shown above it is known that the battery naturally begins to corrode, this can be observed in the estimation of the values of R_{corr} and C_{corr}, which change as corrosion occurs progressively, however, the experiments carried out are based solely on the published information regarding the dynamic behavior of the battery against the effects of corrosion and there is no way to contrast corrosion. Following this methodology it is difficult to know the meaning of the changes or to have the ability to distinguish between the appearance of one or another fault, since they occur simultaneously. This is why it was decided to analyze the parameters of the EEC model from a different point of view, seeking to correlate the parameters with internal reactions of the battery, thus avoiding speculations due to lack of information.

As background material, the battery data sheet used is attached bellow.

Rechargeable Sealed Lead-Acid Battery

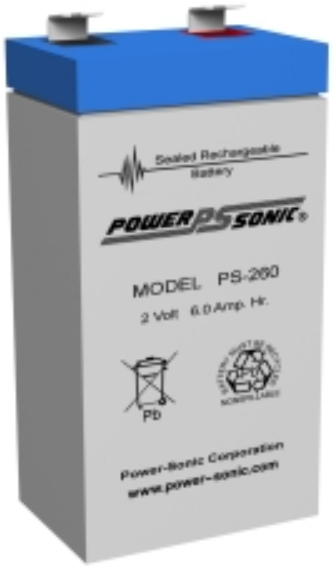

PS-260

2 Volt 6.0 Amp. Hrs.

Features:

- Absorbent Glass Mat (AGM) technology for superior performance.
- Valve regulated, spill proof construction allows safe operation in any position.
- Power/volume ratio yielding unrivaled energy density.
- Rugged ABS plastic case and cover
- Approved for transport by air. D.O.T., I.A.T.A., F.A.A. and C.A.B. certified.
- U.L. recognized under file number MH 20845.

PERFORMANCE SPECIFICATIONS

Nominal Voltage ..... 2 volts (1 cell)

Nominal Capacity

20 hour rate (300mA to 1.75 volts) ..... 6.0 A.H.

10 hour rate (540mA to 1.75 volts) ..... 5.4 A.H.

5 hour rate (980mA to 1.70 volts) ..... 4.9 A.H.

1 hour rate (3600mA to 1.50 volts) ..... 3.6 A.H.

Approximate Weight ..... 0.86 pounds (0.39 kg)

Energy Density (20 hour rate) ..... 1.15 Watt-hours/cubic inch (70.6 Watt-hours/l)

Specific Energy (20 hour rate) ..... 14.0 Watt-hours/pound (30.8 Watt-hours/kg)

Internal Resistance (Fully Charged Battery) ..... 5 milliohms (approximately)

Maximum Discharge Current (≤ 7 Min.) ..... 7.8 amperes

Maximum Short-Duration Discharge Current (≤ 10 Sec.) ..... 26.0 amperes

Terminals ..... "F1": Quick Disconnect tabs, 0.187" x 0.032" - Mate with AMP, INC. FASTON "187" series

Shelf Life — % of nominal capacity at 68° F (20° C)

1 Month 97%

3 Months 91%

6 Months 83%

Operating Temperature Range

Charge ..... -4°F (-20°C) to 122°F (50°C)

Discharge ..... -4°F (-20°C) to 140°F (60°C)

Case ..... ABS Plastic

Shelf Life and Storage

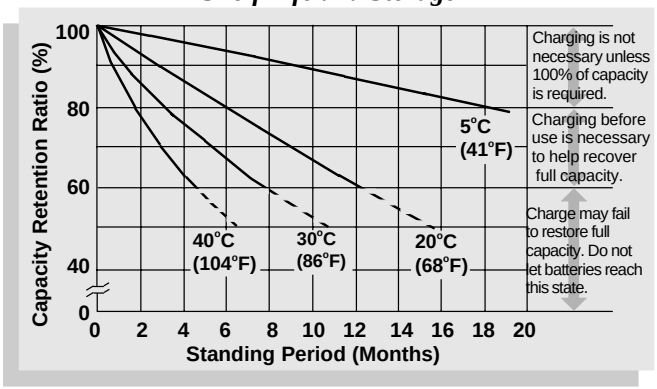

Discharge Characteristics

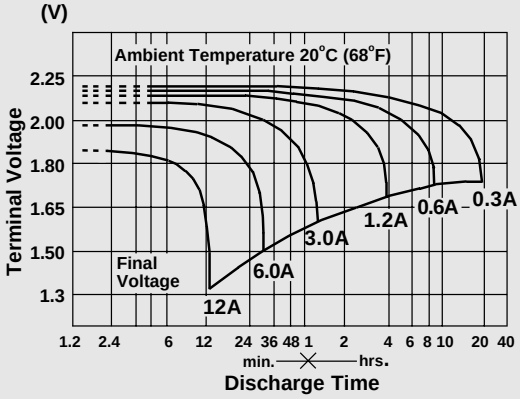

Life Characteristics in Stand-By Use

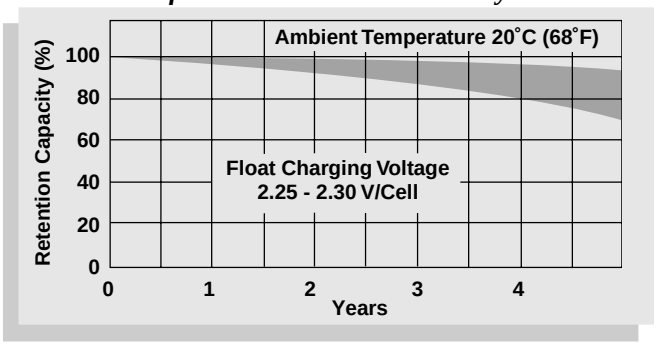

Discharge Time vs. Discharge Current

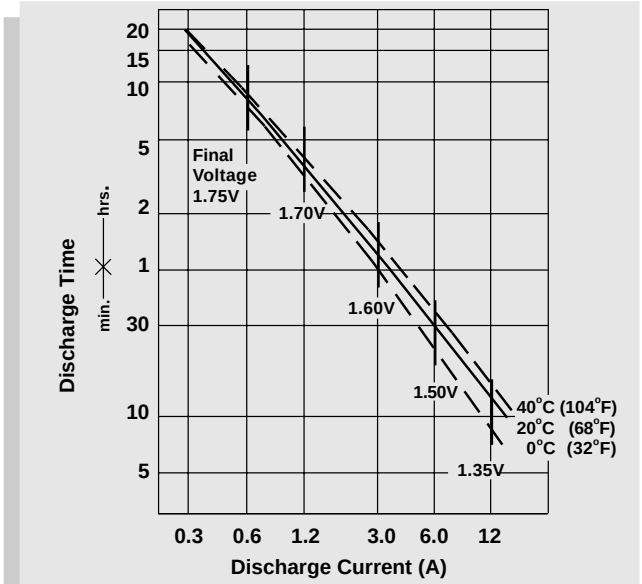

Life Characteristics in Cyclic Use

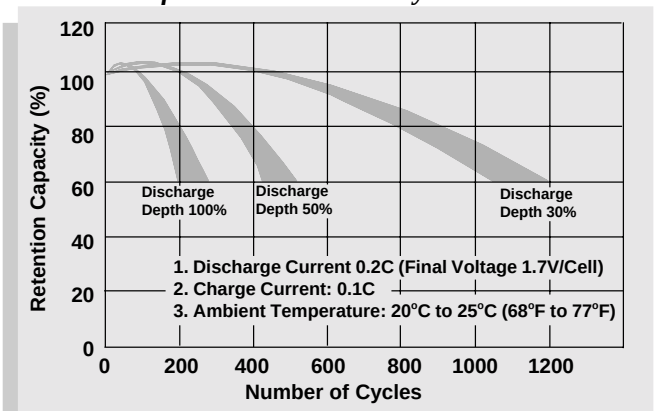

Physical Dimensions: in. (mm)

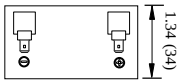

Terminals: F1 (mm)

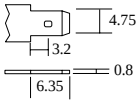

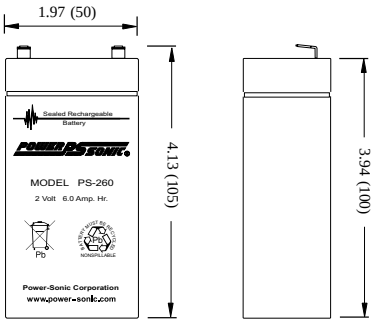

Tolerances are +/- 0.04 in. (+/- 1mm) and +/- 0.08 in. (+/- 2mm) for height dimensions.
All data subject to change without notice.

CHARGING

Cycle Applications: Limit initial current to 1.8A. Charge until battery voltage (under charge) reaches 2.4 to 2.5 volts at 68°F (20°C). Hold at 2.4 to 2.5 volts until current drops to approximately 60mA. Battery is fully charged under these conditions, and charger should either be disconnected or switched to "float" voltage.

"Float" or "Stand-By" Service: Hold battery across constant voltage source of 2.25 to 2.30 volts continuously. When held at this voltage, the battery will seek its own current level and maintain itself in a fully charged condition.

NOTE: Due to the self-discharge characteristics of this type of battery, it is imperative that they be charged after 6-9 months of storage, otherwise permanent loss of capacity might occur as a result of sulfation.

POWER-SONIC

SALES & MARKETING
3106 Spring Street
Redwood City, CA 94063 USA
Tel: 650-364-5001 Fax: 650-366-3662
national-sales@power-sonic.com

ISO9001-2000
FM39170

www.power-sonic.com

CUSTOMER SERVICE
7550 Panasonic Way
San Diego, CA 92154 USA
Tel: 619-661-2030 Fax: 619-661-3648
customer-service@power-sonic.com

PRINTED IN U.S.A.

11/04 1.5M

Chapter 4

Equivalent Electric Circuit modeling based on mechanistic model

In this chapter, a mechanistic model was developed to elucidate the internal mechanisms of a lead-acid battery. Subsequently, the resulting impedance data was utilized to propose a 3-RC parallel arrangement EEC model. By employing EIS, a correlation between the contributions of the poles of both models was established. This correlation was further validated through comprehensive analysis across the SOC and throughout the useful life.

4.1 Lead-acid mechanistic model

As already mentioned, knowing the physical meaning of the parameters of the model becomes relevant to associate the variations of these parameters to the internal electrochemical phenomena caused by the aging, so this issue is approached from a different point of view than previously published, where the parameters of the EEC model are redefined and correlated with a mechanistic model through the analysis of EIS and the control theory. For this purpose, the mechanistic model used in this work is developed below.

A mechanistic model is a system model based on electrochemical kinematic equations that represents the rate at which chemical reactions occur [87].

The procedure for deriving the mechanistic model can be outlined in six steps as follows:

1. Consider an electrochemical battery system involving adsorbed intermediates.
2. Apply mass balance to derive the reaction transfer function.
3. Apply charge balance to derive faradic impedance.

4. Construct the equivalent circuit (Figure 4.1) by incorporating the interfacial capacitance (C_{dl}) and solution resistance (R_s).

5. Incorporate electrode area in transfer function calculations.

6. Determine time constants of each reaction from battery model.

The previous steps are shown in Figure 4.1 and will be detailed in the following sections.

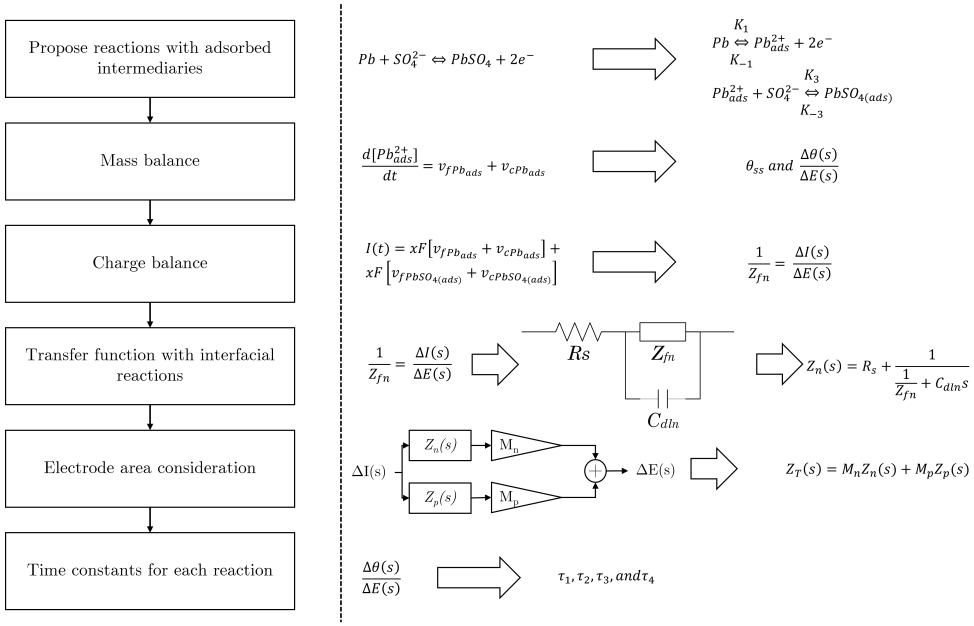

Figure 4.1: Flowchart for battery mechanistic model and impedance analysis

A fundamental understanding of faradic reactions is essential. As outlined in [66, 67], these reactions involve a material (A_{sol}) undergoing a transformation into a new substance (C_{sol}) through the gain or loss of energy (electrons, e^-).

$$A_{sol} + xe^- \Leftrightarrow C_{sol} \tag{4.1}$$

where The variable x represents the number of electrons participating in the reaction. By incorporating adsorbed intermediates, represented as a function of surface coverage for species B_{ads}, the reaction equation can be reformulated as a faradic loop in equation (4.2). This approach offers insights into the dynamic behavior of each individual process contributing to the overall reaction, as detailed in [88].

$$\begin{aligned} A_{sol} + r_1 e^- &\underset{K_{-a}}{\overset{K_a}{\Longleftrightarrow}} B_{ads} \\ B_{ads} + r_2 e^- &\underset{K_{-b}}{\overset{K_b}{\Longleftrightarrow}} C_{sol} \end{aligned} \tag{4.2}$$

The total number of electrons involved in the faradic loop (r_1+r_2) equals the number of electrons transferred in the overall reaction (x). The reaction rate constants, K_a, K_{-a}, K_b and K_{-b}, quantify the rates of formation and depletion for each adsorbed species.

4.1.1 Propose reactions with adsorbed intermediaries

Building upon the aforementioned principles, a lead-acid battery, composed of a lead negative electrode (Pb), lead dioxide positive electrode (PbO_2), and sulfuric acid electrolyte(H_2SO_4), as described in [71], can be represented through faradic loop models, as outlined in [89].

For lead-acid batteries, two simultaneous reactions occur at each electrode. On the negative electrode, these reactions are represented by equations (4.3) and (4.4). equation (4.3) describes the process where lead from the electrode detaches and forms adsorbed lead ions (Pb^{2+}_{ads}), releasing two electrons in the process. Equation (4.4) depicts the consumption of these Pb^{2+}_{ads} ions by reacting with sulfate ions in the electrolyte, resulting in the formation of lead sulfate ($PbSO_{4(ads)}$) on the electrode surface, as explained in [90].

$$Pb \underset{K_{-1}}{\overset{K_1}{\rightleftharpoons}} Pb^{2+}_{ads} + 2e^- \tag{4.3}$$

$$Pb^{2+}_{ads} + SO^{2-}_4 \underset{K_{-3}}{\overset{K_3}{\rightleftharpoons}} PbSO_{4(ads)} \tag{4.4}$$

The chemical reactions occurring at the positive electrode are detailed in Equations (4.5) and (4.6). In Equation (4.5), lead dioxide decomposes into adsorbed lead ions (Pb^{2+}_{ads}) and water molecules through a two-electron reduction process. Subsequently, Equation (4.6) describes the reaction between these adsorbed lead ions and sulfate ions from the electrolyte, resulting in the formation of lead sulfate ($PbSO_{4(ads)}$) on the electrode surface, as reported in [91].

$$PbO_2 + 4H^+ + 2e^- \underset{K_{-2}}{\overset{K_2}{\rightleftharpoons}} Pb^{2+}_{ads} + 2H_2O \tag{4.5}$$

$$Pb^{2+}_{ads} + SO^{2-}_4 \underset{K_{-4}}{\overset{K_4}{\rightleftharpoons}} PbSO_{4(ads)} \tag{4.6}$$

The previously described reactions are influenced by the time-varying potential difference, $E(t)$. This dependence is reflected in the reaction rate constants (K_i, where $i = 1, -1, 2, -1, 3, -3, 4, -4$), which are defined by the Tafel equation (Equation (4.7)) involving Tafel coefficients (b_i) and pre-exponential factors (k_i) as mentioned in [92]. Consequently, the resulting evolution equation exhibits nonlinear behavior due to the exponential relationship with $E(t)$.

$$K_i = k_i e^{b_i E(t)} \tag{4.7}$$

The Tafel coefficient is defined as:

$$b_i = \frac{n\alpha F}{RT} \tag{4.8}$$

where n represents the number of electrons transferred in the reaction, α is the charge transfer coefficient ($0 < \alpha < 1$), F is the Faraday constant (96500 C mol^{-1}), R is the ideal gas constant (8.314 J mol^{-1} K^{-1}), and T is the absolute temperature in Kelvin. Due to the temperature dependency embedded in the Tafel coefficient, changes in temperature would influence the model's behavior [92]. However, the present study was confined to room temperature conditions (approximately 303 K).

It is important to note that two distinct adsorbed intermediates, Pb^{2+}_{ads} and $PbSO_{4(ads)}$, are formed during the electrode reactions. Interestingly, the formation of $PbSO_{4(ads)}$ occurs at both the positive and negative electrodes. In the following sections, the mechanistic model is developed for the reactions of the negative electrode, since for the positive electrode the equations will only modify the subscripts 1 by 2 and 3 by 4.

4.1.2 Mass balance

The concentrations of the adsorbed species, $[Pb^{2+}_{ads}]$ and $[PbSO_{4(ads)}]$, are expressed in terms of surface area units, as defined by equations (4.9) and (4.10) [88].

$$[Pb^{2+}_{ads}] = \beta_1\theta_1(t) \tag{4.9}$$

$$[PbSO_{4(ads)}] = \beta_3\theta_3(t) \tag{4.10}$$

where the parameters β_1 and β_3 represent the maximum adsorbate concentrations (lead and sulfate, respectively) per unit surface area. The variables $\theta_1(t)$ and $\theta_3(t)$ represent the fractions of the surface occupied by lead and sulfate adsorbates at a given time (t).

To ensure compliance with the law of conservation of matter, a mass balance equation is required. Equation (4.11) specifically focuses on the adsorbed species $[Pb^{2+}_{ads}]$ and expresses their balance, considering both formation and consumption rates, as described in [93].

$$\frac{d[Pb^{2+}_{ads}]}{dt} = v_{fPb^{2+}_{ads}} - v_{cPb^{2+}_{ads}} \tag{4.11}$$

where in the mass balance equation, $v_{fPb^{2+}_{ads}}$ represents the rate of formation of adsorbed lead, while $v_{cPb^{2+}_{ads}}$ denotes its consumption rate. A similar mass balance equation for the adsorbed lead sulfate species, $[PbSO_{4(ads)}]$, is presented in Equation (4.12).

$$\frac{d[PbSO_{4(ads)}]}{dt} = v_{fPbSO_{4(ads)}} - v_{cPbSO_{4(ads)}} \tag{4.12}$$

where $v_{fPbSO_{4(ads)}}$ represents the rate of formation of adsorbed sulfate, and $v_{cPbSO_{4(ads)}}$ denotes its consumption rate.

The formation and consumption rates of adsorbed species, as expressed in the mass balance equation (4.11), are determined by the changes in surface coverage over time. This relationship is further detailed in Equation (4.13), as explained in [88].

$$\begin{aligned} v_{fPb^{2+}_{ads}} &= K_1(1-\theta_1(t)-\theta_3(t)) + K_{-3}[PbSO_{4(ads)}] \\ v_{cPb^{2+}_{ads}} &= K_{-1}[Pb^{2+}_{ads}] + K_3[Pb^{2+}_{ads}] \end{aligned} \tag{4.13}$$

Similarly, the formation and consumption rates for the adsorbed lead sulfate species ($PbSO_{4(ads)}$) are defined by Equation (4.12). It's important to note that this particular adsorbate is exclusively formed from the adsorbed lead ions (Pb^{2+}_{ads}) [88].

$$\begin{aligned} v_{fPbSO_{4(ads)}} &= K_3[Pb^{2+}_{ads}] \\ v_{cPbSO_{4(ads)}} &= K_{-3}[PbSO_{4(ads)}] \end{aligned} \tag{4.14}$$

In the case of the positive electrode, equation (4.14) is modified as shown in equation (4.15), and from here on the only difference apart from the subscripts is that the multiplication of the acid concentration ($[SO_4^{2-}]$) will be transferred.

$$\begin{aligned} v_{fPbSO_{4(ads)}} &= K_4[Pb^{2+}_{ads}] \\ v_{cPbSO_{4(ads)}} &= K_{-4}[PbSO_{4(ads)}][SO_4^{2-}] \end{aligned} \tag{4.15}$$

Building upon the previously defined reactions in equations (4.9), (4.10), (4.13), and (4.14), could be substitute these expressions into the mass balance equations ((4.11) and (4.12)). This substitution leads to the evolution equations for the adsorbed species, presented in equations (4.16) and (4.17). Notably, both these evolution equations depend on the time-varying surface coverages, represented by $\theta_1(t)$ and $\theta_3(t)$ and time-varying potential $E(t)$ [88].

$$\beta_1 \frac{d\theta_1(t)}{dt} = K_1(1-\theta_1(t)-\theta_3(t)) + K_{-3}\beta_3\theta_3(t) - \beta_1\theta_1(t)(K_{-1}+K_3) \tag{4.16}$$

$$\beta_3 \frac{d\theta_3(t)}{dt} = K_3\beta_1\theta_1(t) - K_{-3}\beta_3\theta_3(t) \tag{4.17}$$

The resulting system of differential equations is nonlinear, due to the presence of the parameters K_i, so it is necessary to linearize in the steady state of the reaction [88].

4.1.2.1 Evolution equation linearization

The steady-state condition for the evolution equations (4.16) and (4.17) implies no mass exchange, resulting in zero time derivatives for surface fractions ($d\theta_1(t)/dt = 0$, $d\theta_3(t)/dt = 0$) and zero steady-state potential ($E_{ss} = 0$). By setting these conditions, we obtain the simultaneous equations in (4.18). The subscript 'ss' denotes steady-state

values for the time-dependent functions, allowing us to determine steady-state surface fractions θ_{1ss} and θ_{3ss}; and steady-state reaction rate constants ($K_{iss} = k_i$) [88].

$$\begin{aligned} \theta_{1ss} &= \frac{k_1(1-\theta_{3ss}) + k_{-3}\beta_3\theta_{3ss}}{k_1 + \beta_1(k_{-1}+k_3)} \\ \theta_{3ss} &= \frac{k_3\beta_1\theta_{1ss}}{k_{-3}\beta_3} \end{aligned} \tag{4.18}$$

The steady-state values for surface fractions, θ_{1ss} and θ_{3ss}, are determined. Subsequently, a Taylor series expansion is applied to linearize the evolution equations ((4.16) and (4.17)) around the steady-state point. This linearization process results in the simplified equations (4.19) and (4.20). [88]

$$\begin{aligned} \beta_1\frac{d\Delta\theta_1(t)}{dt} =& (-k_1 - \beta_1(k_{-1}+k_3))\Delta\theta_1(t) - (k_1 - k_{-3}\beta_3)\Delta\theta_3(t) + ... \\ &... + (k_1b_1(1-\theta_{1ss}-\theta_{3ss}) - k_{-3}b_{-3}\beta_3\theta_{3ss} + \beta_1\theta_{1ss}(k_{-1}b_{-1} - k_3b_3))\Delta E(t) \end{aligned} \tag{4.19}$$

$$\beta_3\frac{d\Delta\theta_3(t)}{dt} = k_3\beta_1\Delta\theta_1(t) - k_{-3}\beta_3\Delta\theta_3(t) + (k_3b_3\beta_1\theta_{1ss} + k_{-3}b_{-3}\beta_3\theta_{3ss})\Delta E(t) \tag{4.20}$$

The Laplace transform is applied to the linearized system of equations (4.19) and (4.20), resulting in the transformed equations (4.21) and (4.22) [88].

$$\begin{aligned} \beta_1 s\Delta\theta_1(s) =& (-k_1 - \beta_1(k_{-1}+k_3))\Delta\theta_1(s) - (k_1 - k_{-3}\beta_3)\Delta\theta_3(s) + ... \\ &... + (k_1b_1(1-\theta_{1ss}-\theta_{3ss}) - k_{-3}b_{-3}\beta_3\theta_{3ss} + \beta_1\theta_{1ss}(k_{-1}b_{-1} - k_3b_3))\Delta E(s) \end{aligned} \tag{4.21}$$

$$\begin{aligned} \beta_3 s\Delta\theta_3(s) =& (k_3\beta_1\Delta\theta_1(s) - k_{-3}\beta_3\Delta\theta_3(s) + ... \\ &... + (k_3b_3\beta_1\theta_{1ss} + k_{-3}b_{-3}\beta_3\theta_{3ss})\Delta E(s) \end{aligned} \tag{4.22}$$

By algebraic manipulation of equations (4.21) and (4.22), the transfer functions relating the change in surface coverage $\Delta\theta_1(s)/\Delta E(s)$ and $\Delta\theta_3(s)/\Delta E(s)$ are obtained in equations (4.23) and (4.24). These transfer functions quantify the sensitivity of surface coverage to potential variations, as described in [88].

$$\frac{\Delta\theta_1(s)}{\Delta E(s)} = \frac{-(k_1-k_{-3}\beta_3)\frac{\Delta\theta_3(s)}{\Delta E(s)} + (k_1b_1(1-\theta_{1ss}-\theta_{3ss}) - k_{-3}b_{-3}\beta_3\theta_{3ss} + \beta_1\theta_{1ss}(k_{-1}b_{-1}-k_3b_3))}{\beta_1 s + (k_1+\beta_1(k_{-1}+k_3))} \tag{4.23}$$

$$\frac{\Delta\theta_3(s)}{\Delta E(s)} = \frac{k_3\beta_1\frac{\Delta\theta_1(s)}{\Delta E(s)} + k_3b_3\beta_1\theta_{1ss} + k_{-3}b_{-3}\beta_3\theta_{3ss}}{\beta_3 s + k_{-3}\beta_3} \tag{4.24}$$

The obtained transfer functions contain time constants, represented by τ_{1g} from equation (4.23) and τ_{3g} from equation (4.24), as defined in equations (4.25) and (4.26), respectively. These time constants provide an estimate of the system's settling time, or the time required to reach equilibrium after a disturbance, as explained in [94].

$$\tau_{1g} = \frac{\beta_1}{k_1 + \beta_1(k_{-1}+k_3)} \tag{4.25}$$

$$\tau_{3g} = \frac{1}{k_{-3}} \tag{4.26}$$

The transfer functions in equations (4.23) and (4.24) are interdependent, analogous to the coupled equations in (4.18). By solving this system of equations, the steady-state surface coverages (θ_{1ss} and θ_{3ss}) and the transfer function ($\Delta\theta_1(s)/\Delta E(s)$ and $\Delta\theta_3(s)/\Delta E(s)$) can be expressed in terms of measurable parameters [88].

4.1.3 Charge balance

Following the determination of the aforementioned parameters, it is crucial to establish an energy balance, adhering to the principle of energy conservation, as outlined in [95]. This energy balance is mathematically expressed in equation (4.27).

$$I(t) = xF[v_{fPb^{2+}_{ads}} - v_{cPb^{2+}_{ads}}] + xF[v_{fPbSO_{4(ads)}} - v_{cPbSO_{4(ads)}}] \tag{4.27}$$

where F represents Faraday's constant, x is the number of electrons transferred in the reaction, and I is the battery current. By incorporating the mass balance equations ((4.13) and (4.14)) and simplifying, equation (4.28) is obtained.

$$I(t) = xF[K_1(1 - \theta_1(t) - \theta_3(t)) - \beta_1\theta_1(t)K_{-1}] \tag{4.28}$$

It is important to note that the current is influenced by the constants K_1 and K_{-1}, which exhibit nonlinear behavior as defined by Equation (4.7). To simplify Equation (4.28), a linear approximation is obtained through Taylor series expansion.

$$\begin{aligned}\Delta I(t) =& xF(-k_1 - \beta_1 k_{-1})\Delta\theta_1(t) - xFk_1\Delta\theta_3(t) + ... \\ &... + xF(k_1b_1(1 - \theta_{1ss} - \theta_{3ss}) - \beta_1\theta_{1ss}k_{-1}b_{-1})\Delta E(t)\end{aligned} \tag{4.29}$$

Then, the transfer function for $\Delta I(s)/\Delta E(s)$ results in (4.30).

$$\begin{aligned}\frac{\Delta I(s)}{\Delta E(s)} =& xF(-k_1 - \beta_1 k_{-1})\frac{\Delta\theta_1(s)}{\Delta E(s)} - xFk_1\frac{\Delta\theta_3(s)}{\Delta E(s)} + ... \\ &... + xF(k_1b_1(1 - \theta_{1ss} - \theta_{3ss}) - \beta_1\theta_{1ss}k_{-1}b_{-1})\end{aligned} \tag{4.30}$$

The negative electrode faradic process of the impedance $Z_{fn}(s)$ is given by equation (4.31).

$$Z_{fn}(s) = \frac{\Delta E(s)}{\Delta I(s)} \tag{4.31}$$

The overall system impedance encompasses more than just the faradic processes. To accurately represent the system, it is essential to incorporate the solution resistance (R_s) and the interfacial capacitance (C_{dln}) between the negative electrode and electrolyte, as outlined in [88]. The resulting transfer function describing the negative electrode impedance is denoted as $Z_n(s)$.

$$Z_n(s) = R_s + \frac{1}{\frac{1}{Z_{fn}(s)} + C_{dln}s} \tag{4.32}$$

A similar process is applied to the positive electrode, yielding the transfer function in Equation (4.33). This function, combined with the negative electrode's transfer function, constitutes the overall battery impedance. The positive electrode model includes solution resistance (R_s), which is shared with the negative electrode, and electrode-specific elements: interfacial capacitance (C_{dlp}) and faradic impedance ($Z_{fp}(s)$). The transfer function for the positive electrode is detailed in Equation (4.33), as referenced in [96].

$$Z_p(s) = R_s + \frac{1}{\frac{1}{Z_{fp}(s)} + C_{dlp}s} \tag{4.33}$$

where $Z_{fp}(s)$ is equation (4.34):

$$\begin{aligned}\frac{1}{Z_{fp}(s)} = \frac{\Delta I(s)}{\Delta E(s)} =& xF(-k_2 - \beta_2 k_{-2})\frac{\Delta\theta_2(s)}{\Delta E(s)} - xFk_2\frac{\Delta\theta_4(s)}{\Delta E(s)} + ... \\ &... + xF(k_2 b_2(1 - \theta_{2ss} - \theta_{4ss}) - \beta_2\theta_{2ss}k_{-2}b_{-2})\end{aligned} \tag{4.34}$$

Obtaining the transfer function (4.35) from the impedance of a lead-acid battery ($Z_{Tg}(s)$), however, this transfer function is generalized for the battery technology used, so it is necessary to multiply the resulting function by the area of the electrodes.

$$Z_{Tg}(s) = Z_n(s) + Z_p(s) \tag{4.35}$$

4.1.4 Electrodes area consideration

The developed mechanistic model reflects the battery reaction for a specific surface area. Therefore, to account for the actual electrode sizes, each electrode model (negative and positive) needs to be scaled by its corresponding area factor (represented by M_n and M_p, respectively). This scaling is incorporated in the final model presented in equation (4.36).

$$Z_T(s) = M_n Z_n(s) + M_p Z_p(s) \tag{4.36}$$

where $Z_T(s)$ is the total transfer function of the impedance for the used battery, giving the result of the desired mechanistic model, however, for this work it is of interest to know the time constants of this model and in turn the poles related to said constants.

For this, the transfer functions obtained are substituted in opposite order, modifying the transfer function of the negative electrode, equation (4.32), as (4.37).

$$M_n Z_n = M_n R_s + \frac{M_n}{\frac{1}{Z_{fn}(s)} + C_{dln}s} = M_n R_s + \frac{1}{\frac{1}{M_n Z_{fn}(s)} + \frac{C_{dln}}{M_n}s} \tag{4.37}$$

In the same way the transfer function of the positive electrode, equation (4.33), as (4.38).

$$M_p Z_p = M_p R_s + \frac{M_p}{\frac{1}{Z_{fp}(s)} + C_{dlp}s} = M_p R_s + \frac{1}{\frac{1}{M_n Z_{fp}(s)} + \frac{C_{dlp}}{M_p}s} \tag{4.38}$$

The mass balance equations are also influenced by the electrode area. This modification results in adjusted transfer functions for the adsorbed species on the negative electrode, as shown in Equations (4.39) and (4.40). This process was carried out in the same way for the positive electrode.

$$\frac{\Delta\theta_1(s)}{\Delta E(s)} = \frac{-(k_1-k_{-3}\beta_3)\frac{\Delta\theta_3(s)}{\Delta E(s)}+(k_1b_1(1-\theta_{1ss}-\theta_{3ss})-k_{-3}b_{-3}\beta_3\theta_{3ss}+\beta_1\theta_{1ss}(k_{-1}b_{-1}-k_3b_3))}{\beta_1 s+M_n(k_1+\beta_1(k_{-1}+k_3))} \tag{4.39}$$

$$\frac{\Delta\theta_3(s)}{\Delta E(s)} = \frac{(k_3\beta_1)\frac{\Delta\theta_1(s)}{\Delta E(s)}+k_3b_3\beta_1\theta_{1ss}+k_{-3}b_{-3}\beta_3\theta_{3ss}}{\beta_3 s+M_n k_{-3}\beta_3} \tag{4.40}$$

These transfer functions are of interest since when developing the model the resulting denominator is equal to the multiplication of the denominators of these transfer functions.

4.1.5 Time constant for each reaction

The first-order transfer functions, Equations (4.39) and (4.40), are characterized by their respective time constants, τ_1 show in equation (4.41) and τ_3 show in equation (4.43). These time constants represent the relaxation times for adsorbed lead and lead sulfate, respectively, on the negative electrode. By applying the same methodology to the positive electrode, analogous time constants, τ_2 and τ_4, are obtained for the corresponding adsorbed species on the positive electrode. These time constants are defined by equations (4.42) and (4.44).

$$\tau_1 = \frac{\beta_1}{M_n(k_1+\beta_1(k_{-1}+k_3))} \tag{4.41}$$

$$\tau_2 = \frac{\beta_2}{M_p(k_2+\beta_2(k_{-2}+k_4))} \tag{4.42}$$

$$\tau_3 = \frac{1}{M_n k_{-3}} \tag{4.43}$$

$$\tau_4 = \frac{1}{M_p k_{-4}[SO_4^{2-}]} \tag{4.44}$$

where $[SO_4^{2-}]$ represents the acid concentration. Both electrodes produce $PbSO_{4ads}$ at the same time, However, it is necessary that a process be carried out releasing electrons, so that these released electrons are used in the other electrode, therefore the production time of this element corresponds to the sum of both constants of time, onwards when referring to the time constant associated with the production of lead sulfate, τ_s will be used, defined as $\tau_s = \tau_3 + \tau_4$.

4.1.6 VRLA PS-260 battery mechanistic model

This study investigated two-electrode, power-symmetric PS-260 VRLA batteries (2 V, 6 Ah capacity). The positive and negative electrodes measured 41.30 mm x 72.40 mm

x 2.02 mm and 38.50 mm x 68.40 mm x 2.02 mm, respectively, and were separated by a nonwoven glass fiber material. Impedance measurements were performed over a frequency range of 10 mHz to 10 kHz using a 10 mV AC amplitude signal. All measurements were conducted at the battery's open-circuit potential, as described in [97].

To accurately model the battery, the weight and surface area of the electrodes were determined. The active material was extracted and weighed using an Ohaus Adventure analytical balance, while the electrode area was measured with a Mitutoyo Vernier caliper. The obtained results are summarized in Table 4.1.

Table 4.1: Mass and area measurements for VRLA PS-260 battery.

Measurement	Value	Units
Pb mass	0.132	g
PbO_2 mass	0.165	g
M_n (Pb)	2.633×10^{-3}	m^2
M_p (PbO_2)	2.99×10^{-3}	m^2

The kinetic parameters for the negative electrode reactions were obtained from Niya et al. [90], while those for the positive electrode were taken from Shah et al. [91]. These values are tabulated in Table 4.2. It is noteworthy that the rate constants associated with the formation and recombination of lead sulfate (K_3, K_{-3}, K_4, and K_{-4}) are identical for both electrodes.

Table 4.2: Reaction rate constants for VRLA battery.

Constants	Value	Units
K_1	0.0078	mol m^{-2} s^{-1}
K_{-1}	218	mol m^{-2} s^{-1}
K_2	3.495×10^{-16}	mol^{-1} m^{-2} s^{-1}
K_{-2}	128.7321	mol^{-1} m^{-2} s^{-1}
K_3, K_4	9.34×10^{-12}	mol^{-1} m^{-2} s^{-1}
K_{-3}, K_{-4}	4.44	s^{-1}

The time constant (τ) for each reaction can be determined. The settling time, defined as four times the time constant ($t_s = 4\tau$), represents the time required to reach steady-state conditions. For the overall system, the settling time (τ_s) is the sum of

the individual time constants (τ_3 and τ_4). The calculated time constants based on Equations (4.41) to (4.44) are presented in Table 4.3.

Table 4.3: Time constants for adsorbates reactions.

Time constant	Value	t_s
τ_1	0.217 s	0.871 s
τ_2	0.433 s	1.731 s
τ_s	13.306 s	53.224 s

With the entire process described above, the necessary data from the mechanistic model are obtained; however, it is necessary to establish an EEC model described in the following section.

4.2 Equivalent electric circuit characterization

In the realm of electrochemical modeling, EEC models occupy a middle ground between detailed chemical models and simplified input-output models. By approximating battery processes as electrical circuits, valuable insights into electrochemical phenomena can be gained, as suggested in [1].

For this work, the point of union between the models to be correlated will be the frequency response of the impedance, through the use of Nyquist graphs. To determine the EEC that adjusts to said impedance, it is necessary to understand that the graph obtained for the vast majority of battery technologies, including lead-acid, lithium ions, among others, has a shape similar to that shown in Figure 4.2, where the response of the battery impedance to a sweep of frequencies from highest to lowest is shown, graphed from left to right, respectively. Knowing that the resulting graph will follow this pattern and following the EEC model construction methods from the literature [98, 99], The circuit shown in the upper part of the figure is proposed. For this figure and all Nyquist plots the axes follow the following nomenclature: the x-axis (Z') represents the real component of the impedance measured in ohms (Ω); the y-axis (jZ'') represents the imaginary component of the impedance measured in ohms (Ω).

The equivalent circuit model consists of several components. The solution resistance (R_s) is represented by the intersection of the impedance plot with the real axis. The charge transfer process is modeled by a parallel combination of resistance (R_1) and constant phase element (CPE_1), corresponding to the loop-shaped region in the Nyquist plot bounded by the orange lines. The subsequent linear portion of the plot is represented by two RC circuits (R_2C_2 and R_3C_3), following the approach outlined in [100].

The constant phase element (CPE_1) is a representation of a non-ideal capacitor, which tends to change its value with respect to frequency, which physically is understood as a virtual capacitor inside the battery which changes the conditions of its dielectric. due to the transformation of the electrodes [12, 100].

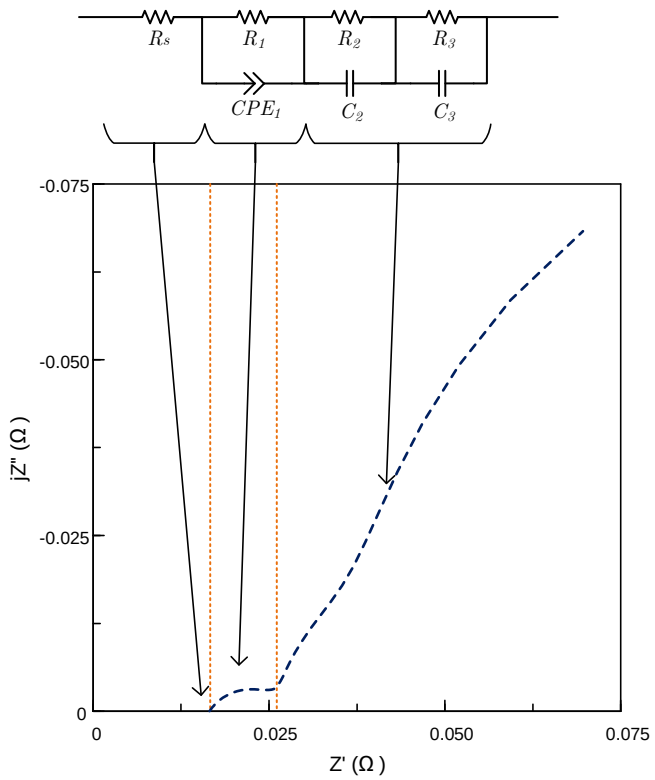

Figure 4.2: Expected Nyquist plot for the battery impedance and the relationship with the EEC used.

While the previously described model provides a theoretical framework for battery impedance, practical measurement necessitates more sophisticated techniques. Electrochemical impedance spectroscopy (EIS) is the established method for characterizing battery impedance experimentally.

4.2.1 Electrochemical Impedance Spectroscopy Analysis

Electrochemical impedance spectroscopy (EIS) is a non-destructive method for studying the behavior of the electrode-electrolyte interface, as detailed in [101]. This technique involves applying a chirp signal, a linearly swept frequency modulation signal, to

the system (as described in [102, 103]). The complex electrochemical impedance is subsequently determined by analyzing the resulting voltage response in relation to the applied current, as outlined in [104, 105].

Measured impedance reflects the influence of two primary processes.

- Faradic processes, as described in (4.31), involve the exchange of electrons.
- Nonfaradic processes, as described in (4.32) by R_s and C_{dln}, that represent the physical constraints on the active material.

A VersaSTAT 3F potentiostat-galvanostat was employed to measure the impedance of a PS260 battery. The resulting Nyquist plots were analyzed using ZView2 software to extract relevant impedance parameters, as detailed in [98].

The previously determined time constants from Table 4.3 were integrated with the measured impedance data to analyze the dynamic contributions of individual reactions. The frequency response of the battery impedance, as illustrated in Figure 4.3, provides insights into these contributions.

- The solution resistance R_s as the intersection with the abscissa axis at $Z' = 0.011$ Ω.
- The adsorbed lead from the negative electrode (4.3) is represented by the green area.
- The adsorbed lead from the positive electrode (4.5) is represented by the green and yellow areas.
- The sulfate production from (4.4) and (4.6) is represented by the green, yellow and red areas.
- The Z' complex values exceeding the previously mentioned areas represent the diffusion effects from $Z' = 0.036$ Ω to the end of the Nyquist plot.

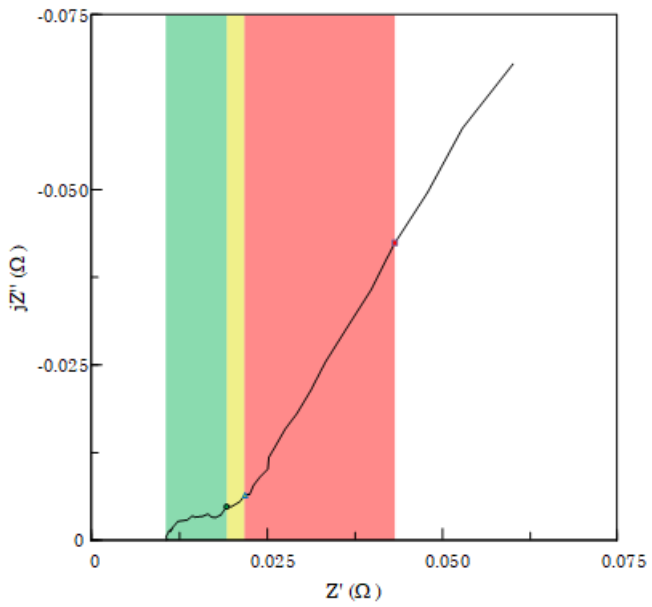

Figure 4.3: Nyquist plot response for a new battery at 100% SOC. The colored regions represent the different time constants for the processes occurring.

The electrochemical reactions underpinning the battery's charge and discharge processes directly influence its impedance characteristics, including response times. By correlating these impedance features with the EEC model, a deeper understanding of the underlying physical mechanisms can be achieved, as outlined in [106].

In order to validate that the measurements obtained are repeatable, the measurements were repeated with different batteries in new conditions, obtaining the measurements in Figure 4.4, where 3 different batteries are shown, it is observed that the measurements are not exactly the same but they are close, the differences between these measurements are due to the small variations produced at the time of manufacturing, any way the results prove that the procedure develop in this work is consistent.

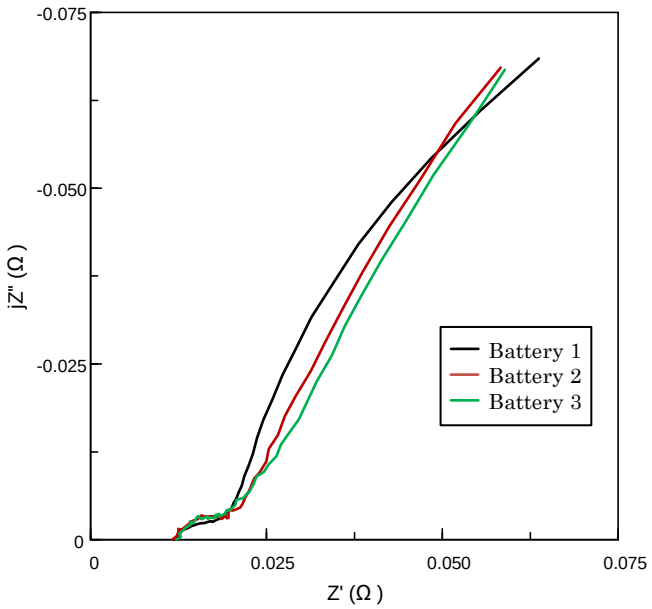

Figure 4.4: Nyquist plot response for 3 new batteries at 100% SOC, to prove repetitiveness.

The process of fitting the proposed EEC model to the experimental impedance data was automated using the ZView2™ software package, which employs the Levenberg-Marquardt algorithm, as described in [107]. The resulting EEC model comprises three parallel RC circuits, as visualized in Figure 4.3. The model components include a solution resistance (R_s), a charge transfer resistance (R_1) in parallel with a constant phase element (CPE_1), and two additional RC circuits (R_2C_2 and R_3C_3). Following the approach outlined in [98, 99, 100].

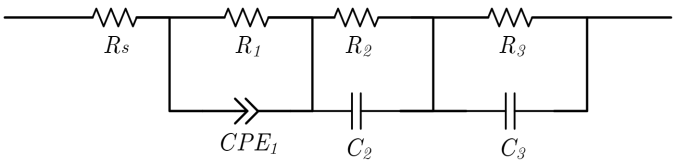

Figure 4.5: The EEC model was used to adjust the EIS data for all the experimental conditions tested.

By using [108], an equivalent capacitor C_1 for CPE_1 is considered, given by:

$$C_1 = \frac{(Y_0 R_1)^{1/a}}{R_1} sin(\frac{a\pi}{2}) \tag{4.45}$$

where Y_0 and a are the characteristic parameters of CPE_1 and R_1 is the parallel resistance.

The refined EEC model provides a significantly improved fit to the experimental impedance data, as evident in Figure 4.6, where the modeled data (dashed line) closely aligns with the measured data (continuous line). Within this figure, the dynamic contributions of the R_1C_1, R_2C_2 and R_3C_3 circuit elements are highlighted in regions 1, 2, and 3, respectively. By comparing the modeled and experimental Nyquist plots, the relative importance of the included reactions within the mechanistic model can be assessed. Although the model captures the dominant processes, it's essential to acknowledge the presence of additional electrochemical phenomena within the battery.

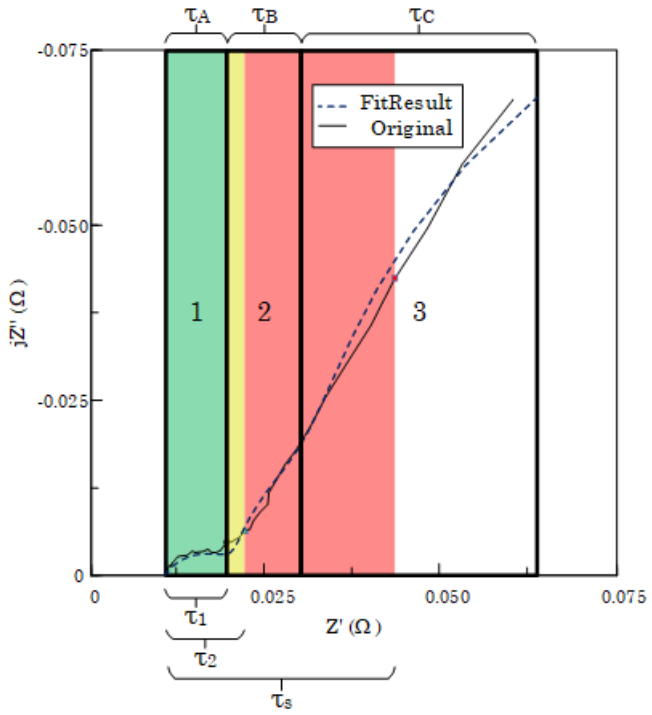

Figure 4.6: Nyquist plot response for a new battery at 100% SOC. The colored regions and the bold rectangular outlines show comparisons of the experimental (τ_1, τ_2 and τ_s) and modeled (τ_A, τ_B and τ_C) time constants.

- $R_1C_1 = \tau_A$ corresponds to the charge transfer and release of lead adsorbed on the negative electrode related to (4.3).
- $R_2C_2 = \tau_B$ corresponds to the Pb^{2+}_{ads} at the positive electrode and the release of oxygen that produces water (4.5), and the simultaneous generation of $PbSO_{4ads}$ according to (4.4) and (4.6).

- $R_3C_3 = \tau_C$ corresponds to the generation of $PbSO_{4ads}$ and the diffusion of sulfates in the electrolyte related to (4.4) and (4.6).

A methodology for correlating the mechanistic and equivalent circuit models is proposed and illustrated in Figure 4.7. The following steps outline this approach:

- Develop a mechanistic model representing battery impedance as a frequency-domain transfer function.
- Extract system poles and associated time constants from the transfer function denominator using control theory principles. Each pole corresponds to a specific reaction (equations (4.3), (4.4), (4.5), (4.6))
- Assuming a time-frequency relationship, determine characteristic frequencies of each pole by solving the characteristic polynomial (Step 3 in Figure 4.7). These frequencies associated to the time constants (p_{τ_1}, p_{τ_2}, ..., p_{τ_q}) quantify the dynamic contribution of each pole.
- Identify frequency regions associated with each pole's dynamic contribution by tracing the corresponding pole frequency in the impedance spectrum.
- Correlate EEC model poles with specific Nyquist plot regions to identify the contribution of each mechanistic reaction.

The proposed methodology for correlating electrochemical phenomena with electrical circuit elements is graphically illustrated in Figure 4.7. By establishing this link, changes in circuit parameters can be attributed to specific battery aging mechanisms.

To study the validity and scope of the proposed correlation, it is necessary to study the behavior of the impedance throughout the useful life of the battery, for this purpose the previously aged batteries will be taken according to the test described in Chapter 3, the Results of these tests are detailed in the following section.

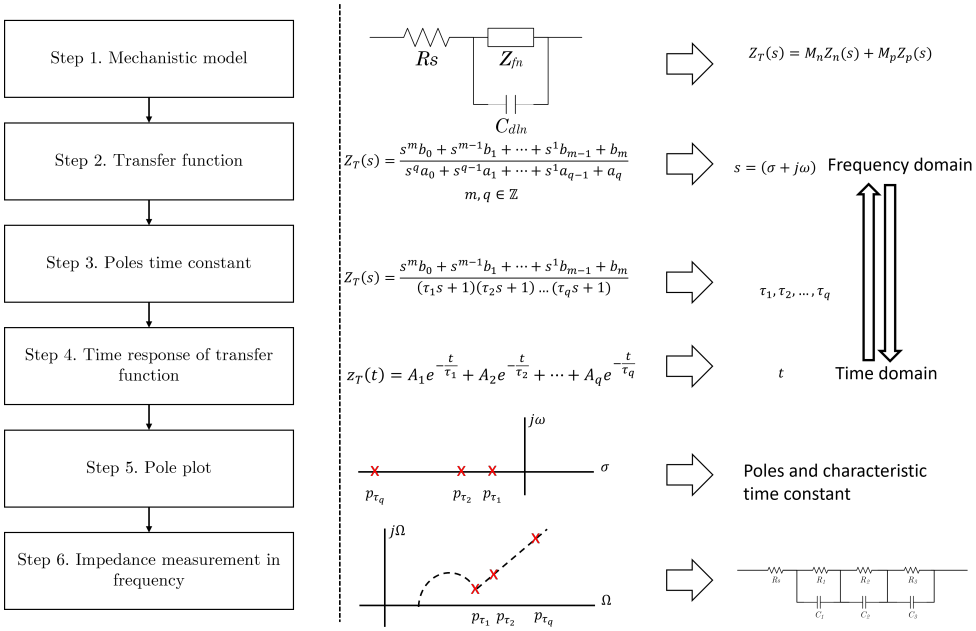

Figure 4.7: Flow chart for obtaining the semiempirical model.

4.3 Results and Discussion

Battery impedance is dynamic and influenced by various factors. To assess the model's performance across different battery states, impedance measurements were conducted at multiple stages of battery life during charge-discharge cycles. Battery aging was evaluated under controlled conditions at room temperature (approximately 303 K) using a constant current discharge of 0.2C (equivalent to 1.2 A for a 6 Ah battery). Batteries with 0, 50, 100, 150, and 200 cycles were examined, as battery life typically ends around 200 cycles when the battery can no longer meet the required current demands.

Batteries at different SOC were subjected to EIS analysis. The resulting Nyquist plots were analyzed to determine the poles associated to the time constants (τ_1, τ_2, and τ_s) related with the underlying electrochemical reactions.

The data show that the impedance magnitude increases as the battery ages; To exemplify this, Figure 4.8 shows the impedance measurements obtained from the batteries at 100% of the SOC, evidencing how the impedance of the battery increases as we age, separating by color for easy appreciation, however, due to the scale it is difficult to visualize the changes, therefore they will be analyzed in isolation, comparing measurements and analyzing the trends shown in each graph.

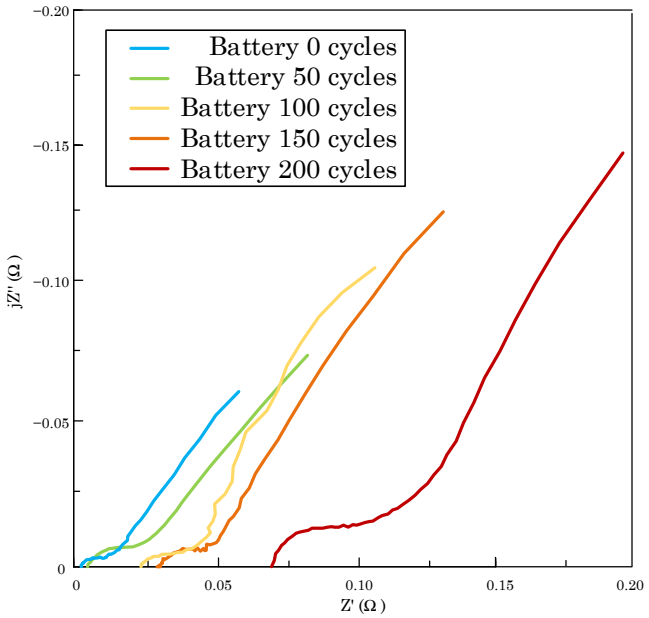

Figure 4.8: Nyquist plot for batteries with different aging cycles.

Figure 4.9 displays the impedance spectra for both fully charged (100% SOC, blue lines) and completely discharged (0% SOC, orange lines) batteries at various aging stages (0, 50, 100, 150, and 200 cycles). The graphs are marked with symbols to highlight the frequency range where each time constant (τ_1) associated with the cathodic reaction (Equation (4.3)), (τ_2) for the anodic reaction (Equation (4.5)), and (τ_s) for the combined reactions (Equations (4.4) and (4.6)) has a significant influence. Similar to Figure 4.3, each impedance plot (100% and 0% SOC) includes a pair of bars at the bottom visually representing the contribution of each reaction on the real axis.

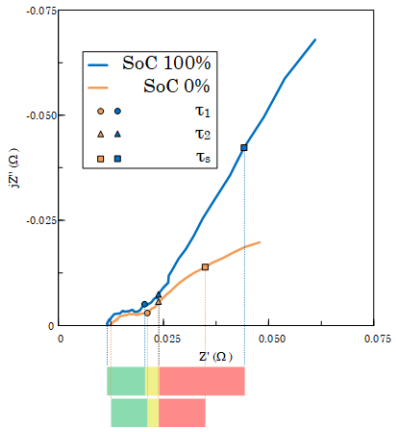

(a)

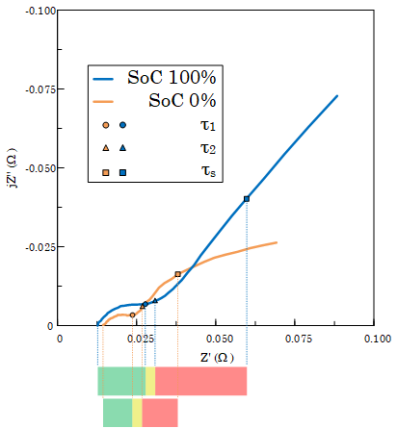

(b)

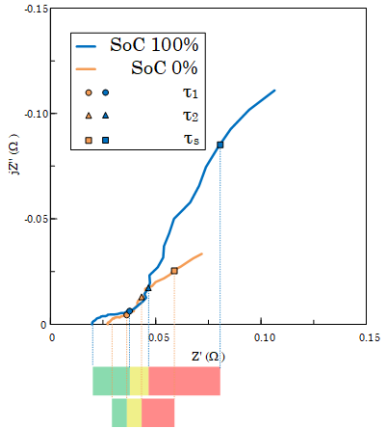

(c)

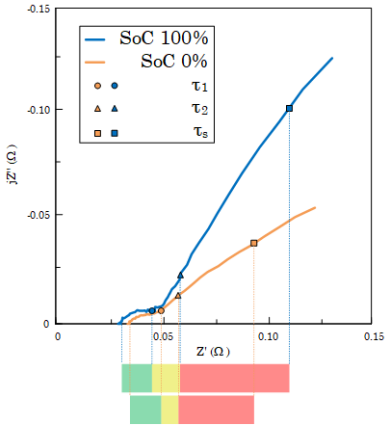

(d)

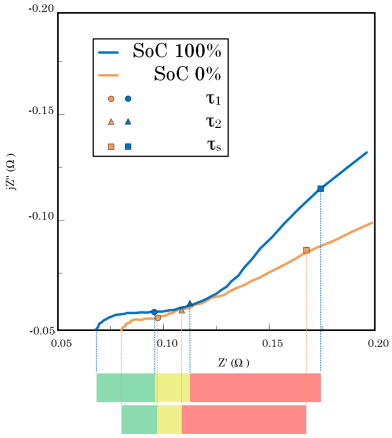

(e)

Figure 4.9: Nyquist plot response of a battery under different aging cycles. The markers depict the limit for each time constant at 0 and 100% of SOC, (a) 0 aging cycles, (b) 50 aging cycles, (c) 100 aging cycles, (d) 150 aging cycles, (e) 200 aging cycles.

The impedance increase is analyzed numerically evaluating the real component of the impedance at the frequency related to τ_s; where, $Z'_0(\tau_s) = 0.0482\ \Omega$, $Z'_{50}(\tau_s) = 0.0598\ \Omega$, $Z'_{100}(\tau_s) = 0.0856\ \Omega$, $Z'_{150}(\tau_s) = 0.1022\ \Omega$, and $Z'_{200}(\tau_s) = 0.1174\ \Omega$, the subindex represents the aging cycles, for 100% SOC. These values correspond to the blue square depicted on blue lines from Figure 4.9 (a) to Figure 4.9 (e); The time constants associated with each reaction correspond to the values in the penultimate row of Table 4.4. Notably, impedance magnitude decreases as the state of charge (SOC) drops, regardless of battery age. For instance, the impedance at the τ_s time constant's frequency ($Z'_{50}(\tau_s)$) is 0.0598 Ω at 100% SOC and 0.0410 Ω at 0% SOC for a battery aged 50 cycles. Similarly, for a 200-cycle battery, $Z'_{200}(\tau_s)$ is 0.1174 Ω and 0.1153 Ω at 100% and 0% SOC, respectively. However, the difference in impedance between full and empty states diminishes with increasing aging, as detailed in Table 4.4 and visually represented by the length of the color bars below each impedance plot.

Table 4.4: Impedance obtained from Nyquist plots shown in Figure 4.9.

SOH	New (0 *cycles*) 0% of aging		50 *cycles* 25% of aging		100 *cycles* 50% of aging		150 *cycles* 75% of aging		200 *cycles* 100% of aging	
SOC	100%	0%	100%	0%	100%	0%	100%	0%	100%	0%
R_s (Ω)	0.011	0.012	0.012	0.016	0.022	0.031	0.03	0.038	0.068	0.08
$Z'(\tau_1)$ (Ω)	0.019	0.020	0.027	0.025	0.038	0.034	0.047	0.049	0.097	0.099
$jZ''(\tau_1)$ (Ω)	−0.0049	−0.002	−0.006	−0.004	−0.006	−0.004	−0.006	−0.004	−0.009	−0.007
$Z'(\tau_2)$ (Ω)	0.022	0.021	0.031	0.026	0.043	0.041	0.051	0.053	0.102	0.103
$jZ''(\tau_2)$ (Ω)	−0.006	−0.003	−0.008	−0.006	−0.009	−0.006	−0.01	−0.007	−0.011	−0.009
$Z'(\tau_s)$ (Ω)	0.048	0.041	0.059	0.041	0.085	0.061	0.102	0.096	0.117	0.115
$jZ''(\tau_s)$ (Ω)	−0.049	−0.017	−0.054	−0.024	−0.082	−0.024	−0.09	−0.037	−0.096	−0.029

Table 4.4 provides numerical data corresponding to the graphical results displayed in Figure 4.9.

- The R_s values can be found at the intersection of the blue and orange lines with the real axis.
- The impedance values, represented by $Z'(\tau_1)+jZ''(\tau_1)$, correspond to the circular markers on the blue and orange lines in Figures 4.9 (a) to (e).
- The impedance values, represented by $Z'(\tau_2) + jZ''(\tau_2)$, correspond to the triangles markers on the blue and orange lines in Figures 4.9 (a) to (e).
- The impedance values, represented by $Z'(\tau_s)+jZ''(\tau_s)$, correspond to the squares markers on the blue and orange lines in Figures 4.9 (a) to (e).

Table 4.4 summarizes the numerical data extracted from the impedance plots in Figures 4.9 (a) to (e), differentiating between 100% and 0% SOC conditions, represented by blue

and orange lines, respectively. The graphical representation of these data is presented in Figure 4.10, followed by a detailed interpretation.

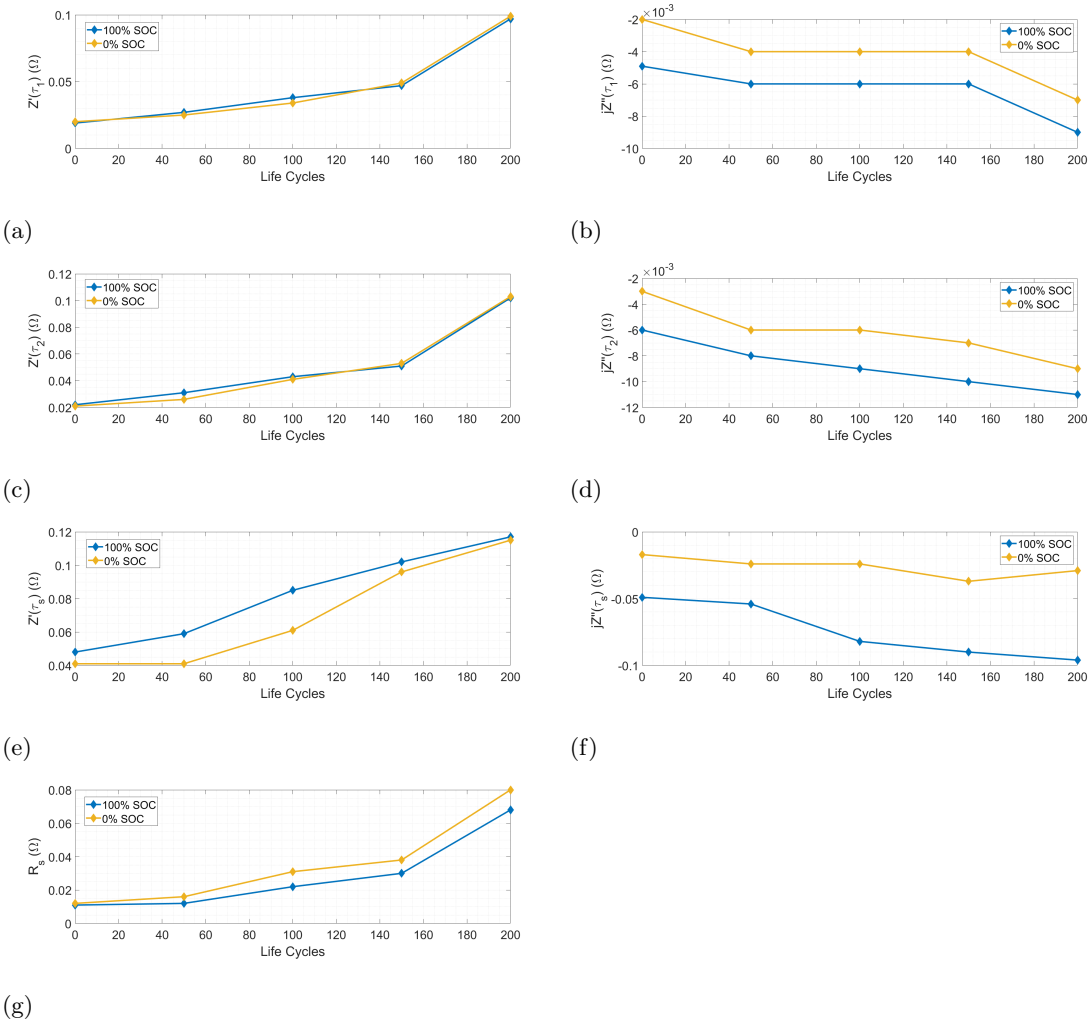

Figure 4.10: Impedance trends of mechanistic reaction model according to Table 4.4. (a) and (b) are the real and imaginary impedance ($Z'(\tau_1)$ and $jZ''(\tau_1)$) respectively, (c) and (d) are the real and imaginary impedance ($Z'(\tau_2)$ and $jZ''(\tau_2)$) respectively, (e) and (f) are the real and imaginary impedance ($Z'(\tau_s)$ and $jZ''(\tau_s)$) respectively, and (g) is the R_s trend.

The solution resistance (R_s) exhibits an increasing trend with decreasing SOC for all aging conditions, as evidenced by the R_s values in Table 4.4. Additionally, R_s progressively increases with the overall aging of the battery.

The time constant associated with the slowest reaction, τ_s, exhibits the most

significant increase across all conditions, suggesting it as the rate-determining step in the overall electrochemical process. This is corroborated by its dominant contribution to the system's dynamics, as indicated by its larger impedance magnitude compared to τ_1 and τ_2 in Figure 4.9(a). In contrast, the reaction linked to τ_2 shows minimal changes in its real impedance magnitude with varying SOC, as evidenced by the data in Table 4.4. As the SOC decreases, the frequency markers representing τ_1, τ_2, and τ_s shift closer to the real axis, indicating a reduction in diffusion processes. This trend is visually apparent in the decreasing slope of the impedance plots between 100% and 0% SOC.

The preceding analysis has focused on qualitative observations. To provide a quantitative perspective, the impact of SOC on battery behavior under normal aging conditions is summarized in Table 4.4.

To validate the previously described behavior within the EEC framework, the EEC parameters were estimated for various aging states and SOC levels using the ZView2™ simulator. Table 4.5 summarizes the obtained results. The goodness-of-fit between the measured and modeled data was assessed using the chi-square test, which yielded a value of approximately $1 \times 10^{-}3$, indicating a strong statistical relationship.

Table 4.5: EIS parameters calculated using the EEC model shown in Figure 4.5.

SOH	New (0 *cycles*)		50 *cycles*		100 *cycles*		150 *cycles*		200 *cycles*	
	0% of aging		25% of aging		50% of aging		75% of aging		100% of aging	
SOC	100%	0%	100%	0%	100%	0%	100%	0%	100%	0%
R_s (Ω)	0.011	0.012	0.012	0.016	0.022	0.031	0.03	0.038	0.068	0.08
R_1 (Ω)	0.017	0.022	0.024	0.015	0.021	0.01	0.028	0.023	0.006	0.044
C_1 (F)	16.62	4.552	6.283	8.07	4.177	7.795	2.1	2.404	0.607	0.014
τ_A (s)	0.289	0.102	0.154	0.125	0.09	0.081	0.058	0.057	0.003	6.533×10^{-4}
R_2 (Ω)	0.013	0.018	0.013	0.02	0.024	0.02	0.03	0.131	0.021	0.14
C_2 (F)	302.50	159.00	354.30	104.20	85.23	151.50	67.50	10.43	43.95	1.21
τ_B (s)	4.01	2.999	4.881	2.147	2.118	3.17	2.041	1.37	0.93	0.17
R_3 (Ω)	0.256	0.065	0.257	0.046	0.263	0.023	0.287	0.224	0.695	0.366
C_3 (F)	250.1	238.0	228.8	220.1	180.4	257.0	143.8	58.5	58.9	23.5
τ_C (s)	64.15	15.52	58.888	10.217	47.517	6.117	41.395	13.16	40.983	8.638
χ^2	2.2×10^{-3}	1.5×10^{-3}	1.5×10^{-3}	2.2×10^{-3}	0.9×10^{-3}	2.8×10^{-3}	1.2×10^{-3}	0.9×10^{-3}	$2.1 \times 10{-}3$	1.3×10^{-3}

Table 4.5 presents the results obtained from the ZView2™ software utilized to fit the EEC model parameters to the EIS measurements displayed in Figure 4.9. Additionally, Figure 4.11 provides a graphical representation of the data in Table 4.5 for enhanced clarity. A comparative analysis of the results in Tables 4.4 and 4.5, alongside the corresponding plots in Figures 4.10 and 4.11, reveals a consistent trend in the behavior of the time constants (τ_s) across varying SOC and aging conditions. This observation serves as validation for the established correlations between the mechanistic and electrical models across all operational points.

Specifically, the time constant τ_A exhibits a progressive decrease with diminishing SOC, mirroring the behavior of τ_1. This trend coincides with the observed increase in $jZ''(\tau_1)$ and the widening gap between R_s and $Z'(\tau_1)$. These observations align with

the expected behavior of the reaction described by Equation (4.3).

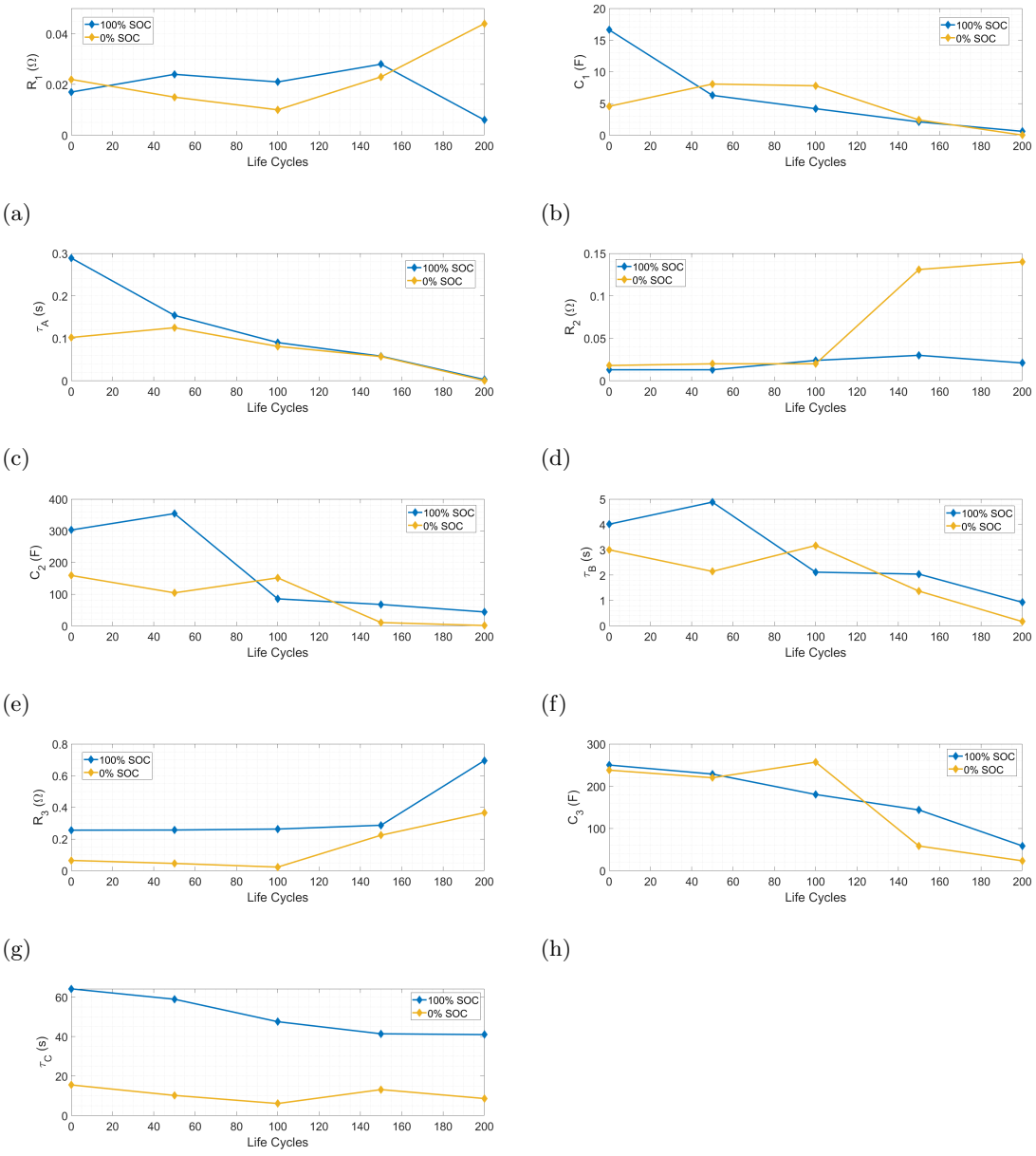

Figure 4.11: Fitted parameters trends of EEC model from data of Table 4.5. (a), (b), and (c) corresponds to R_1, C_1, and τ_A trend, respectively, (d), (e), and (f) corresponds to R_2, C_2, and τ_B trend, respectively, (g), (h), and (i) corresponds to R_3, C_3, and τ_C trend, respectively.

The time constant τ_B represents a transitional region where the individual contributions of sulfate generation and adsorbate release from the positive electrode cannot be distinctly identified, as indicated by region 2 in Figure 4.12. Nevertheless, an overall decreasing trend is observed for τ_B due to the combined decline in both τ_2 and τ_s, evident in the values of $jZ''(\tau_2)$ and $jZ''(\tau_s)$ within Table 4.4. The relatively minor variations in τ_B can be attributed to the minimal changes in $jZ''(\tau_2)$, as graphically depicted by the yellow bars in Figure 4.9.

The time constant τ_C is associated with both sulfation (represented by squares in Figure 4.9) and diffusion processes, the latter being linked to the peak impedance values at 100% and 0% SOC in Figure 4.9. As the battery discharges, both sulfation and diffusion effects move closer to the real axis on the impedance plot. This shift is attributed to the increasing distance between the active material and electrolyte caused by sulfate crystal growth, leading to a decrease in capacitance (C_3). The linear impedance behavior between the sulfation region and the end point is also influenced by the decreasing ion mobility through the electrolyte due to sulfate agglomeration, which is reflected in the reduced value of τ_C.

Among the identified time constants, τ_C exhibits the most pronounced influence within the EEC model. Conversely, τ_s holds the greatest significance within the mechanistic model. To establish a correlation between these models, the real part of the impedance associated with τ_s, $Z'(\tau_s)$, is compared to the resistance R_3. Both parameters demonstrate a decreasing trend with declining SOC. Furthermore, an increase in battery aging leads to a rise in both R_3 and $Z'(\tau_s)$ values.

It is noteworthy that the capacitance values (C_1, C_2 and C_3) exhibit a general decreasing trend with battery aging, as evidenced by the diminishing slope of the diffusion-related line in Figure 4.9.

Table 4.6 presents a comparative analysis to validate the enhanced approximation capabilities of the proposed time-variant model over the time-invariant model. Simulations were conducted using the parameter values from the first column of Table 4.5 for the time-invariant model and all data from the same table for the time-variant model. Relative errors, calculated using Equation (4.46), were assessed for both models over a complete charge-discharge cycle. Results indicate lower average and maximum errors for the time-variant model compared to the time-invariant model.

Table 4.6: Error between the conventional time-invariant model and the proposed time-variant model with respect to the battery measurements.

Aging cycles	Average error invariant model (%)	Average error variant model (%)	Maximum error invariant model (%)	Maximum error variant model (%)
0	0.69	0.69	3.90	3.90
50	1.89	0.87	4.86	4.16
100	2.61	1.42	6.00	4.52
150	2.87	2.24	7.82	6.90
200	3.82	2.25	10.30	7.00

$$Error(\%) = \frac{\mid v_{batt_{measured}} - v_{batt_{model}} \mid}{v_{batt_{measured}}} * 100 \tag{4.46}$$

where $Error(\%)$ is the relative error, $v_{batt_{measured}}$ is the battery voltage measured along a complete charge/discharge cycle, and $v_{batt_{model}}$ is the battery voltage obtained from simulation model along the same cycle.

To evaluate the accuracy of the EEC model parameters determined through the previous methodology, simulations were conducted using current and differential voltage data collected from a complete charge-discharge cycle of a PS-260 battery. The battery current served as the model input, while the output was the differential terminal voltage. A linear relationship between open-circuit voltage and state of charge, as reported in [68] and bounded by the battery's voltage limits (2.24 V and 1.8 V) from [71], was assumed. Figure 4.12 compares the simulated and measured voltage profiles, demonstrating good agreement, for the simulation the values in the Table 4.5 were used for a time-variant model. These results were obtained using a new battery and maintained consistency over 200 charge-discharge cycles.

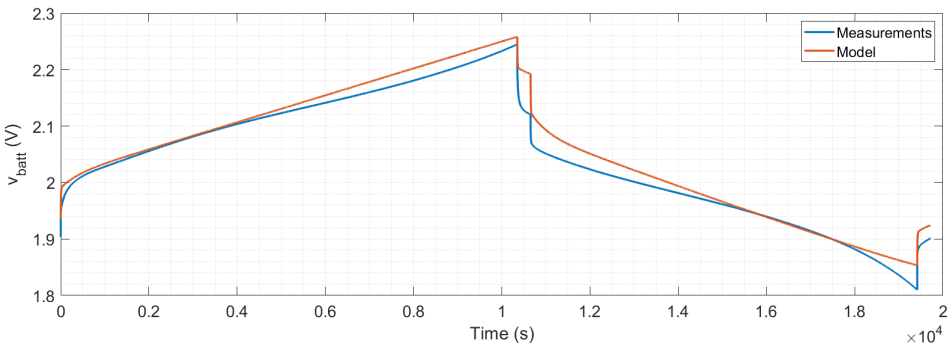

Figure 4.12: Semi-empirical model validation with real data from PS-260 battery.

The proposed time-variant model encompasses the influence of various aging

mechanisms, including corrosion, hard sulfation, and active material loss, as documented in [1]. While these mechanisms occur concurrently, their individual contributions to overall battery degradation are challenging to isolate. Nonetheless, each mechanism collectively impacts the observed changes in impedance spectra. By employing the proposed semi-empirical model, it is postulated that these distinct aging effects can be differentiated. For instance, the time constant associated with active material loss, being primarily influenced by electrical and surface phenomena, is the shortest. Corrosion, affecting electrode composition and the electrode-electrolyte interface, follows in terms of time scale. Lastly, hard sulfation, characterized by its impact on diffusion and mass transport, exhibits the longest associated time constant.

A combined analysis of Figure 4.9 and the numerical data in Tables 4.4 and 4.5 confirms the validity and consistency of the proposed electrochemical phenomena within the equivalent electrical circuit (EEC) model across the entire range of battery state of charge (SOC) and lifespan.

In this way we can obtain from this Chapter a configuration of passive elements for the EEC model, which, unlike the model in Chapter 3, is capable of giving a physical meaning to the present parametric changes, contributing to the study of aging. Additionally, it is now necessary to analyze the estimation of the amount of stored energy, which is described in the next Chapter.

Chapter 5

Battery aging model with parametric variations

In this chapter, a SOC observer is developed for the EEC model resulting from the analyzes presented above. Likewise, the evolution of the parametric changes seen as multiplicative signals to the model is studied, thus proposing a state space capable of representing these variations, checking their extent throughout the useful life of the battery and checking their performance for controlled cases of overcharge and overdischarge.

According to the results obtained in the previous chapters, the EEC model that will be used is shown in Figure 5.1, which represents the impedance of the battery through its passive elements, associating said elements with internal electrochemical reactions.

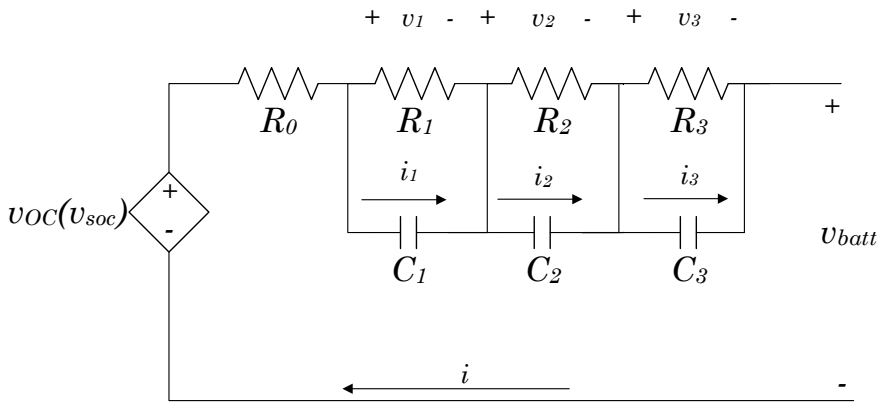

Figure 5.1: Equivalent Electric Circuit (EEC) for the battery modeling.

This model has an associated and well-known state space (5.1), obtained by applying

Kirchhoff's laws [100].

$$\begin{aligned} \dot{\mathbf{x}} &= \mathbf{A}\mathbf{x} + \mathbf{B}i \\ v_{batt} &= h(\mathbf{x}) + \mathbf{D}i \end{aligned} \tag{5.1}$$

where $\mathbf{x} \in \mathbb{R}^4$, $i \in \mathbb{R}$, and $v_{batt} \in \mathbb{R}$; defining the matrixes $\mathbf{x}$, $\mathbf{A}$, $\mathbf{B}$, and $\mathbf{D}$ as (5.2) [4].

$$\begin{aligned} \mathbf{x} = \begin{bmatrix} v_1 \\ v_2 \\ v_3 \\ v_{SOC} \end{bmatrix}; \mathbf{A} = \begin{bmatrix} -\frac{1}{\tau_A} & 0 & 0 & 0 \\ 0 & -\frac{1}{\tau_B} & 0 & 0 \\ 0 & 0 & -\frac{1}{\tau_C} & 0 \\ 0 & 0 & 0 & 0 \end{bmatrix}; \\ \mathbf{B} = \begin{bmatrix} \frac{1}{C_1} \\ \frac{1}{C_2} \\ \frac{1}{C_3} \\ -\frac{1}{C_{available}} \end{bmatrix}; \mathbf{D} = \begin{bmatrix} -R_0 \end{bmatrix}; \end{aligned} \tag{5.2}$$

Likewise $h(\mathbf{x})$ is the function (5.3) and the parameters τ_A, τ_B, and τ_C represent the multiplication of R_1C_1, R_2C_2, and R_3C_3, respectively.

$$h(\mathbf{x}) = -v_1 - v_2 - v_3 + v_{OC} \tag{5.3}$$

where v_1 correspond to the voltage in the parallel arrangement R_1C_1, v_2 correspond to the voltage in the parallel arrangement R_2C_2, and v_3 correspond to the voltage in the parallel arrangement R_3C_3. The function $h(\mathbf{x})$ adds nonlinearity.

Once the problem of parameter correlation has been addressed to redefine the physical meaning of the variables, it is necessary to guarantee the estimation of the SOC. The results previously obtained have a behavior close to the measurements using the Coulomb Counting method. However, this method has some deficiencies: It is highly dependent on the quality of the current measurement, so any change in the sensor or external conditions diverts the result [12]. In the same way, it is highly susceptible to changes due to the initial values, causing an accumulation of errors that must constantly restart the integral [86]. Even so, when applied in the long term or in conditions far from the initial ones, this method tends to be far from the actual values, which puts the battery at risk since it can lead to undetected over-charging and over-discharging situations [109].

To avoid the aforementioned and take care of the batteries, it is proposed to use an observer, which, through a correction matrix, will compensate for the deficiencies of Coulomb Counting method. The observer selected for this application is an observer for systems with a nonlinear output map.

5.1 Observer for systems with a nonlinear output map

Observers are a widely used tool to understand non-measurable state variables. In the case of nonlinear systems, observers have been developed. However, these apply to models with a nonlinear equation of states and a linear output equation [110]. Even so, there are nonlinear systems whose equation of states is linear and the output equation is nonlinear, known as systems with nonlinear output maps. A system of form (5.1) is considered for designing an observer under these conditions [111, 112].

$$\begin{aligned} \dot{\mathbf{x}} &= \mathbf{A}\mathbf{x} + \mathbf{B}\mathbf{u} \\ \mathbf{y} &= h(\mathbf{x}) + \mathbf{D}\mathbf{u} \end{aligned} \tag{5.4}$$

where $\mathbf{x} \in \mathbb{R}^n$, $\mathbf{u} \in \mathbb{R}^m$, $\mathbf{y} \in \mathbb{R}^q$, $h(\mathbf{x})$ is nonlinear. A nonlinear observer is proposed for this type of system according to equation (5.5).

$$\begin{aligned} \dot{\hat{\mathbf{x}}} &= \mathbf{A}\hat{\mathbf{x}} + \mathbf{B}u + \mathbf{H}\nabla h^T(\hat{\mathbf{x}})(\mathbf{y} - \hat{\mathbf{y}}) \\ \hat{\mathbf{y}} &= h(\hat{\mathbf{x}}) + \mathbf{D}\mathbf{u} \end{aligned} \tag{5.5}$$

where $\nabla h(\hat{\mathbf{x}}) = \dfrac{\partial h(\hat{\mathbf{x}})}{\partial \mathbf{x}}$ and $\mathbf{H}$ the correction matrix. The error dynamic between the system and the observer is defined as (5.6).

$$\dot{\mathbf{e}}_x = \dot{\mathbf{x}} - \dot{\hat{\mathbf{x}}} = (\mathbf{A} - \mathbf{H}\nabla h^T(\hat{\mathbf{x}})\nabla h(\hat{\mathbf{x}}))\mathbf{e}_x \tag{5.6}$$

This observer needs to fulfill some conditions according to [111]:

- Case 1: If all the eigenvalues of matrix $\mathbf{A}$ have a negative real part, it must be verified that matrix A is Hurwitz.
- Case 2: If there is only one eigenvalue equal to 0 and the rest have a negative real part, Liapunov stability must be checked.

In any case, it must be verified that the nonlinear component of the system is Lipschitz.

5.2 State-of-charge battery observer

According to the state space (3.8). The system has the form of (5.1), and the application of this observer has already been tested in other battery technologies, such as lithium ions [112, 113], sharing a structure similar to the model used in this work.

Furthermore, the values of the resistors and capacitors change with respect to the SOC and SOH variation, which will increase the deviation between the model and actual measurements. The selected observer also is robust against those variations

since the correction vector will adjust the model to follow the measurements. In this way, the observer's dynamics will include the effect of the parametric changes within the observed state. This observer will not only lead the system to correct monitoring but also allow us to know the evolution of the dynamic response throughout its useful life, information that will be vital when analyzing cases of overcharge and over-discharge. The observer design is described in detail as follows.

Since the system falls into case 2, the following corollaries must be checked:
Corollary 4.1[Zero eigenvalues.] $\mathbf{A}$ is allowed to have one eigenvalue with $\mathrm{Re}\{\lambda_j(\mathbf{A})\} = 0$ and all other eigenvalues $\mathrm{Re}\{\lambda_i(\mathbf{A})\} < 0$, with the observer structure (5.5) where the matrix $\mathbf{H}$ is diagonal and positive defined solution for the Lyapunov equation (5.7).

$$\mathbf{A}^T\mathbf{H}^{-1} + \mathbf{H}^{-1}\mathbf{A} = -\mathbf{Q} \tag{5.7}$$

where the design matrix $\mathbf{Q}$ is symetric and positive semidefinite and $rk(\mathbf{A}) \equiv rk(\mathbf{Q})$

Proof. Considering a matrix $\mathbf{Q}$ as (5.8):

$$\mathrm{Q} = \begin{bmatrix} 2/k_1 & 0 & 0 & 0 \\ 0 & 2/k_2 & 0 & 0 \\ 0 & 0 & 2/k_3 & 0 \\ 0 & 0 & 0 & 0 \end{bmatrix} \tag{5.8}$$

where k_1, k_2, and k_3 are positive numbers.

It is substituted into equation (5.7) like the matrix $\mathbf{A}$ shown in (3.9), obtaining expression (5.9).

$$\begin{bmatrix} -2h_{11}/\tau_1 & 0 & 0 & 0 \\ 0 & -2h_{22}/\tau_2 & 0 & 0 \\ 0 & 0 & -2h_{33}/\tau_3 & 0 \\ 0 & 0 & 0 & 0 \end{bmatrix} = \begin{bmatrix} -2/k_1 & 0 & 0 & 0 \\ 0 & -2/k_2 & 0 & 0 \\ 0 & 0 & -2/k_3 & 0 \\ 0 & 0 & 0 & 0 \end{bmatrix} \tag{5.9}$$

where h_{11}, h_{22}, h_{33}, and h_{44} are the elements of the correction matrix $\mathbf{H}$. Finding the values of the matrix $\mathbf{H}$ as indicated in (5.10), the element h_{44} is a free element, where all are positive constants.

$$h_{11} = \tau_1 k_1 \tag{5.10}$$
$$h_{22} = \tau_2 k_2$$
$$h_{33} = \tau_3 k_3$$

The selected Lyapunov function is (5.11):

$$V(\mathbf{e}_x) = \mathbf{e}_x^T \mathbf{H}^{-1} \mathbf{e}_x \tag{5.11}$$

Therefore, the derivative of the function is described as (5.12):

$$\dot{V}(\mathbf{e}_x) = \dot{\mathbf{e}}_x^T \mathbf{H}^{-1} \mathbf{e}_x + \mathbf{e}_x^T \mathbf{H}^{-1} \dot{\mathbf{e}}_x \tag{5.12}$$

Substituting equation (5.6) in (5.12) is posible to expressed as (5.13):

$$\begin{aligned} \dot{V}(\mathbf{e}_x) =& \mathbf{e}_x^T \mathbf{A}^T \mathbf{H}^{-1} \mathbf{e}_x + \mathbf{e}_x^T \mathbf{H}^{-1} \mathbf{A} \mathbf{e}_x + ... \\ & ... - \mathbf{e}_x^T \nabla h^T(\hat{\mathbf{x}}) \nabla h(\hat{\mathbf{x}}) \mathbf{H}^T \mathbf{H}^{-1} \mathbf{e}_x - \mathbf{e}_x^T \nabla h^T(\hat{\mathbf{x}}) \nabla h(\hat{\mathbf{x}}) \mathbf{H} \mathbf{H}^{-1} \mathbf{e}_x \end{aligned} \tag{5.13}$$

Using equation (5.7) and considering that the matrix $\mathbf{H}$ is diagonal and positive defined, we can ensure that $\mathbf{H} = \mathbf{H}^T$ and simplify equation (5.13) in (5.14).

$$\dot{V}(\mathbf{e}_x) = \mathbf{e}_x^T(-\mathbf{Q})\mathbf{e}_x - \mathbf{e}_x^T(2\nabla h^T(\hat{\mathbf{x}})\nabla h(\hat{\mathbf{x}}))\mathbf{e}_x = -\mathbf{e}_x^T(\mathbf{Q} + \nabla h^T(\hat{\mathbf{x}})\nabla h(\hat{\mathbf{x}}))\mathbf{e}_x \tag{5.14}$$

Where the matrix $\mathbf{Q} + \nabla h^T(\hat{\mathbf{x}})\nabla h(\hat{\mathbf{x}})$ is defined as (5.15).

$$\mathbf{Q} + \nabla h^T(\hat{\mathbf{x}})\nabla h(\hat{\mathbf{x}}) = 2 \begin{bmatrix} 1 + h_{11} & 1 & 1 & -\frac{\partial v_{OC}}{\partial v_{SOC}} \\ 1 & 1 + h_{22} & 1 & -\frac{\partial v_{OC}}{\partial v_{SOC}} \\ 1 & 1 & 1 + h_{33} & -\frac{\partial v_{OC}}{\partial v_{SOC}} \\ -\frac{\partial v_{OC}}{\partial v_{SOC}} & -\frac{\partial v_{OC}}{\partial v_{SOC}} & -\frac{\partial v_{OC}}{\partial v_{SOC}} & (\frac{\partial v_{OC}}{\partial v_{SOC}})^2 \end{bmatrix} \tag{5.15}$$

Given the matrix (5.15), it is necessary to guarantee that it is positive definite, so the Sylvester criterion is used [114], taking all the superior principal submatrices and calculating their determinants (Δ_1, Δ_2, Δ_3, and Δ_4) (5.16).

$$\begin{aligned}\Delta_1 &= 2(1+h_{11}) \\ \Delta_2 &= 4(h_{11}+h_{22}+h_{11}h_{22}) \\ \Delta_3 &= 8(h_{11}h_{22}+h_{11}h_{33}+h_{22}h_{33}+h_{11}h_{22}h_{33}) \\ \Delta_4 &= 16(h_{11}h_{22}h_{33}\frac{\partial v_{OC}}{\partial v_{SOC}})\end{aligned} \tag{5.16}$$

Considering that h_{11}, h_{22}, h_{33}, and h_{44} are positive and $\frac{\partial v_{OC}}{\partial v_{SOC}}$ is positive on the interval ($[0,1]$), it is known that the determinants of the principal submatrices are positive. Therefore $\dot{V}(\mathbf{e}_x)$ is negative definite, concluding in this way that the derivative of the error is asymptotically stable.

□

Corollary 4.2[Nonlinear condition.] The nonlinear function $h(\mathbf{x})$ and its derivative $\nabla h(\mathbf{x})$ are Lipschitz.

Proof. $h(\mathbf{x})$ and $\nabla h(\mathbf{x})$ are polynomial functions, hence is of interest to demonstrate that they are locally Lipschitz using the inequality (5.17) [115].

$$\left\| \frac{\partial h(\mathbf{x})}{\partial \mathbf{x}} \right\| \leq L \quad \forall \mathbf{x} \in \mathbb{R} \tag{5.17}$$

Indicating that the Lipschitz constant should be higher than any of the jacobians supremes in the closed interval where the SOC have physical meaning ($[0,1]$).

For this case, the partial derivative of the function $h(\mathbf{x})$ is nonlinear only in its partial derivative to v_{SOC}, while the remainder of the jacobian is 0, so it will be validated for element $\frac{\partial h(\mathbf{x})}{\partial v_{SOC}}$, resulting in the polynomial equation(5.18).

$$\frac{\partial h(\mathbf{x})}{\partial v_{SOC}} = 11.785(v_{SOC})^4 - 23.852(v_{SOC})^3 + 16.872(v_{SOC})^2 - 4.884(v_{SOC}) + 0.6952 \tag{5.18}$$

Since the resulting function is polynomial and is bounded to a closed interval ($[0, 1]$), the Lipschits constant must be greater than any value of the function in this interval, to do this the supreme of the bounded function must be found. In this case we will use the derivative of the function (5.18) with respect to v_{SOC} which is described as (5.19).

$$\frac{\partial^2 h(\mathbf{x})}{\partial v_{SOC}^2} = 47.140(v_{SOC})^3 - 71.556(v_{SOC})^2 + 33.744(v_{SOC}) - 4.884 \tag{5.19}$$

This expression is equal to zero and the solutions to said equation are obtained, including the boundaries of the interval and evaluating said values in function (5.18), obtaining the results of Table 5.1.

Table 5.1: Values of the supremes of the Jacobian of the nonlinear function (5.19).

v_{SOC} (V)	$\frac{\partial h(\mathbf{x})}{\partial v_{SOC}}$ (V)
0.0000	0.0000
0.2823	0.1992
0.4965	0.2269
0.7390	0.1886
1.0000	0.6162

Allowing us to conclude that there exists a contant $L \geq 0.6162$ proving that the nonlinear function $h(\mathbf{x})$ is lipschitz. $\therefore \exists L \colon \left\| \frac{\partial h(\mathbf{x})}{\partial \mathbf{x}} \right\| \leq L \quad \forall \mathbf{x} \in \mathbb{X}$ □

According to the previous verifications, the proposed observer is valid for the battery used, where the elements of the correction matrix have the restriction to be positive. For this case, the values of $h_{11} = 0.6$, $h_{22} = 0.6$, $h_{33} = 0.6$, and $h_{44} = 0.2$ were selected, respecting the above corollaries, these gains allow us to position the observer slightly faster than the model system used.

5.3 Experimental validation

After establishing the EEC model, highlighting the potential drawbacks of Coulomb Counting, and designing the nonlinear observer analytically, the effectiveness of the

proposed approach through experiments will be shown. This will be done by comparing the Columb Counting method with the nonlinear observer.

The first validation is the observer performance in deteriorating conditions and compare them with the model using only Coulom Counting method; this is shown in Figure 5.2, where the battery voltage after 200 aging cycles is shown in Figure 5.2 (a), showing how the Coulom Counting method diverges from the measurements; however, the observer maintains values close to what was measured. In the same way, Figure 5.2 (b) shows how the use of Coulomb Counting presents problems in estimating the SOC by indicating that the battery is at 100% SOC when, in reality, it only reaches 80%. Upon discharge, the Coulomb Counting estimates having 30% SOC available when, in fact, it has already reached 0%, giving rise to periods of over-discharge. This can be confirmed by observing how in Fig 5.2 (a), the voltage at the terminals does not reach 2.24 V due to retention loss; likewise, when discharging the battery, a trend of accelerated voltage loss is shown with respect to Fig 3.10.

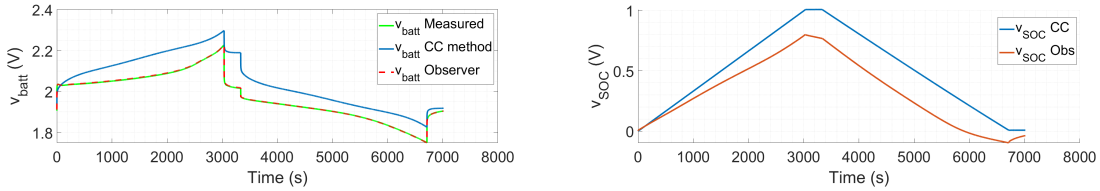

(a) (b)

Figure 5.2: Comparison of battery measurements and simulated results for the battery nonlinear observer model and traditional Coulomb Counting method at 200 aging cycles, (a) Battery voltage measured, simulated and observed at 200 cycles. (b) SOC estimated by coulomb counting method and a nonlinear observer at 200 cycles.

Although Coulomb Counting delivers results close to what was expected, it exposes the battery to possible overcharge or over-discharge conditions by accelerating its aging, a problem that the observer corrects.

Another point to evaluate is the inclusion of the variations in the dynamics due to parametric changes, which are produced by battery aging; the battery state variables corresponding to the voltage in the *RC* arrangements, plotting the battery without aging and the battery with 200 aging cycles, the results are shown in Figure 5.3, showing the charge/discharge test previously described in Chapter 2, the blue lines correspond to the model using Coulomb Counting and the red lines correspond to the observer.

Note that the model's response with Coulomb Counting presents little changes even when evaluating batteries with different aging states. In contrast, the observer in Figure 5.3(a), 5.3(b), and 5.3(c) shows minor variations throughout the charge and discharge, representing the changes due to SOC discussed above. In the same way, Figure 5.3(d), 5.3(e), and 5.3(f) show how the observer variations are more pronounced

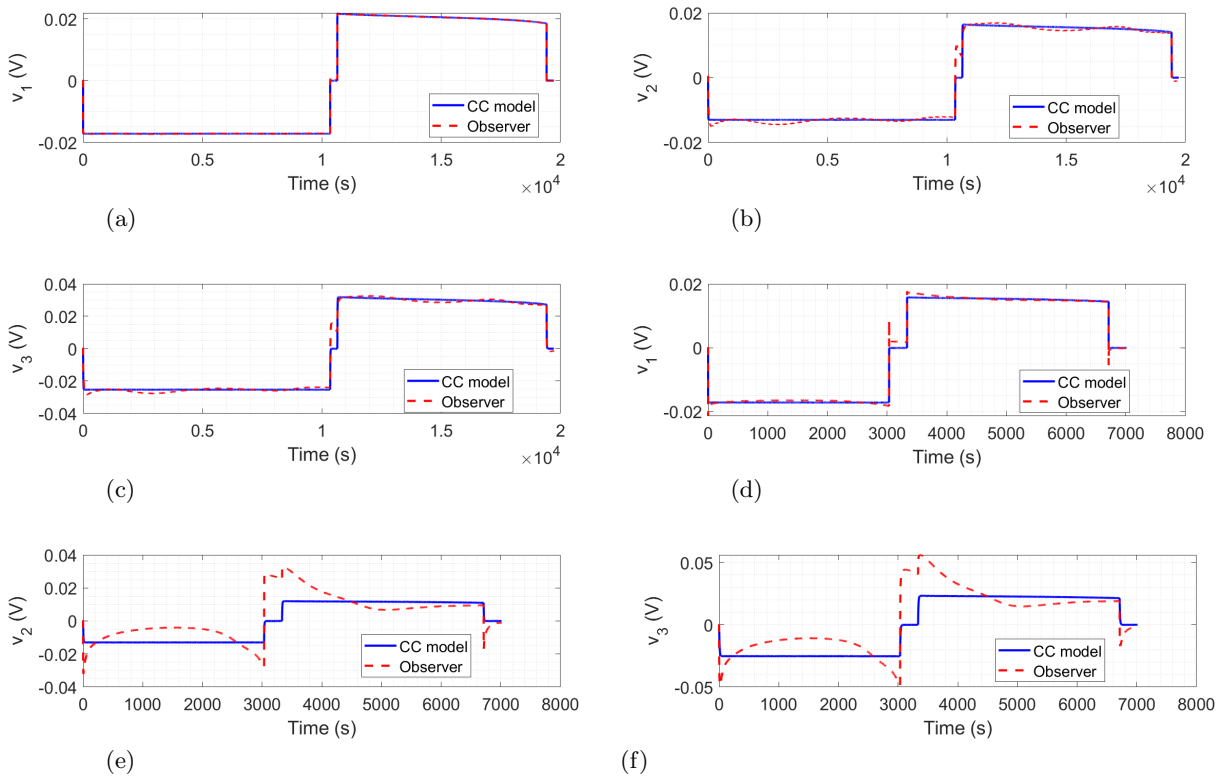

Figure 5.3: Response of the state variables at the beginning and end of useful life comparing the Coulomb Counting model response and the observer response. (a), (b), and (c) Voltage in arrangement R_1C_1, R_2C_2, and R_3C_3 for a battery without aging, respectively. (d), (e), and (f) Voltage in arrangement R_1C_1, R_2C_2, and R_3C_3 for a battery with 200 aging cycles, respectively.

than the previous ones due to parametric changes due to aging. The results shown by the observer are consistent with what is described in the literature and prove that the observer includes the parametric variations in a single model.

According to the previous results, and using the batteries tested in Chapter 3, different batteries with different aging points were measured in discharge cycles, extracting from the model the behavior of the voltage in the different states, The batteries are evaluated with 0, 25, 50, 100, 150 and 200 life cycles, these evaluation points were selected so that variations due to aging were evident, on the contrary, if the points to be evaluated are close to each other the changes will not be noticed, according to the literature [68] the changes in continuous cycles are minimal at the level of considering the same evaluation point, as proof Figure 5.4 shows the first three charge and discharge cycles of a battery.

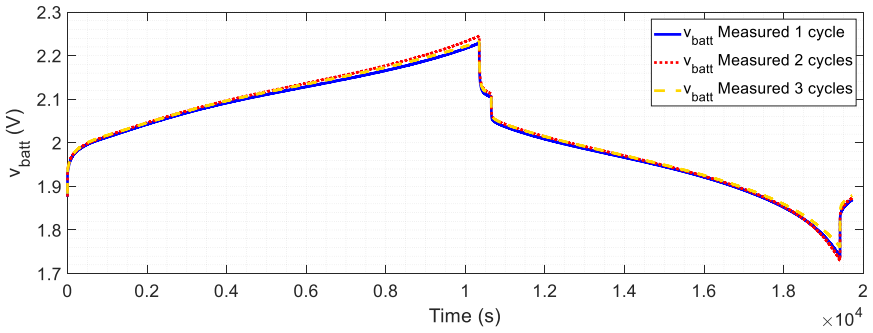

Figure 5.4: Battery voltage measurements from one battery in three consecutive charge/discharge cycles.

Giving the results shown in Figure 5.5. In this way, the evolution of the system's dynamic response can be observed, approximating the ideal aging trend. At the end of each plot, the voltages have an abrupt change in their value; this is because at that moment, the charging or discharging process ended, as appropriate, and the batteries are disconnected, leaving them in an open circuit, which produces this abrupt change. This behavior is maintained in the rest of the figures and was graphed to illustrate the end of the process to be analyzed.

Figure 5.5(a), 5.5(b), and 5.5(c) correspond to the evolution of state variables during the charging process. The first thing that stands out is that the time it takes to complete the charge is increasingly shorter; this is the effect of the loss of capacity. This phenomenon also occurs during discharge. Typically, aging measured through SOH uses this phenomenon since it presents the most noticeable change. However, subtle changes are also shown in the transient behavior, where v_3 has more obvious differences because it represents the most significant time constant. The changes of greatest interest are the initial overshot, which, although subtle, increases as the battery ages, the transient movements, which are smooth at the beginning and, as it ages, begin to be abrupt; this is related to the decrease in the time constants, and finally, the response of the state variables when approaching the beginning and end of the SOC is faster, this is because in those regions where the nonlinear response settles.

On the other hand, Figure 5.5(d), 5.5(e), and 5.5(f) correspond to the voltages of the state variables in the discharge process, where the effects of the loss of capacity are evident just as mentioned above. The changes during discharge are more noticeable than during charging because, during discharge, the electrochemical processes follow their natural reaction tendency; meanwhile, when charging, an external source is applied that causes the processes to be reversed [4]. One of the aspects to highlight is that as the battery ages, the voltage amplitude is lower, except for the initial overshoots; this is best manifested in v_1 since the arrangement with the lowest capacity makes the changes in amplitude have greater visibility. At the same time, an initial overshoot

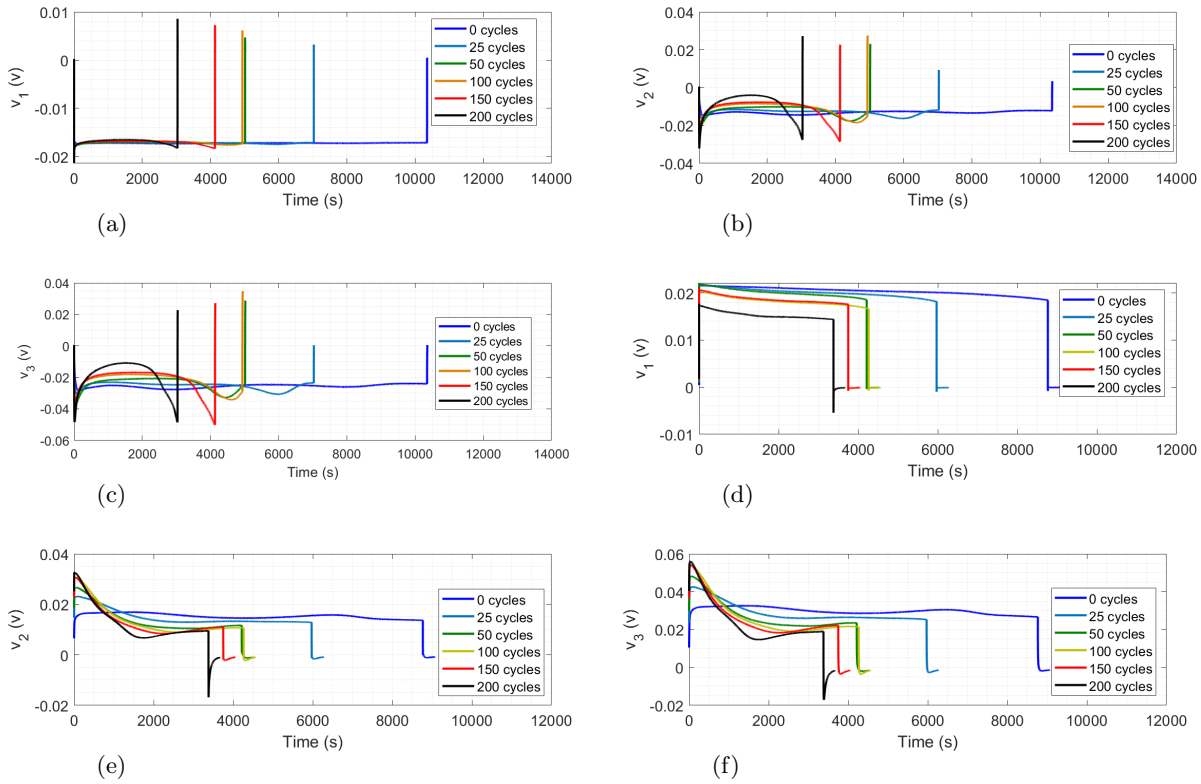

Figure 5.5: Response of the state variables during the charge and discharge process throughout the useful life of the battery. (a), (b), and (c) Voltage in array R_1C_1, R_2C_2, and R_3C_3 when charging, respectively. (d), (e), and (f) Voltage in array R_1C_1, R_2C_2, and R_3C_3 when discharging, respectively.

appears in the v_2 and v_3 graphs, which is directly related to the increase in internal resistance previously mentioned. During discharge transients become abrupt as the battery ages, indicating decreasing time constants.

For the aging experiments described above, the evolution of SOH shown in Figure 5.6 corresponds where it can be seen that the batteries are approaching 80% SOH, which indicates the end of useful life for most applications. This indicates that the batteries are about to be unusable for the application for which they were designed. This does not mean that 80% of the battery's life is wasted, but when the percentage falls below this, its performance deteriorates to levels where it is impossible to guarantee its operation [4].

It is important to note that all the graphs throughout aging have the same behavior; it is evident that the parametric changes deform the response, but the trend remains monotonous throughout the useful life. It also becomes clear that as age increases,

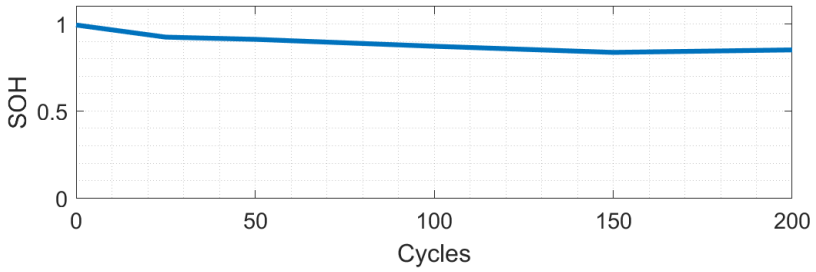

Figure 5.6: Battery SOH evolution through 200 aging cycles under manufacturer recommended conditions.

resistance values increases, observable in the plotted overshoots, and the time constants decrease, visible in the abrupt transients, validating that the use of the observer shows the changes produced by the SOH and the parametric variation.

With the evidence previously presented, the modeling of the battery is postulated according to equation (5.20), where aging is treated as a multiplicative terms, They are considered multiplicative terms because these terms multiply the vector of states and/or the input of the system [116], modifying the parameters of the model, where said multiplicative terms depend on aging.

$$\begin{aligned} \dot{\mathbf{x}} &= (\mathbf{A} + \Delta\mathbf{A}_F)\mathbf{x} + (\mathbf{B} + \Delta\mathbf{B}_F)u \\ y &= h(\mathbf{x}) + (\mathbf{D} + \Delta\mathbf{D}_F)u \end{aligned} \tag{5.20}$$

where $\mathbf{x} \in \mathbb{R}^4$, $u \in \mathbb{R}$, $i \in \mathbb{R}$, and the matrices $\Delta\mathbf{A}_F$, $\Delta\mathbf{B}_F$, $\Delta\mathbf{D}_F$ represent the changes in the system parameters due to the advance in the SOH, described in the form (5.21).

$$(\mathbf{A} + \Delta\mathbf{A}_F) = \begin{bmatrix} -\frac{1}{\tau_A} + \frac{\Delta\tau_A}{\tau_A(\tau_A+\Delta\tau_A)} & 0 & 0 & 0 \\ 0 & -\frac{1}{\tau_B} + \frac{\Delta\tau_B}{\tau_B(\tau_B+\Delta\tau_B)} & 0 & 0 \\ 0 & 0 & -\frac{1}{\tau_C} + \frac{\Delta\tau_C}{\tau_C(\tau_C+\Delta\tau_C)} & 0 \\ 0 & 0 & 0 & 0 \end{bmatrix}; \tag{5.21}$$

$$(\mathbf{B} + \Delta\mathbf{B}_F) = \begin{bmatrix} \frac{1}{C_1} + \frac{\Delta C_1}{C_1(C_1+\Delta C_1)} \\ \frac{1}{C_2} + \frac{\Delta C_2}{C_2(C_2+\Delta C_2)} \\ \frac{1}{C_3} + \frac{\Delta C_3}{C_3(C_3+\Delta C_3)} \\ -\frac{1}{C_{usable}} \end{bmatrix};$$

$$(\mathbf{D} + \Delta\mathbf{D}_F) = \begin{bmatrix} -R_0 + \Delta R_0 \end{bmatrix};$$

where R_0, C_1, C_2, C_3, τ_A, τ_B, and τ_C constitute a time-invariant model and only depend on the SOC, while ΔR_0, ΔC_1, ΔC_2, ΔC_3, $\Delta\tau_A$, $\Delta\tau_B$, and $\Delta\tau_C$ depend on

the aging, thus defining the effect of aging as an multiplicative element of parametric modification.

To obtain the additive terms of matrix $\Delta\mathbf{A}_F$ and $\Delta\mathbf{B}_F$, it was considered that the changes would modify the term found in the denominator and it is sought to separate said term into the sum of two fractions where one of them is the original term of matrix $\mathbf{A}$, as shown in equation (5.22), where the term a_{11} of matrix $\Delta\mathbf{A}_F$ will be exemplified; however, the procedure is the same for all terms.

$$\frac{-1}{\tau_A + \Delta\tau_A} = -\frac{1}{\tau_A} + a_{11} \tag{5.22}$$

To obtain the searched value, the term a_{11} is cleared as shown in equation (5.23), this same procedure is repeated for the rest of the aforementioned terms.

$$a_{11} = \frac{-1}{\tau_A + \Delta\tau_A} + \frac{1}{\tau_A} = \frac{\Delta\tau_A}{\tau_A(\tau_A + \Delta\tau_A)} \tag{5.23}$$

5.4 Overcharge and Over-discharge test

For the proposed model (5.21) to make sense and be used in future applications, it is necessary to know the expected behavior under conditions of misuse, such as overcharge and over-discharge, describing the resulting trends of abnormal behavior and how these would manifest in the model.

For this, an aging profile was developed based on the one shown in Figure 3.19, where for the overcharge condition, the batteries were charged to a voltage of 2.4V, which exceeds the limit suggested by the manufacturer by a 5%. In contrast, during discharge, the batteries were required to deliver current until they reached 1.3V, exceeding the proposed lower limit in a 5%, 12 batteries were aged in overcharge conditions with discharge at normal levels, batteries $B1\_OC$ to $B12\_OC$, and 12 batteries in over-discharge conditions with normal charge levels, batteries $B1\_OD$ to $B12\_OD$, in both cases 3 batteries were removed every 50 cycles, to conserve batteries at different aging points, for this test the circuit shown in figure 5.7 was used, in where 2 sources were used, one for the overcharge test (DC Source OC) and the other for the over-discharge test (DC Source OD), in addition to 2 different resistive load, R_OC and R_OD for overcharge and over-discharge test, respectively, both circuits were controlled and mediated by a RTAC SEL-2240 industrial computer equipment.

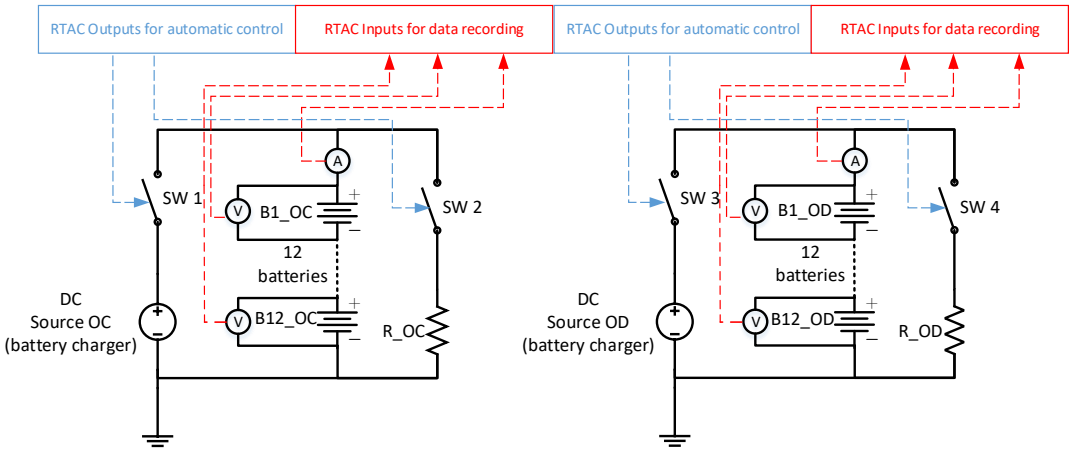

Figure 5.7: Battery Circuit Schematic for overcharge and over-discharge test.

With these tests, it is possible to know the effectiveness of the proposed observer, finding that for both overcharge and over-discharge, the observer continues giving best results, even taking the battery beyond the voltage limits. Fig 5.8(a) shows the voltage measured in the overcharge test, the measured voltage (green line), the observer's estimation (red dashed line), and the Coulomb Counting method estimation (blue line), evidencing how the observer has better tracking while the Coulomb Counting model tends to diverge. Additionally, Fig 5.8(b) shows the estimate of v_{SOC}, making it evident that the battery reached 100% before the Coulomb Counting model registered it. In the same way, Figure 5.8(c) shows the voltage and how the observer performs well beyond the limits in the discharge. In addition, Figure 5.8(d) shows how Coulomb Counting cannot detect the over-discharge at which they subdued.

From these new tests, batteries with 200 aging cycles were taken, and the voltages of the state variables were compared against the voltages of Figure 5.5. In this way, it is possible to compare the dynamic behavior of an aging battery in conditions of misuse and the behavior of an aging battery according to factory specifications.

First, the batteries subjected to aging with overcharge levels were analyzed. Finding that the evolution of SOH under overcharge (SOH OC) tends to grow above 100%, as shown in Figure 5.9 with a red line, and compared to the evolution of SOH under normal conditions (SOH NC) by the manufacturer, in the blue line, does not show superior aging.

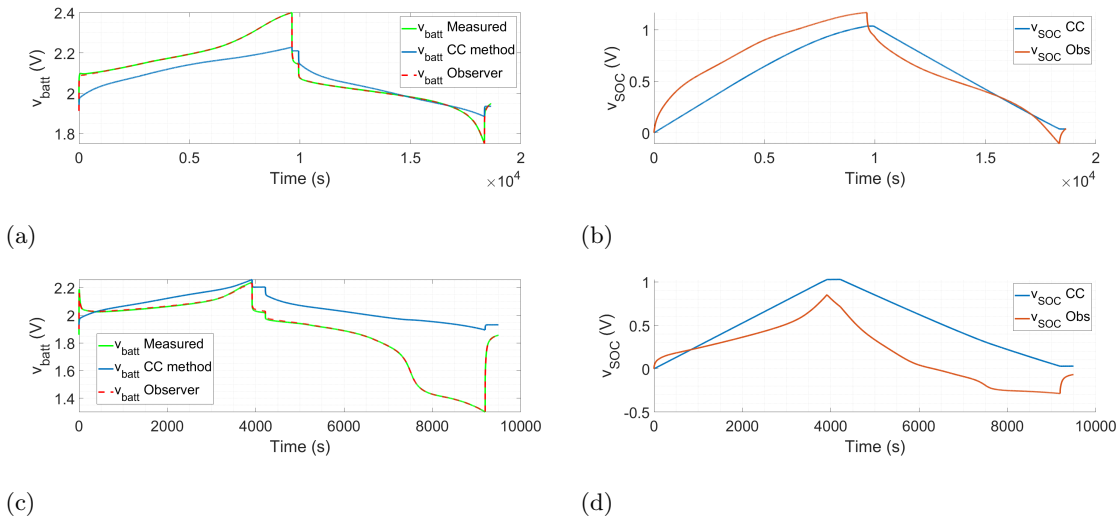

Figure 5.8: Comparison of battery measurements and simulated results for the battery nonlinear observer model and traditional Coulomb Counting model at 200 aging cycles in overcharge and over-discharge. (a) Battery voltage measured, simulated and observed at 200 cycles at overcharge. (b) SOC estimated by coulomb counting method and a nonlinear observer at 200 cycles at overcharge. (c) Battery voltage measured, simulated and observed at 200 cycles at over-discharge. (d) SOC estimated by coulomb counting method and a nonlinear observer at 200 cycles at over-discharge.

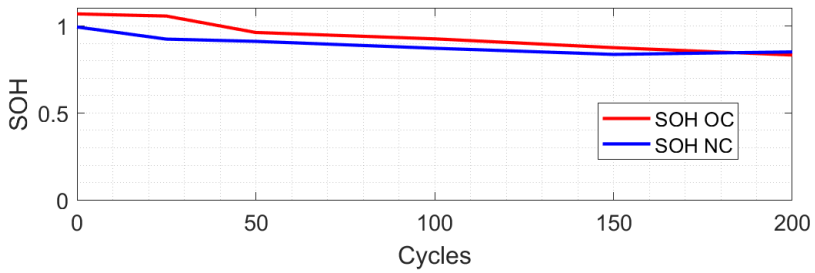

Figure 5.9: Comparison between battery SOH evolution through 200 aging cycles under manufacturer recommended conditions and 200 aging cycles under overcharge conditions.

These results make it possible to infer a difference comparing the SOH. However, these are subtle and could pass as a battery subjected to normal discharge. This inference the state variables of the proposed observer can be seen by analyzing Figure 5.10, shows the charging and discharging behaviour of the battery at 200 cycles of

aging under overcharge conditions in the red line, with the blue line the reaction of a battery without aging, and in dashed blue line the reaction of a battery with 200 aging cycles according to the manufacturer's specifications. It is notable that the battery overcharged for 200 cycles has a greater capacity than the aged batteries under normal conditions, this is evident since the red line ends much later than the dashed blue line. However, this is because the battery is being forced to stores more than 100% SOC, so its capacity is greater, but its response during this time is noticeably affected.

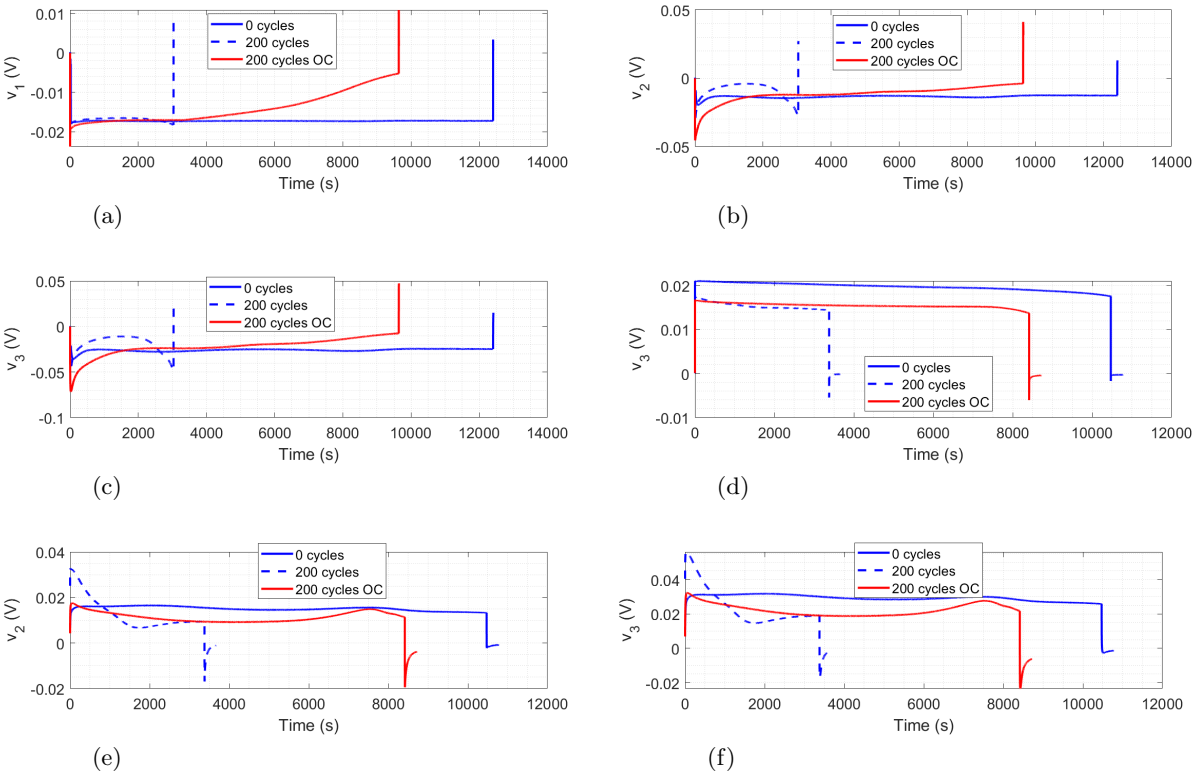

Figure 5.10: Overcharge test resulting response of the state variables, comparing test results with normal condition aging limits. (a) voltage in arrangement R_1C_1 when charging, (b) voltage in arrangement R_2C_2 when charging, (c) , voltage in arrangement R_3C_3 when charging, (d) voltage in arrangement R_1C_1 when discharging, (e) voltage in arrangement R_2C_2 when discharging, and (f) voltage in arrangement R_3C_3 when discharging.

The Figures. 5.10(a), 5.10(b), and 5.10(c) show the response of the state variables during the charge, where essential differences can be observed; first, there is an overshoot greater than the expected behavior in the three graphs, becoming evident in v_3. In the same way, the amplitude of the graphs before finishing the charge decreases significantly, which is evident in v_1. On the other hand, Figure 5.10(d), 5.10(e), and

5.10(f) show the response in the discharge; it is possible to find a behavior outside of what was expected. In this case, contrary to the load graphs, it is not shown on impulse. On the contrary, the charts show a smooth behavior, which indicates that the variations in the time constants have been smaller than those obtained with normal aging, which becomes relevant in the first moments after the change in current. This allows us to conclude that changes in the smallest time constant and the elements of the instantaneous response will demonstrate actual aging due to overcharge.

In addition, the same analysis was carried out on over-discharge aged batteries. Figure 5.11 shows with a blue line the evolution of the SOH of the batteries aged under normal conditions (SOH CN), while the green line shows the behavior of the SOH of the aged batteries under over-discharge conditions (SOH OD).

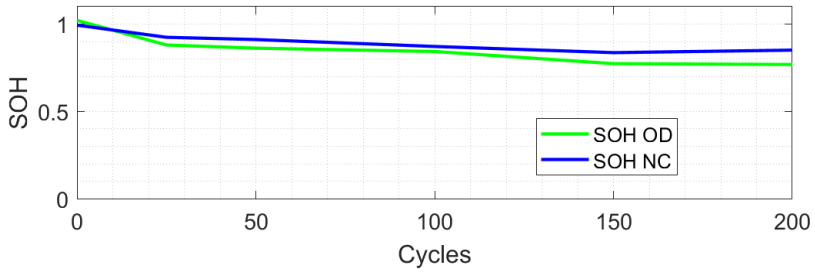

Figure 5.11: Comparison between battery SOH evolution through 200 aging cycles under manufacturer recommended conditions and 200 aging cycles under over-discharge conditions.

In this case, the SOH advances faster when the battery is subjected to over-discharge conditions, decaying 10% more than the normally aged battery, demonstrating that the SOH can detect this misuse.

Complementary to the SOH, the responses of the observer's state variables were analyzed, obtaining Figure 5.12, where the reaction of a battery without aging is shown with a blue line, and with a blue dashed line, the response of a battery with 200 aging cycles in conditions recommended by the manufacturer and in green line the reaction of a battery with 200 aging cycles in over-discharge conditions. As in the case of batteries exposed to overcharge, batteries exposed to over-discharge show a capacity greater than expected for a battery with 200 aging cycles. However, by requiring the battery to work below 0% at loading appears to have greater capacity, however the rest of the behavior of the graphs shows irregularities due to misuse.

Figure 5.12(a), 5.12(b), and 5.12(c) show the results of this test during charging, where it can be noted that the battery response has a behavior similar to the proposed limits, differentiated by an initial overshoot with a very short duration. On the other hand, Figure 5.12(d), 5.12(e), and 5.12(f) show the response to the discharge; in this case, the response is similar to the proposed limits both in the instantaneous response

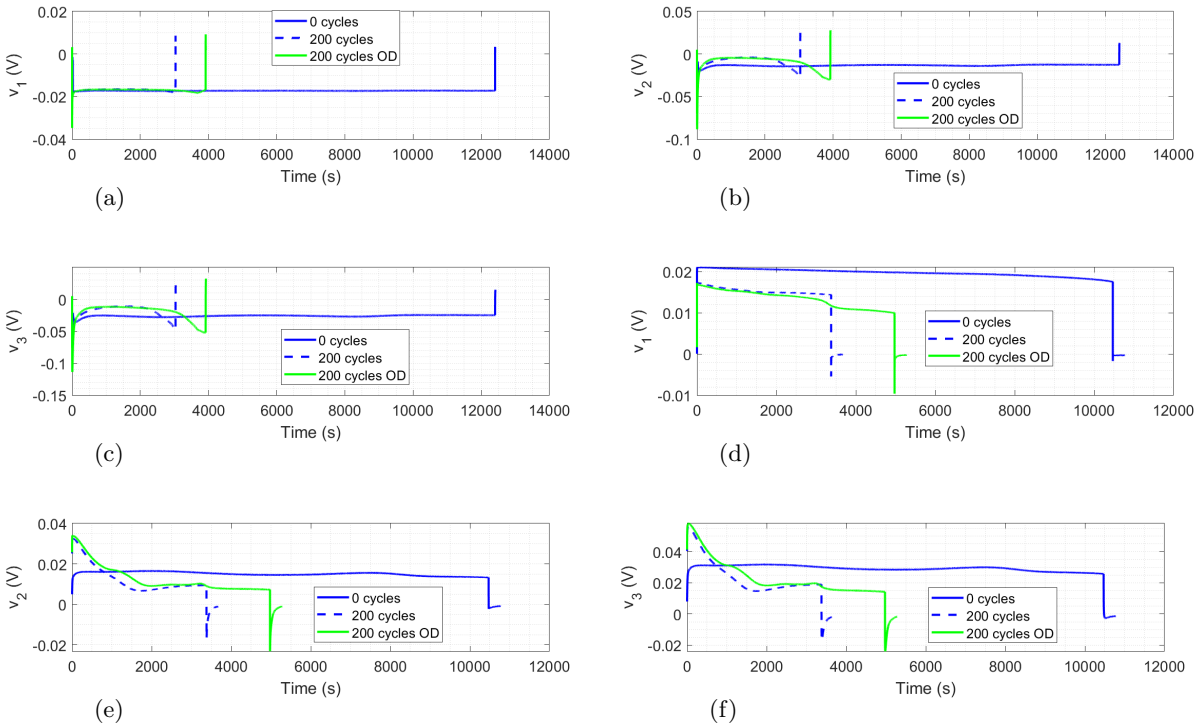

Figure 5.12: Over-discharge test resulting response of the state variables, comparing test results with normal condition aging limits. (a) Voltage in arrangement R_1C_1 when charging, (b) voltage in arrangement R_2C_2 when charging, (c) Voltage in arrangement R_3C_3 when charging, (d) voltage in arrangement R_1C_1 when discharging, (e) voltage in arrangement R_2C_2 when discharging, and (f) voltage in arrangement R_3C_3 when discharging.

and in the transient of the first moments. However, after the first moments, the behavior of the transient is more abrupt than that of the proposed limits. In this way, it is possible to conclude that over-discharge is associated with the largest instantaneous changes and time constants.

It is possible to conclude how the extraction of additional information can detect aging due to misuse in greater detail than the SOH, where in cases of aging due to overcharge, it does not detect the correct level of aging. At the same time, the observed states show signs of aging. Likewise, it is possible to associate the responses of the conditions of misuse with time variables.

- Both the effects of overcharge and over-discharge modify the instantaneous response, which is directly related to the loss of active material. By rapidly wearing out the battery, the material is forced to lose effectiveness before the expected time.

- The overcharge conditions are strongly reflected in the reactions with a lower time constant, being associated with the effects of the electrical double layer and corrosion.
- Over-discharge conditions have a longer response time, making it possible to associate them with diffusion effects and hard sulfation.

With these new conclusions, it is possible to give meaning to the multiplicative faults of the proposed model (5.20), which do not provide information on the detection of aging; this does not eliminate or invalidate the detection of SOH; on the contrary, it provides additional information to improve the detection.

- ΔR_0 corresponds to instantaneous changes graphically; this is reflected in the overshoots in Figure 5.5, both in charging and discharging, increasing progressively with aging; in the same way, it appears more aggressively when overcharge and over-discharge, particularly when charging the battery.
- $\Delta\tau_A$ and ΔC_1 correspond to the changes present in the smallest time constants; the values are modified in all cases; however, it has a relevant change in the overcharge Figure 5.10, since, during the charge, it is in these elements where the drop in The amplitude has a noticeable change in proportion to its expected nominal values. Likewise, during discharge, this time constant dampens the first moments in conjunction with the absence of the expected overshoot.
- $\Delta\tau_B$ and ΔC_2 It corresponds to the reactions with the middle time constant; in this case, the variations of these elements are progressive with respect to aging, and although it showed changes between normal aging and aging due to misuse, it does not reveal such compelling information, without However, together with the rest of the variations, it allows us to validate that they are changes due to misuse or errors in the estimation.
- $\Delta\tau_C$ and ΔC_3 correspond to the variations of the slower time constants, and it is these changes that mainly contribute to the voltage oscillations during charging and discharging. These effects are present during aging under normal conditions and are accentuated during aging due to over-discharge, and on the contrary, are attenuated during aging due to overcharge.

Chapter 6

Conclusions

In contemporary electrical energy systems, batteries serve as indispensable energy storage components, particularly in the realm of electric vehicle propulsion. While extensive research has been conducted on battery modeling from both electrochemical and electrical perspectives, a comprehensive correlation between mechanistic and EEC models to elucidate internal aging phenomena remains unexplored. The main contributions are listed below and detailed later.

- A correlation was established between a mechanistic model and an EEC model, redefining the physical meaning of the parameters of the EEC model, facilitating the interpretation of chemical reactions from this model.
- A state space model was proposed which represents the parametric changes of the model due to aging as multiplicative variations, where these variations were associated with electrochemical reactions and at the same time with aging mechanisms.

This study addresses this gap by investigating lead-acid batteries, with the understanding that the proposed methodology can be extended to other battery chemistries that involve adsorbed intermediates. Through rigorous experimentation employing EIS, a robust correlation between EEC model time constants and underlying electrochemical reactions was established.

The findings reveal that the first RC parallel circuit component corresponds to charge transfer and lead adsorption on the negative electrode within the 1.48 Hz to 10 kHz frequency range. The second RC component is associated with oxygen release, water formation, and lead sulfate generation at the positive electrode in the 0.5 Hz to 1.48 Hz range. Finally, the third RC component relates to lead sulfate generation and electrolyte diffusion processes within the 0.01 Hz to 0.5 Hz frequency band.

Based on the analysis and results obtained, the importance of estimating aging is reinforced, where the SOH allows monitoring the useful life of the battery. Therefore, the proposed model seeks to contribute information that details how aging is occurring. This additional information can be observed in greater detail in the experiments carried

out during the overcharge tests, where the SOH has changed with respect to aging under normal conditions; however, at first glance, it is impossible to make a significant or forceful distinction between their results. However, the proposal of this work shows indicators with a clear difference between both cases. The case of over-discharge is differentiable from the SOH by showing a greater drop than expected; even so, the proposal of this work allows us to identify how the variations in the instantaneous reactions and in the slow time constants predominantly increase.

An analysis is made of the SOC estimation using the Coulomb Counting method and its limitations when taking the battery to the end of its useful life and to conditions of misuse, where the Coulomb Counting puts the battery at risk, taking it to overcharging and over-discharging due to the divergence of results. On the other hand, the observer, has a better estimation of the battery SOC, promptly detecting the risks that the Coulomb Counting overlooks. The results obtained in this work are a small sample of the range of possibilities that were explored, leaving evidence of possible future work such as a aging diagnosis algorithm using the results obtained, as well as approaching the problem from the parametric variation once the physical meaning of these results is known.

6.1 Future work

One of the main issues to be addressed in the future is the incorporation of a thermal model, since the entire development of this work was handled at room temperature. There are thermal models that can be represented as electrical circuits, which would allow us to maintain a model uniform, providing additional information so it would be necessary to analyze the performance of the reactions used in this work under different temperature conditions, preferably at 10°, 40° and 65° Celsius, which is what is recommended for battery testing.

In the same way, it is possible to explore different EEC models. Following the methodology proposed in this work, it is necessary to associate the elements of the proposed circuit with a group of frequencies, ideally measured, thus representing the impedance response in said spectrum. However, to associate these terms with a reaction outside the limits presented in this work, it is necessary to carry out an electrochemical analysis or have sufficient information to give it a physical meaning. As an example, in various works inductive elements are added to the model used, within the proposed methodology it is necessary to make measurements in frequency ranges higher than those shown and analyze their behavior and association with chemical reactions.

Likewise, it is important to be able to transfer the work developed here to other battery technologies. This process is possible. To do this, one of the following two paths can be followed: If the battery works through a redox reaction, the proposed modeling procedure must be followed. In chapter 4, it is evident that the reactions will not be the same, since each battery produces its own intermediates and final products, however, the steps to follow are the same, it is also important that the circuit used in

this work is designed to lead-acid batteries and although it is possible to use it in other technologies, it is necessary to check its correct adjustment by determining the number of RC arrangements necessary following the same arrangement; in case of a battery technology that does not work through a redox reaction, lithium ions for example, the procedure to follow is to find the P2D model instead of the mechanistic model, these models follow similar steps providing a transfer function where it is possible to find the internal reaction rates of the batteries.

Bibliography

[1] N. M. Hammad, "Vehicle valve regulated lead acid battery modeling and fault diagnosis," tech. rep., SAE Technical Paper, 2010. xxi, 2, 38, 39, 49, 71, 87

[2] X. Sun, J. Ji, B. Ren, C. Xie, and D. Yan, "Adaptive forgetting factor recursive least square algorithm for online identification of equivalent circuit model parameters of a lithium-ion battery," Energies, vol. 12, no. 12, p. 2242, 2019. xxi, 27, 40, 41, 52, 56

[3] P. Ruetschi, "Aging mechanisms and service life of lead–acid batteries," Journal of power sources, vol. 127, no. 1-2, pp. 33–44, 2004. xxii, 48, 49

[4] G. L. Plett, Battery management systems, Volume I: Battery modeling, vol. 1. Artech House, 2015. xxv, 1, 9, 10, 11, 13, 24, 25, 26, 29, 90, 98, 99

[5] J. A. Sanguesa, V. Torres-Sanz, P. Garrido, F. J. Martinez, and J. M. Marquez-Barja, "A review on electric vehicles: Technologies and challenges," Smart Cities, vol. 4, no. 1, pp. 372–404, 2021. 1

[6] Z. Pan, N. V. Quynh, Z. M. Ali, S. Dadfar, and T. Kashiwagi, "Enhancement of maximum power point tracking technique based on pv-battery system using hybrid bat algorithm and fuzzy controller," Journal of Cleaner Production, vol. 274, p. 123719, 2020. 1

[7] S. Maddukuri, D. Malka, M. S. Chae, Y. Elias, S. Luski, and D. Aurbach, "On the challenge of large energy storage by electrochemical devices," Electrochimica Acta, vol. 354, p. 136771, 2020. 1

[8] IEEE, "Standard for qualification of class 1e static battery chargers, inverters, and uninterruptible power supply systems for nuclear power generating stations," IEEE Std. 650-2017, February 2018. 1

[9] S. Sharma, A. K. Panwar, and M. Tripathi, "Storage technologies for electric vehicles," Journal of traffic and transportation engineering (english edition), vol. 7, no. 3, pp. 340–361, 2020. 1

[10] A. El Fathi and A. Outzourhit, "Technico-economic assessment of a lead-acid battery bank for standalone photovoltaic power plant," Journal of Energy Storage, vol. 19, pp. 185–191, 2018. 1

[11] S. N. Haider, Q. Zhao, and X. Li, "Data driven battery anomaly detection based on shape based clustering for the data centers class," Journal of Energy Storage, vol. 29, p. 101479, 2020. 1

[12] G. L. Plett, Battery management systems, Volume II: Equivalent-circuit methods, vol. 2. Artech House, 2015. 1, 4, 13, 16, 17, 18, 19, 23, 27, 72, 90

[13] C. S. Lai, G. Locatelli, A. Pimm, X. Wu, and L. L. Lai, "A review on long-term electrical power system modeling with energy storage," Journal of Cleaner Production, vol. 280, p. 124298, 2021. 1

[14] G. J. May, A. Davidson, and B. Monahov, "Lead batteries for utility energy storage: A review," Journal of energy storage, vol. 15, pp. 145–157, 2018. 1

[15] Y. Yu, J. Mao, and X. Chen, "Comparative analysis of internal and external characteristics of lead-acid battery and lithium-ion battery systems based on composite flow analysis," Science of The Total Environment, vol. 746, p. 140763, 2020. 1

[16] R. Ahuja, A. Blomqvist, P. Larsson, P. Pyykkö, and P. Zaleski-Ejgierd, "Relativity and the lead-acid battery," Physical Review Letters, vol. 106, no. 1, p. 018301, 2011. 1

[17] S. C. Levy and P. Bro, Battery hazards and accident prevention. Springer Science & Business Media, 1994. 1

[18] D. A. J. Rand, L. Holden, G. May, R. Newnham, and K. Peters, "Valve-regulated lead/acid batteries," Journal of Power Sources, vol. 59, no. 1-2, pp. 191–197, 1996. 1, 2

[19] S.-C. Huang, K.-H. Tseng, J.-W. Liang, C.-L. Chang, and M. G. Pecht, "An online soc and soh estimation model for lithium-ion batteries," Energies, vol. 10, no. 4, p. 512, 2017. 1

[20] S. Sun, J.-z. Sun, Z.-l. Yang, Z.-y. Zhou, and Y.-y. Ding, "Prediction of battery charging process based on aggregation neural network," The Journal of Engineering, vol. 2022, no. 10, pp. 968–977, 2022. 1, 3

[21] W. Liu, Y. Xu, X. Feng, and Y. Wang, "Optimal fuzzy logic control of energy storage systems for V/f support in distribution networks considering battery degradation," International Journal of Electrical Power & Energy Systems, vol. 139, p. 107867, 2022. 1, 3

[22] G. L. Plett, "Extended kalman filtering for battery management systems of LiPB-based hev battery packs: Part 3. state and parameter estimation," Journal of Power sources, vol. 134, no. 2, pp. 277–292, 2004. 1, 3

[23] J. Olarte, J. Martínez de Ilarduya, E. Zulueta, R. Ferret, E. Kurt, and J. M. Lopez-Guede, "High temperature vlra lead acid battery soh characterization based on the evolution of open circuit voltage at different states of charge," JOM, vol. 73, no. 5, pp. 1251–1260, 2021. 1, 2

[24] R. Yahmadi, K. Brik, and F. b. Ammar, "Failures analysis and improvement lifetime of lead acid battery in different applications," Proceedings of Engineering & Technology (PET), pp. 148–154, 2016. 1

[25] R. Yahmadi, K. Brik, and F. b. Ammar, "Causal tree analysis for quality control of the lead acid battery manufacturing process," International Journal of Energy Research, vol. 42, no. 4, pp. 1738–1759, 2018. 2

[26] M. Hughes, R. Barton, S. Karunathilaka, and N. Hampson, "The estimation of the residual capacity of sealed lead-acid cells using the impedance technique," Journal of applied electrochemistry, vol. 16, pp. 555–564, 1986. 2

[27] R. Yu, G. Liu, L. Xu, Y. Ma, H. Wang, and C. Hu, "Review of degradation mechanism and health estimation method of vrla battery used for standby power supply in power system," Coatings, vol. 13, no. 3, p. 485, 2023. 2

[28] K. K. Sadabadi, X. Jin, and G. Rizzoni, "Prediction of remaining useful life for a composite electrode lithium ion battery cell using an electrochemical model to estimate the state of health," Journal of Power Sources, vol. 481, p. 228861, 2021. 2, 4, 37

[29] L. Ungurean, G. Cârstoiu, M. V. Micea, and V. Groza, "Battery state of health estimation: a structured review of models, methods and commercial devices," International Journal of Energy Research, vol. 41, no. 2, pp. 151–181, 2017. 2

[30] M. H. Lipu, M. Hannan, A. Hussain, M. Hoque, P. J. Ker, M. M. Saad, and A. Ayob, "A review of state of health and remaining useful life estimation methods for lithium-ion battery in electric vehicles: Challenges and recommendations," Journal of cleaner production, vol. 205, pp. 115–133, 2018. 2

[31] M. Kwiecien, J. Badeda, M. Huck, K. Komut, D. Duman, and D. U. Sauer, "Determination of soh of lead-acid batteries by electrochemical impedance spectroscopy," Applied Sciences, vol. 8, no. 6, p. 873, 2018. 2

[32] N. Picciano, Battery aging and characterization of nickel metal hydride and lead-acid batteries. PhD thesis, The Ohio State University, 2007. 2, 23, 24

[33] J. Badeda, M. Kwiecien, D. Schulte, and D. U. Sauer, "Battery state estimation for lead-acid batteries under float charge conditions by impedance: Benchmark of common detection methods," Applied Sciences, vol. 8, no. 8, p. 1308, 2018. 2

[34] W. Majchrzycki, E. Jankowska, M. Baraniak, P. Handzlik, and R. Samborski, "Electrochemical impedance spectroscopy and determination of the internal resistance as a way to estimate lead-acid batteries condition," Batteries, vol. 4, no. 4, p. 70, 2018. 2

[35] L. Tao, J. Ma, Y. Cheng, A. Noktehdan, J. Chong, and C. Lu, "A review of stochastic battery models and health management," Renewable and Sustainable Energy Reviews, vol. 80, pp. 716–732, 2017. 2

[36] N.-T. Tran, A. B. Khan, and W. Choi, "State of charge and state of health estimation of agm vrla batteries by employing a dual extended kalman filter and an arx model for online parameter estimation," Energies, vol. 10, no. 1, p. 137, 2017. 2

[37] K. K. Sadabadi, P. Ramesh, P. Tulpule, and G. Rizzoni, "Design and calibration of a semi-empirical model for capturing dominant aging mechanisms of a pba battery," Journal of Energy Storage, vol. 24, p. 100789, 2019. 2, 3, 39

[38] X. Tang, K. Liu, X. Wang, F. Gao, J. Macro, and W. D. Widanage, "Model migration neural network for predicting battery aging trajectories," IEEE Transactions on Transportation Electrification, 2020. 3

[39] C. She, Z. Wang, F. Sun, P. Liu, and L. Zhang, "Battery aging assessment for real-world electric buses based on incremental capacity analysis and radial basis function neural network," IEEE Transactions on Industrial Informatics, vol. 16, no. 5, pp. 3345–3354, 2019. 3

[40] S. Sun, J. Sun, Z. Wang, Z. Zhou, and W. Cai, "Prediction of battery soh by cnn-bilstm network fused with attention mechanism," Energies, vol. 15, no. 12, p. 4428, 2022. 3

[41] M. Esfandyari, M. H. Yazdi, V. Esfahanian, M. Masih-Tehrani, H. Nehzati, and O. Shekoofa, "A hybrid model predictive and fuzzy logic based control method for state of power estimation of series-connected lithium-ion batteries in HEVs," Journal of Energy Storage, vol. 24, p. 100758, 2019. 3

[42] S. Jiang and Z. Song, "A review on the state of health estimation methods of lead-acid batteries," Journal of Power Sources, vol. 517, p. 230710, 2022. 3

[43] J. Loukil, F. Masmoudi, and N. Derbel, "A real-time estimator for model parameters and state of charge of lead acid batteries in photovoltaic applications," Journal of Energy Storage, vol. 34, p. 102184, 2021. 3

[44] M. Messing, T. Shoa, and S. Habibi, "Estimating battery state of health using electrochemical impedance spectroscopy and the relaxation effect," Journal of Energy Storage, vol. 43, p. 103210, 2021. 3

[45] J. Olarte, J. Martínez de Ilarduya, E. Zulueta, R. Ferret, U. Fernández-Gámiz, and J. M. Lopez-Guede, "A battery management system with eis monitoring of life expectancy for lead–acid batteries," Electronics, vol. 10, no. 11, p. 1228, 2021. 3

[46] X. Hu, K. Zhang, K. Liu, X. Lin, S. Dey, and S. Onori, "Advanced fault diagnosis for lithium-ion battery systems: A review of fault mechanisms, fault features, and diagnosis procedures," IEEE Industrial Electronics Magazine, vol. 14, no. 3, pp. 65–91, 2020. 3, 4

[47] S. Tamilselvi, S. Gunasundari, N. Karuppiah, A. Razak RK, S. Madhusudan, V. M. Nagarajan, T. Sathish, M. Z. M. Shamim, C. A. Saleel, and A. Afzal, "A review on battery modelling techniques," Sustainability, vol. 13, no. 18, p. 10042, 2021. 3, 4

[48] J. Andrés and G. Andrés, Origen, progresos y estado actual de toda la literatura, vol. 3. Verbum Editorial, 2000. 9

[49] J. Schüring, H. D. Schulz, W. R. Fischer, J. Böttcher, and W. H. Duijnisveld, Redox: fundamentals, processes and applications. Springer Science & Business Media, 2013. 11, 12

[50] L. David and B. R. Thomas, "Handbook of batteries," 2001. 12, 15

[51] G. Piłatowicz, H. Budde-Meiwes, J. Kowal, C. Sarfert, E. Schoch, M. Königsmann, and D. U. Sauer, "Determination of the lead-acid battery's dynamic response using butler-volmer equation for advanced battery management systems in automotive applications," Journal of Power Sources, vol. 331, pp. 348–359, 2016. 12, 14, 15

[52] D. Burzyński and L. Kasprzyk, "The operation and capacity fade modelling of the lithium-ion cell for electric vehicles," in E3S Web of Conferences, vol. 108, p. 01017, EDP Sciences, 2019. 13

[53] S. Aswatdha, D. A. Raj, and K. U. Rani, "Design of battery pack for electric vehicles," 2019. 13

[54] F. Mohammadi, G.-A. Nazri, and M. Saif, "Modeling, simulation, and analysis of hybrid electric vehicle using matlab/simulink," in 2019 International Conference on Power Generation Systems and Renewable Energy Technologies (PGSRET), pp. 1–5, IEEE, 2019. 13

[55] F. Calise, F. L. Cappiello, A. Cartenì, M. D. d'Accadia, and M. Vicidomini, "A novel paradigm for a sustainable mobility based on electric vehicles, photovoltaic panels and electric energy storage systems: Case studies for naples and salerno (italy)," Renewable and Sustainable Energy Reviews, vol. 111, pp. 97–114, 2019. 13

[56] F. J. G. Navarro, L. J. Y. Muñoz, A. G. Fernández, and J. L. T. Moreno, "Modelado de baterías para aplicación en vehículos urbanos eléctricos ligeros," Revista Iberoamericana de Automática e Informática industrial, 2019. 13

[57] T. Nazghelichi, F. Torabi, and V. Esfahanian, "Non-dimensional analysis of electrochemical governing equations of lead-acid batteries," Journal of Energy Storage, vol. 27, p. 101120, 2020. 13

[58] S.-y. Tan, D. J. Payne, J. P. Hallett, and G. H. Kelsall, "Developments in electrochemical processes for recycling lead-acid batteries," Current Opinion in Electrochemistry, 2019. 13

[59] A. Paul, K. Subramanian, et al., "PV-based off-board electric vehicle battery charger using BIDC," Turkish Journal of Electrical Engineering & Computer Sciences, vol. 27, no. 4, pp. 2850–2865, 2019. 13

[60] J. E. d. Silva and J. Urbanetz Junior, "Converting a conventional vehicle into an electric vehicle (EV)," Brazilian Archives of Biology and Technology, vol. 62, no. SPE, 2019. 13

[61] B. S. Ammaiyappan and S. Ramalingam, "Reliability investigation of electric vehicle," Life Cycle Reliability and Safety Engineering, vol. 8, no. 2, pp. 141–149, 2019. 13

[62] M. Fisher, J. Apt, and J. F. Whitacre, "Can flow batteries scale in the behind-the-meter commercial and industrial market? a techno-economic comparison of storage technologies in california," Journal of Power Sources, vol. 420, pp. 1–8, 2019. 13

[63] B. Nykvist, F. Sprei, and M. Nilsson, "Assessing the progress toward lower priced long range battery electric vehicles," Energy policy, vol. 124, pp. 144–155, 2019. 13

[64] R. Chang, Química general para bachillerato. McGraw-Hill Interamericana, 2008. 14

[65] W. Von Baeckmann, W. Schwenk, and W. Prinz, Handbook of cathodic corrosion protection. Elsevier, 1997. 14, 48

[66] M. Keddam, O. R. Mottos, and H. Takenouti, "Reaction model for iron dissolution studied by electrode impedance: I. experimental results and reaction

model," Journal of the Electrochemical Society, vol. 128, no. 2, p. 257, 1981. 18, 62

[67] M. Keddam, O. R. Mattos, and H. Takenouti, "Reaction model for iron dissolution studied by electrode impedance: Ii. determination of the reaction model," Journal of the Electrochemical Society, vol. 128, no. 2, p. 266, 1981. 18, 62

[68] R. Xiong, "Battery management algorithm for electric vehicles," 2020. 19, 20, 23, 31, 44, 86, 97

[69] X. Hu, F. Feng, K. Liu, L. Zhang, J. Xie, and B. Liu, "State estimation for advanced battery management: Key challenges and future trends," Renewable and Sustainable Energy Reviews, vol. 114, p. 109334, 2019. 24

[70] E. Schoch, M. Königsmann, J. Kizler, C. Schmucker, B. Kronenberg, M. Bremmer, J. Schöttle, and M. Ruch, "Monitoring techniques for 12-v lead–acid batteries in automobiles," in Lead-Acid Batteries for Future Automobiles, pp. 415–442, Elsevier, 2017. 24

[71] Power-Sonic, Rechargeable Sealed Lead-Acid Battery PS-260 2 Volts 6.0 Amps. Hrs., 4 2008. 27, 43, 44, 63, 86

[72] T. Huria, M. Ceraolo, J. Gazzarri, and R. Jackey, "Simplified extended kalman filter observer for soc estimation of commercial power-oriented lfp lithium battery cells," SAE Int, 2013. 27

[73] I. Baccouche, S. Jemmali, B. Manai, N. Omar, and N. Essoukri Ben Amara, "Improved ocv model of a li-ion nmc battery for online soc estimation using the extended kalman filter," Energies, vol. 10, no. 6, p. 764, 2017. 27, 28

[74] P. T. Krein and R. S. Balog, "Life extension through charge equalization of lead-acid batteries," in 24th annual international telecommunications energy conference, pp. 516–523, IEEE, 2002. 31, 34, 44

[75] A. Oury, A. Kirchev, Y. Bultel, and E. Chainet, "PbO2/Pb2+ cycling in methanesulfonic acid and mechanisms associated for soluble lead-acid flow battery applications," Electrochimica Acta, vol. 71, pp. 140–149, 2012. 38

[76] S. Brinic, M. Metkos-Hukovic, and R. Babic, "Impedance spectroscopy as a tool for characterization of surface films on lead and lead alloys," Journal of New Materials for Electrochemical Systems, vol. 8, no. 4, p. 273, 2005. 38

[77] H. A. Catherino, F. F. Feres, and F. Trinidad, "Sulfation in lead–acid batteries," Journal of Power Sources, vol. 129, no. 1, pp. 113–120, 2004. 39

[78] L. Lam, N. Haigh, C. Phyland, and A. Urban, "Failure mode of valve-regulated lead-acid batteries under high-rate partial-state-of-charge operation," Journal of Power Sources, vol. 133, no. 1, pp. 126–134, 2004. 48

[79] S. Pelletier, O. Jabali, G. Laporte, and M. Veneroni, "Battery degradation and behaviour for electric vehicles: Review and numerical analyses of several models," Transportation Research Part B: Methodological, vol. 103, pp. 158–187, 2017. 48, 49

[80] M. Deyab, "Ionic liquid as an electrolyte additive for high performance lead-acid batteries," Journal of Power Sources, vol. 390, pp. 176–180, 2018. 48

[81] H. Bindner, T. Cronin, P. Lundsager, J. F. Manwell, U. Abdulwahid, and I. Baring-Gould, "Lifetime modelling of lead acid batteries," 2005. 48

[82] K. Nakamura, M. Shiomi, K. Takahashi, and M. Tsubota, "Failure modes of valve-regulated lead/acid batteries," Journal of Power Sources, vol. 59, no. 1-2, pp. 153–157, 1996. 49

[83] F. Vaccaro, J. Rhoades, R. Malley, B. Le, and K. Marion, "Negative strap corrosion in valve-regulated lead acid batteries and its analysis by accelerated life testing," in Proceedings of INTELEC 95. 17th International Telecommunications Energy Conference, pp. 70–77, IEEE, 1995. 49

[84] I. N. R. C. Magallanes, "Estudio del efecto de surfactantes no iónicos en la oxidación de calcopirita en medio ácido," Master's thesis, Universidad Autónoma de San Luis Potosí, 2018. 49, 50

[85] F.-M. Wang and J. Rick, "Synergy of nyquist and bode electrochemical impedance spectroscopy studies to commercial type lithium ion batteries," Solid State Ionics, vol. 268, pp. 31–34, 2014. 50

[86] W.-Y. Kim, P.-Y. Lee, J. Kim, and K.-S. Kim, "A nonlinear-model-based observer for a state-of-charge estimation of a lithium-ion battery in electric vehicles," Energies, vol. 12, no. 17, p. 3383, 2019. 56, 90

[87] M. Dubarry and D. Beck, "Perspective on mechanistic modeling of li-ion batteries," Accounts of Materials Research, vol. 3, no. 8, pp. 843–853, 2022. 61

[88] R. Reséndiz-Ramírez, A. Rodríguez-López, J. A. Díaz-Real, H. F. Delgado-Arenas, A. Osornio-Villa, R. Hernández-Leos, V. Vivier, and R. Antaño-López, "Reaction mechanisms of the electrosynthesis of magnetite nanoparticles studied by electrochemical impedance spectroscopy," ACS omega, vol. 7, no. 1, pp. 761–772, 2021. 62, 64, 65, 66, 67

[89] E. R. Larios-Durán, G. Trejo, T. W. Chapman, and R. Antano-Lopez, "Estimation of intrinsic rate constants of electrochemical adsorption-desorption processes from ac impedance data," Electrochemical and solid-state letters, vol. 10, no. 7, p. F27, 2007. 63

[90] S. R. Niya, M. Hejabi, and F. Gobal, "Estimation of the kinetic parameters of processes at the negative plate of lead-acid batteries by impedance studies," Journal of Power Sources, vol. 195, no. 17, pp. 5789–5793, 2010. 63, 70

[91] A. A. Shah, X. Li, R. G. Wills, and F. C. Walsh, "A mathematical model for the soluble lead-acid flow battery," Journal of The Electrochemical Society, vol. 157, no. 5, p. A589, 2010. 63, 70

[92] P. Ekdunge, "A simplified model of the lead/acid battery," Journal of Power Sources, vol. 46, no. 2-3, pp. 251–262, 1993. 63, 64

[93] D. Trinh, M. Keddam, X. R. Nóvoa, and V. Vivier, "Characterization of adsorbates by transient measurements in scanning electrochemical microscopy," Electrochimica Acta, vol. 131, pp. 28–35, 2014. 64

[94] K. Ogata and Y. Yang, Modern control engineering, vol. 4. Prentice hall India, 2002. 66

[95] D. C. Giancoli, Physics: principles with applications, vol. 1. Pearson Educación, 2005. 67

[96] M. Hejabi, A. Oweisi, and N. Gharib, "Modeling of kinetic behavior of the lead dioxide electrode in a lead–acid battery by means of electrochemical impedance spectroscopy," Journal of Power Sources, vol. 158, no. 2, pp. 944–948, 2006. 68

[97] M. Vinod and K. Vijayamohanan, "A novel, non-destructive method for the prediction of the state-of-charge of maintenance-free lead/acid batteries from galvanostatic transients," Journal of power sources, vol. 52, no. 1, pp. 135–139, 1994. 70

[98] J. Zhang, P. Wang, Y. Liu, Z. Cheng, et al., "Variable-order equivalent circuit modeling and state of charge estimation of lithium-ion battery based on electrochemical impedance spectroscopy," Energies, vol. 14, no. 3, p. 769, 2021. 71, 73, 75

[99] J. Sihvo, T. Roinila, and D.-I. Stroe, "Novel fitting algorithm for parametrization of equivalent circuit model of li-ion battery from broadband impedance measurements," IEEE Transactions on Industrial Electronics, vol. 68, no. 6, pp. 4916–4926, 2020. 71, 75

[100] N. I. Picciano, Battery aging, diagnosis, and prognosis of lead-acid batteries for automotive application. PhD thesis, The Ohio State University, 2009. 71, 72, 75, 90

[101] J. R. Scully, D. C. Silverman, and M. W. Kendig, "Electrochemical impedance: analysis and interpretation," ASTM Philadelphia, 1993. 72

[102] B. Bullecks, R. Suresh, and R. Rengaswamy, "Rapid impedance measurement using chirp signals for electrochemical system analysis," Computers & chemical engineering, vol. 106, pp. 421–436, 2017. 73

[103] D. R. Andrews, "Ultrasonics and acoustics," in Encyclopedia of Physical Science and Technology (Third Edition) (R. A. Meyers, ed.), pp. 269–287, New York: Academic Press, third edition ed., 2003. 73

[104] A. J. Bard, L. R. Faulkner, et al., "Fundamentals and applications," Electrochemical Methods, vol. 2, no. 482, pp. 580–632, 2001. 73

[105] J. M. E. Sihvo, "Internal impedance measurement techniques and charger dynamics for lithium-ion batteries," Master's thesis, 2017. 73

[106] M. Van Haeverbeke, M. Stock, and B. De Baets, "Equivalent electrical circuits and their use across electrochemical impedance spectroscopy application domains," IEEE Access, 2022. 74

[107] Y. Jin and P. J. McGinn, "Bulk solid state rechargeable lithium ion battery fabrication with al-doped Li7La3Zr2O12 electrolyte and Cu0. 1V2O5 cathode," Electrochimica Acta, vol. 89, pp. 407–412, 2013. 75

[108] B.-Y. Chang, "Conversion of a constant phase element to an equivalent capacitor," Journal of Electrochemical Science and Technology, vol. 11, no. 3, pp. 318–321, 2020. 75

[109] W. Zhou, Y. Zheng, Z. Pan, and Q. Lu, "Review on the battery model and soc estimation method," Processes, vol. 9, no. 9, p. 1685, 2021. 90

[110] G. Besançon, Nonlinear observers and applications, vol. 363. Springer, 2007. 91

[111] A. Johansson and A. Medvedev, "An observer for systems with nonlinear output map," Automatica, vol. 39, no. 5, pp. 909–918, 2003. 91

[112] Y. Tian, C. Chen, B. Xia, W. Sun, Z. Xu, and W. Zheng, "An adaptive gain nonlinear observer for state of charge estimation of lithium-ion batteries in electric vehicles," Energies, vol. 7, no. 9, pp. 5995–6012, 2014. 91

[113] B. Xia, C. Chen, Y. Tian, W. Sun, Z. Xu, and W. Zheng, "A novel method for state of charge estimation of lithium-ion batteries using a nonlinear observer," Journal of power sources, vol. 270, pp. 359–366, 2014. 91

[114] C.-T. Chen, "Linear system theory and design, holt," Rinhart and Winston, Orlando, 1984. 94

[115] H. K. Khalil, "Nonlinear systems third edition," Patience Hall, vol. 115, 2002. 94

[116] S. X. Ding, Model-based fault diagnosis techniques: design schemes, algorithms, and tools. Springer Science & Business Media, 2008. 100